Exploring the Earth

NORSAR Scientific Report No.2-2014

Semiannual Technical Summary

1 July – 31 December 2014

Tormod Kværna (Ed.)

Kjeller, August 2015

NORSAR

Table of Contents

1 Summary

This report provides summary information on operation and maintenance (O&M) activities at the Norwegian National Data Center (NOR-NDC) for CTBT verification during the period 1 July – 31 December 2014, as well as scientific and technical contributions relevant to verification in a broad sense. The O&M activities, including operation of monitoring stations and transmission links within Norway and to Vienna, Austria are being funded jointly by the CTBTO/PTS and the Norwegian Government, with the understanding that the funding of O&M activities for primary stations in the International Monitoring System (IMS) will gradually be transferred to the CTBTO/PTS. The O&M statistics presented in this report maintain consistency with long-standing reporting practices. Research activities described in this report are mainly funded by the Norwegian Government, with other sponsors acknowledged where appropriate.

A summary of the activities at NOR-NDC relating to field installations, data acquisition, data forwarding and processing during the reporting period is provided in chapters 2 – 4 of this report. Norway contributes data from two primary seismic arrays: the Norwegian Seismic Array NOA (IMS code PS27) and the Arctic Regional Seismic Array ARCES (IMS code PS28), one auxiliary seismic array on Spitsbergen (SPITS, IMS code AS72), and one auxiliary three-component station at Jan Mayen (JMIC, IMS code AS73). In addition, NORSAR provides data from one infrasound array in northern Norway (IMS code IS37), and one radionuclide monitoring station on Spitsbergen (IMS code RN49). These data are provided to the International Data Centre (IDC) in Vienna via the Global Communications Infrastructure (GCI).

This report presents operational statistics for NOA, ARCES, SPITS, JMIC and IS37, as well as for additional seismic stations which through cooperative agreements with institutions in the host countries provide continuous data to the NOR-NDC. These additional stations include the Finnish Regional Seismic Array (FINES, IMS code PS17) and the Hagfors array in Sweden (HFS, IMS code AS101). Operational statistics for the reestablished NORES array and three other three-component stations operated by NORSAR are also provided. These three stations are Åknes (AKN), Jettan (JETT) and TROLL in Antarctica.

All Norwegian IMS stations, the NOA and the ARCES seismic arrays (PS27 and PS28, respectively), the radionuclide station at Spitsbergen (RN49), the auxiliary seismic stations on Spitsbergen (AS72) and Jan Mayen (AS73), as well as the infrasound array at Bardufoss (IS37) are certified by the CTBTO/PTS. Provided that adequate funding continues to be made available (from the CTBTO/PTS and the Norwegian Ministry of Foreign Affairs), we envisage continuing the provision of data from these stations in accordance with current procedures. As part of NORSAR's obsolescence management, the recapitalization of ARCES started in September/October 2014, with replacement of the sensors,

digitizers, multiplexers and the timing system.

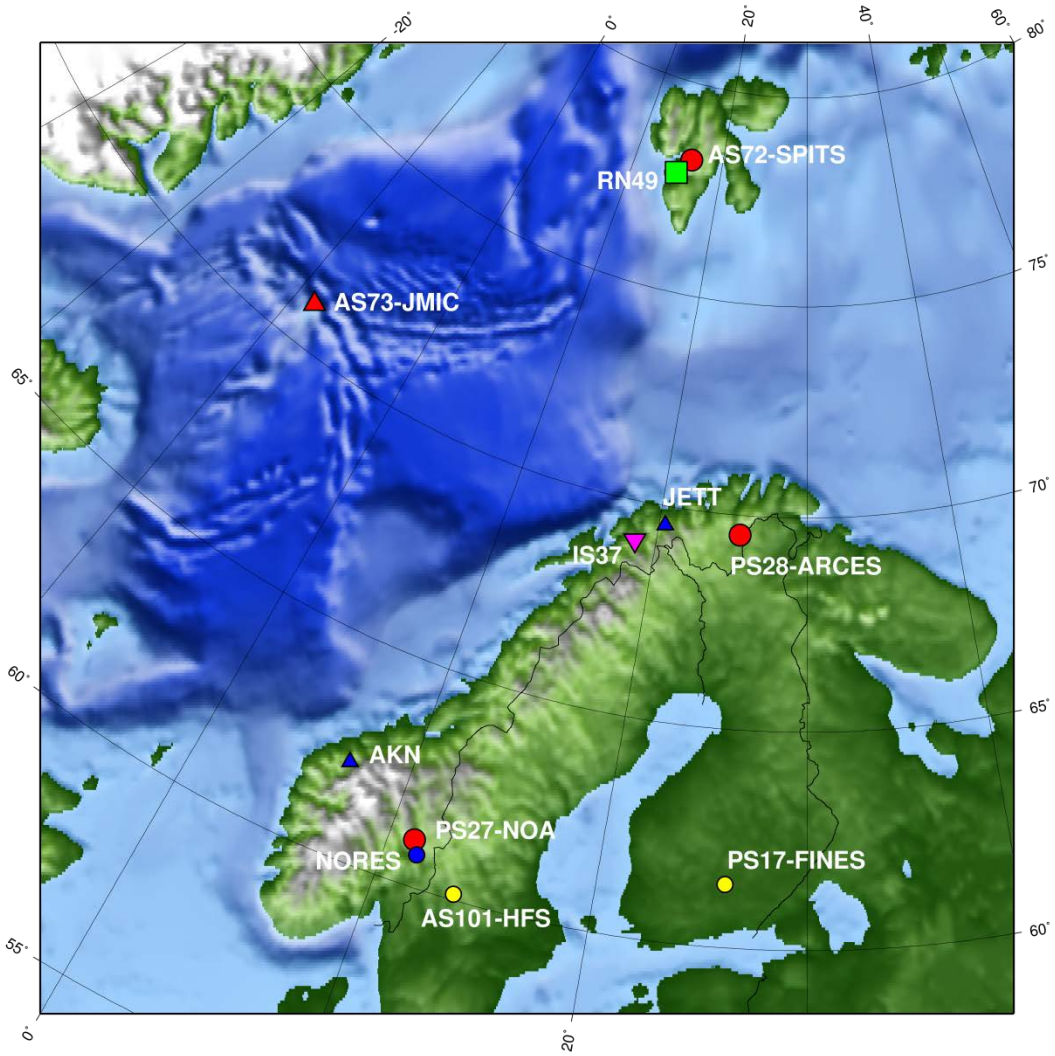

Fig. 1.1 *Locations of stations covered in this report (except TROLL in Antarctica, see Figure. 3.5.1). Norwegian seismic IMS stations are shown in red. Other Norwegian seismic stations are shown by blue symbols. Contributing IMS seismic stations in other countries are yellow. Circles indicate seismic arrays and triangles indicate single 3-component seismic stations. The IMS infrasound station IS37 is shown by a purple inverted triangle, and the IMS radionuclide station RN49 is shown by a green square.*

Three scientific and technical contributions presented in chapter 6 of this report are provided as follows:

Section 6.1 entitled “3-D Crustal Model for Southern Norway” describes results derived by tomographic inversion of a large dataset of local and regional events recorded by seismic stations in southern Norway. The merged dataset, recorded during different projects and time periods, contains altogether 175 events. Hit maps and checkerboard tests indicate that the dataset provides the best resolution in the central part of southern Norway down to about 35-40 km depth. For the outskirts of

the study region the depth resolution decreases. The obtained 3-D P-wave velocity model indicates velocity perturbations up to ±0.4 km/s compared to the reference velocity model, and the inversion shows higher seismic velocities compared to the reference velocity model under the central mountain plateau. The Moho depth ranges from 31 km beneath the Oslo Graben and SW coast of southern Norway to about 35 km beneath the mountain plateau.

In 2012, the 42 vertical-component short-period seismometers of the NOA array were upgraded to broadband sensors. This upgrade allows for array processing over a broader frequency range, and section 6.2 addresses the development of a procedure for detection of long-period signals at the NOA array. The first part of the procedure includes beamforming, bandpass filtering in several frequency bands and detection processing by an STA/LTA detector. This is followed by estimation of back-azimuth and phase velocity by f-k analysis. Promising results were achieved for detection and recognition of Rayleigh waves. Because of the Rayleigh-type nature of ocean microseisms, it has proven difficult to consistently separate microseism detections from surface waves produced by earthquakes or explosions. The development of a further processing step involving dispersion testing or pattern recognition in near-real time could remedy this shortcoming and potentially yield a powerful tool for surface waves analysis in the CTBT context. Furthermore, such a development could provide very useful information for seismic noise studies, e.g., ambient noise seismic tomography.

Section 6.3 addresses observations of stratospheric and thermospheric infrasound signals at the IMS infrasound array IS37 near Bardufoss in northern Norway. In August and September 2014, IS37 recorded for the first time infrasound signals from each of the 15 ammunition destruction explosions at Hukkakero, a military site in northern Finland. In section 6.3 we examine the celerities observed from these events for which low and high frequency infrasound arrivals are observed and we examine the ability of ray-tracing to predict these arrivals, both in unperturbed atmospheric models and in models where perturbations are added to simulate the effect of gravity waves.

We find that the thermospheric arrivals are predicted using the ray-tracer without the addition of any perturbations to the atmospheric model. However, the perturbations are necessary to be able to predict rays with turning points at stratospheric altitudes. The thermospheric phases are typically of lower frequency and they are not observed at all for the smallest of these events. Celerity expectation lookup tables calculated from probability distributions of the gravity-wave perturbed models can be helpful for interpretation of infrasound signals and for improving event location.

T. Kværna

2 Operation of International Monitoring System (IMS) Stations in Norway

2.1 PS27 — Primary Seismic Station NOA

The mission-capable data statistics were 99.999%, as compared to 100.000% for the previous reporting period. The net instrument availability was 96.330%

Monthly uptimes for the NORSAR on-line data recording task, taking into account all factors (field installations, transmissions line, data center operation) affecting this task were as follows:

	Mission Capable	Net instrument availability
July 2014:	99.999	94.304
August 2014:	99.997	94.738
September 2014:	99.999	94.480
October 2014:	99.998	96.394
November 2014:	99.999	98.073
December 2014:	100.000	99.993

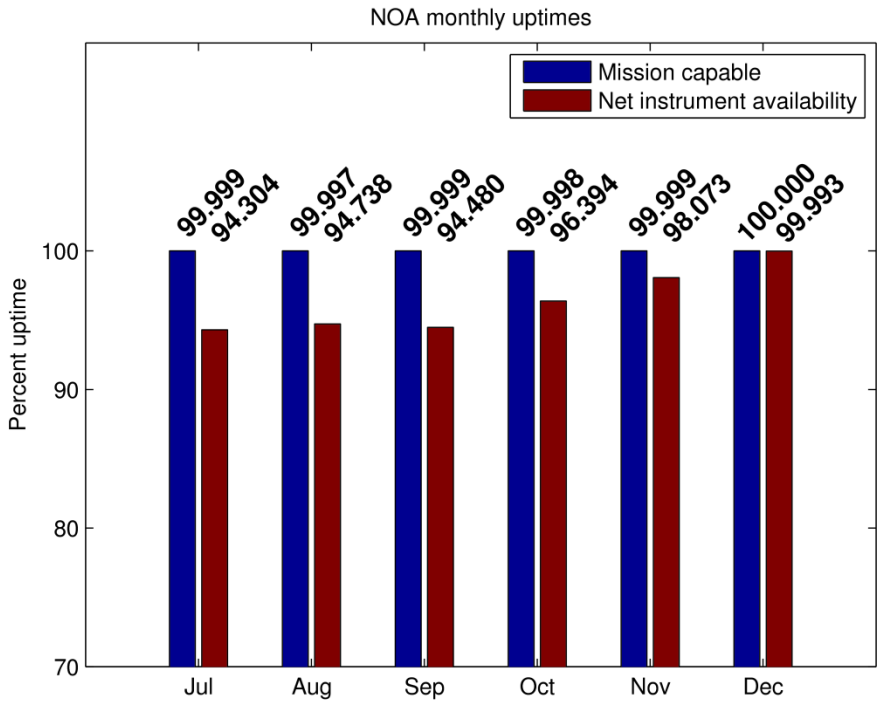

Fig. 2.1.1 Monthly uptimes for NOA for the period July - December 2014.

B. Paulsen

2.1.1 NOA event detection operation

In Table 2.1.1 some monthly statistics of the Detection and Event Processor operation are given. The table lists the total number of detections (DPX) triggered by the on-line detector, the total number of detections processed by the automatic event processor (EPX) and the total number of events accepted after analyst review (teleseismic phases, core phases and total).

	Total DPX	Total EPX	Accepted events P-phases	Core Phases	Sum	Daily average
Jul 14	5210	993	299	126	425	13.7
Aug	6003	918	312	51	363	11.7
Sep	5759	927	266	61	327	10.9
Oct	6474	881	219	50	269	8.7
Nov	9241	1261	268	62	330	11.0
Dec	8268	1029	210	59	269	8.7
	40955	6009	1574	409	1983	10.8

Table 2.1.1. Detection and event processor statistics, 1 July – 31 December 2014.

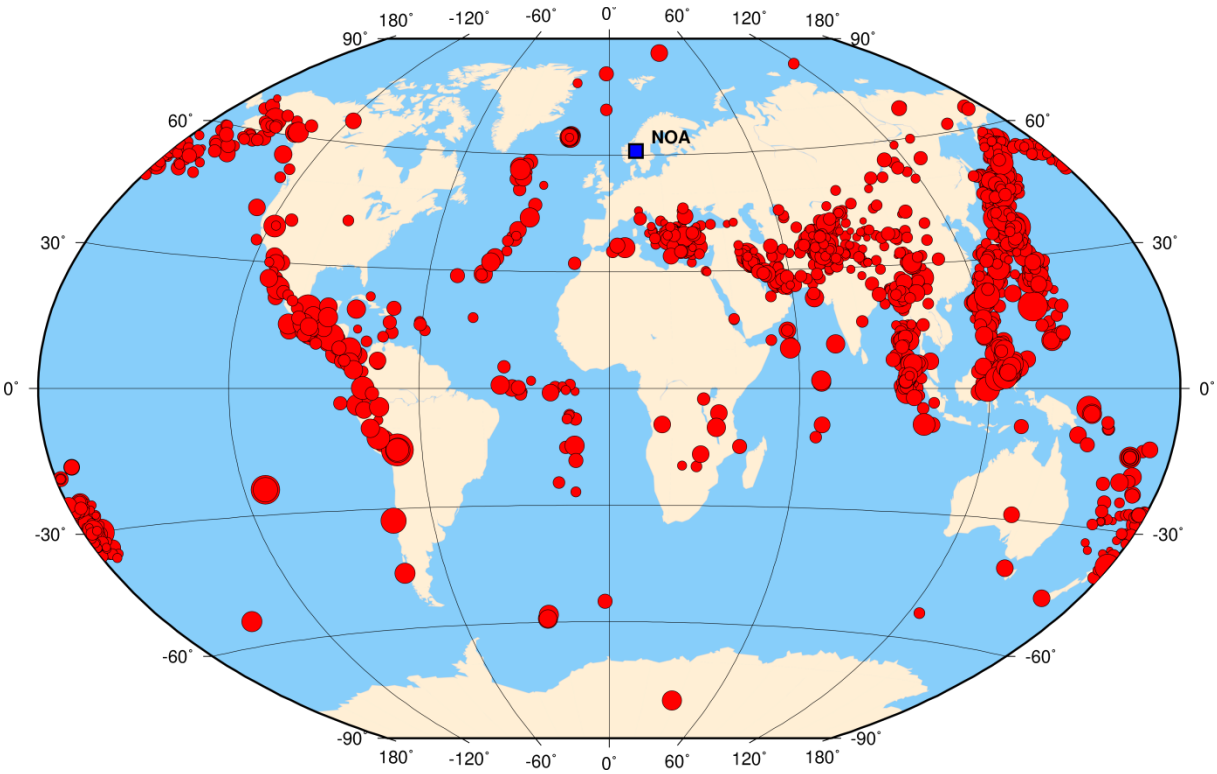

Fig. 2.1.2 Distribution of events in NORSAR's teleseismic reviewed bulletin for the time interval 1 July – 31 December 2014. Event symbols are scaled proportionally to event magnitude. The location of NOA is noted with a blue square. All locations are based on phase interpretation and inversion of slowness and backazimuth into a location, using the NOA array alone.

NOA detections

The number of detections (phases) reported by the NORSAR detector during day 182, 2014, through day 365, 2014, was 40,955, giving an average of 223 detections per processed day (184 days processed).

B. Paulsen
U. Baadshaug

2.2 PS28 — Primary Seismic Station ARCES

In September/October 2014, the recapitalization of ARCES started.

The old Nanometrics HRD24 digitisers and Teledyne Geotech seismometers were replaced by Guralp CMG-3T hybrid response seismometers and Guralp CMG-DM24S3EAM digitisers systems.

The central and pit fibre optic multiplexers were replaced by new and similar equipment from Guralp. The Nanometrics central timing system was replaced by Guralp central timing system. A Network Acquisition Module – NAM and a Moxa PC was installed for CD1.1 data forwarding.

New broadband data collection started 19 September 2014 together with some old data channels, and the complete array was ready 21 September 2014.

The mission-capable data statistics were 99.662%, as compared to 99.968% for the previous reporting period. The net instrument availability was 95.601%.
Monthly uptimes for the ARCES on-line data recording task, taking into account all factors (field installations, transmission lines, data center operation) affecting this task were as follows:

	Mission Capable	Net instrument availability
July 2014:	99.997	92.465
August 2014:	99.998	89.912
September 2014:	98.000	91.280
October 2014:	99.982	99.979
November 2014:	99.998	99.972
December 2014:	100.000	99.996

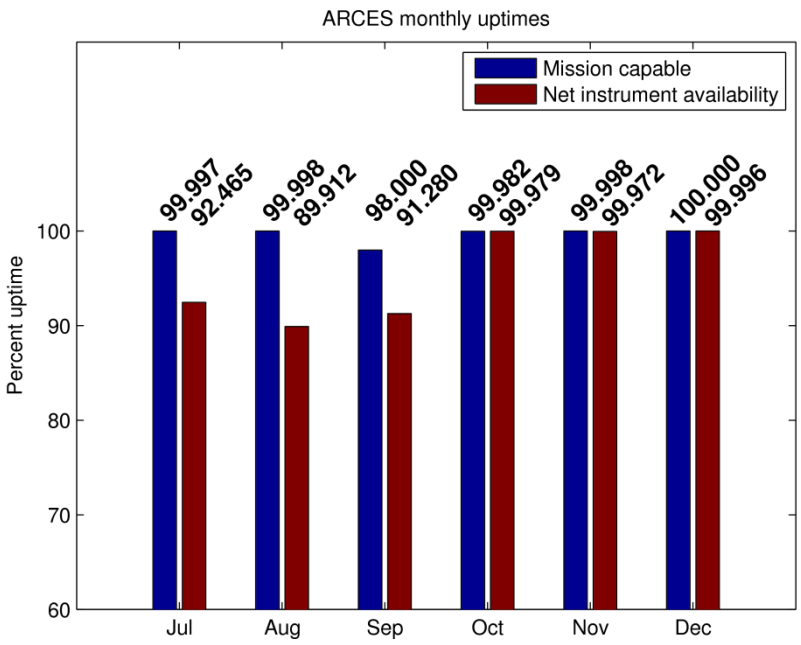

Fig. 2.2.1 Monthly uptimes for ARCES for the period July - December 2014.

B. Paulsen

2.2.1 Event detection operation

ARCES detections

The number of detections (phases) reported during day 182, 2014, through day 365, 2014, was 211,942, giving an average of 1,152 detections per processed day (184 days processed).

Events automatically located by ARCES

During days 182, 2014, through day 365, 2014, 7,783 local and regional events were located by ARCES, based on automatic association of P- and S-type arrivals. This gives an average of 42.3 events per processed day (184 days processed). 71% of these events are within 300 km, and 91% of these events are within 1000 km.

U. Baadshaug

2.3 AS72 — Auxiliary Seismic Station on Spitsbergen

The mission-capable statistics for the period were 99.570%, as compared to 97.226% for the previous reporting period. The net instrument availability was 96.360%.

Monthly uptimes for the Spitsbergen on-line data recording task, taking into account all factors (field installations, transmissions line, data center operation) affecting this task were as follows:

	Mission Capable	Net instrument availability
July 2014:	99.963	95.201
August 2014:	99.958	95.194
September 2014:	99.964	95.199
October 2014:	97.600	93.714
November 2014:	99.968	99.965
December 2014:	99.970	98.887

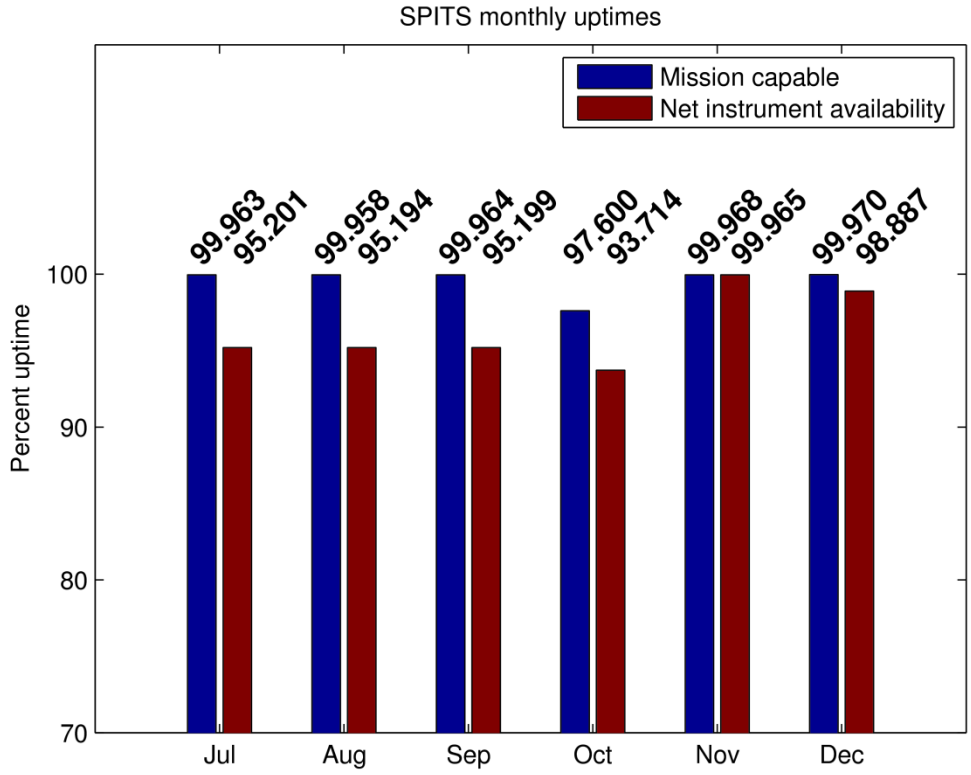

Fig. 2.3.1 Monthly uptimes for SPITS for the period July - December 2014.

B. Paulsen

2.3.1 Event detection operation

Spitsbergen array detections

The number of detections (phases) reported from day 182, 2014, through day 365, 2014, was 597,600, giving an average of 3,248 detections per processed day (184 days processed).

Events automatically located by the Spitsbergen array

During days 182, 2014, through day 365, 2014, 54,958 local and regional events were located by the Spitsbergen array, based on automatic association of P- and S-type arrivals. This gives an average of 298.7 events per processed day (184 days processed). 82% of these events are within 300 km, and 92% of these events are within 1000 km.

U. Baadshaug

2.4 AS73 — Auxiliary Seismic Station at Jan Mayen

Monthly uptimes for the Jan Mayen on-line data recording task, taking into account all factors (field installations, transmissions line, data center operation) affecting this task were as follows:

	Mission Capable	Net instrument availability
July 2014:	99.996	99.996
August 2014:	99.994	99.994
September 2014:	100.000	100.000
October 2014:	100.000	100.000
November 2014:	100.000	100.000
December 2014:	100.000	100.000

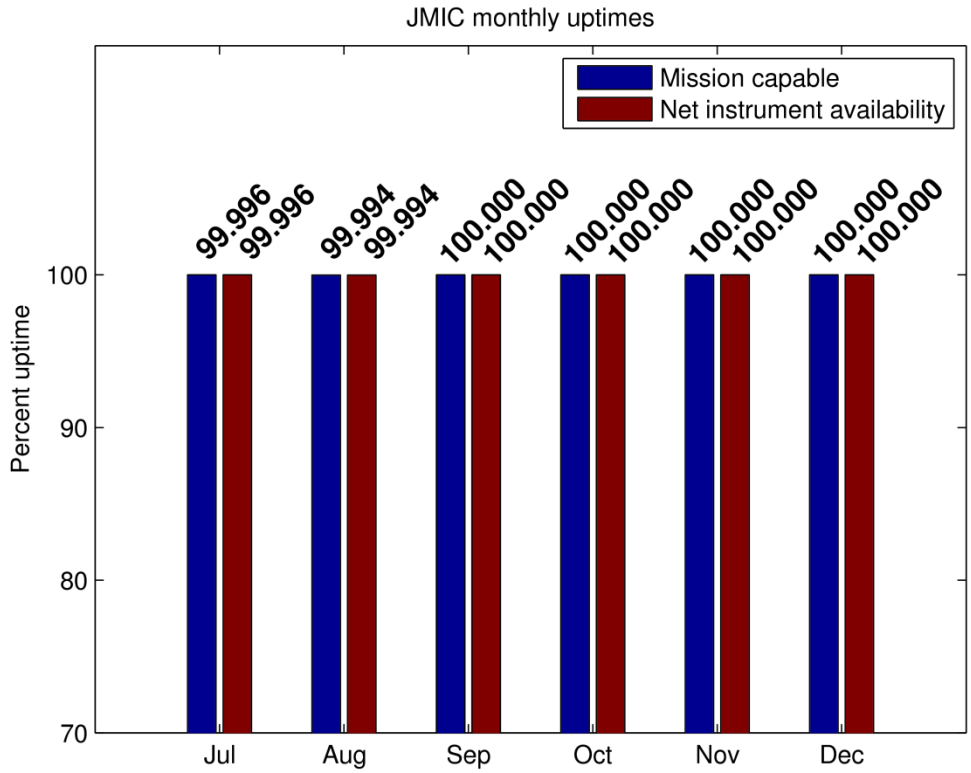

Fig. 2.4.1 Monthly uptimes for JMIC for the period July - December 2014.

B. Paulsen

2.5 IS37 — Infrasound Station at Bardufoss

Monthly uptimes for the IS37 on-line data recording task, taking into account all factors (field installations, transmissions line, data center operation) affecting this task were as follows:

	Mission Capable	**Net instrument availability**
July 2014:	99.996	99.980
August 2014:	99.999	99.998
September 2014:	99.992	99.996
October 2014:	99.997	99.997
November 2014:	99.998	99.998
December 2014:	100.000	100.000

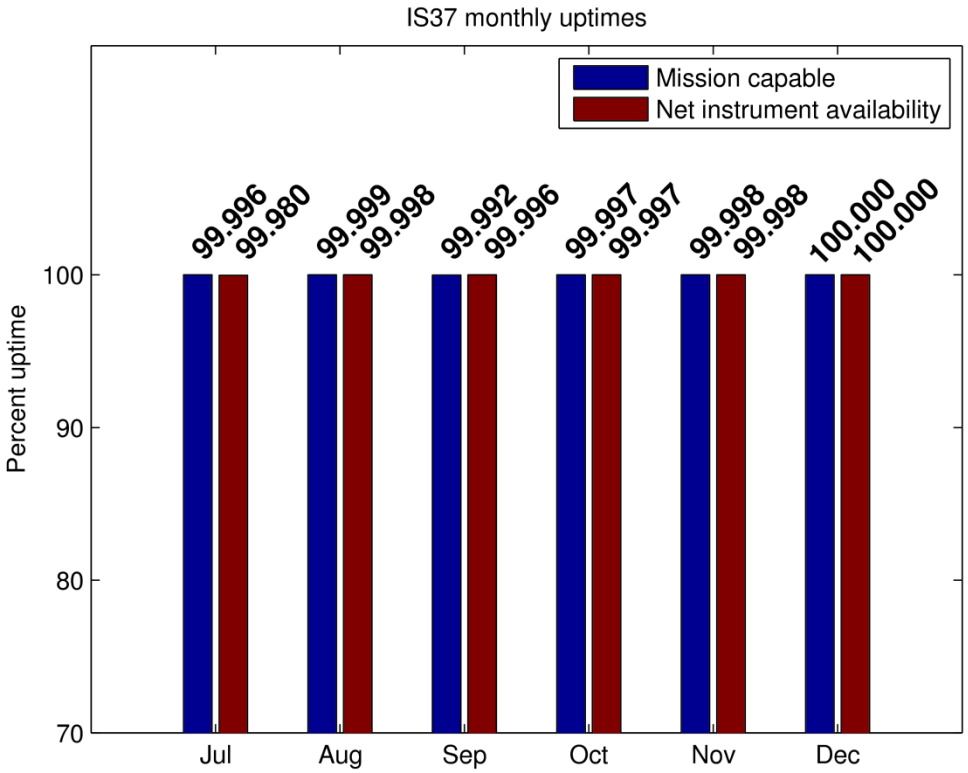

Fig. 2.5.1 Monthly uptimes for IS37 for the period July - December 2014.

U. Baadshaug

2.6 RN49 — Radionuclide Station on Spitsbergen

The IMS particulate radionuclide network includes a station on the island of Spitsbergen. This station was selected to be among those IMS radionuclide stations that will also monitor for the presence of relevant noble gases upon entry into force of the CTBT.

A site survey for this station was carried out in August of 1999 by NORSAR, in cooperation with the Norwegian Radiation Protection Authority. The site survey report to the PTS contained a recommendation to establish this station at Platåberget, near Longyearbyen. The infrastructure for housing the station equipment was established in early 2001, and a noble gas detection system, based on the Swedish "SAUNA" design, was installed at this site in May 2001, as part of CTBTO PrepCom's noble gas experiment. A particulate station ("ARAME" design) was installed at the same location in September 2001. A certification visit to the particulate station took place in October 2002, and the particulate station was certified on 10 June 2003. Both systems underwent substantial upgrades in May/June 2006. The noble gas system was certified on 21 December 2012. The equipment at RN49 is being maintained and operated under a contract with the CTBTO/PTS.

S. Mykkeltveit

3 Contributing Regional Arrays and Three-Component Stations

3.1 NORES

3.1.1 NORES seismic array

During the reporting interval, the NORES array has been operating with instruments at nine sites (site A0, sites A1-A3 and B1-B5, together spanning an aperture of approximately 650 meters).

Monthly uptimes for the NORES on-line data recording task, taking into account all factors (field installations, transmission lines, data center operation) affecting this task are given in the following table:

	Data availability
July 2014:	96.177
August 2014:	99.997
September 2014:	97.307
October 2014:	90.851
November 2014:	100.000
December 2014:	99.676

3.1.2 NRSI infrasound array

In 2013, infrasound sensors were installed at each of the 9 sites in the NORES seismic array.

Monthly uptimes for the NRSI on-line data recording task, taking into account all factors (field installations, transmission lines, data center operation) affecting this task are given in the following table:

	Data availability
July 2014:	96.174
August 2014:	99.997
September 2014:	97.307
October 2014:	90.851
November 2014:	100.000
December 2014:	99.676

B. Paulsen

3.2 Hagfors (IMS Station AS101)

Data from the Hagfors array are made available continuously to NORSAR through a cooperative agreement with Swedish authorities.

The mission-capable data statistics were 93.673%, as compared to 98.130% for the previous reporting period. The net instrument availability was 77.538%.

Monthly uptimes for the Hagfors on-line data recording task, taking into account all factors (field installations, transmission lines, data center operation) affecting this task were as follows:

	Mission Capable	**Net instrument availability**
July 2014:	99.983	97.663
August 2014:	64.564	47.819
September 2014:	99.979	66.654
October 2014:	99.985	66.659
November 2014:	99.993	87.183
December 2014:	97.532	99.248

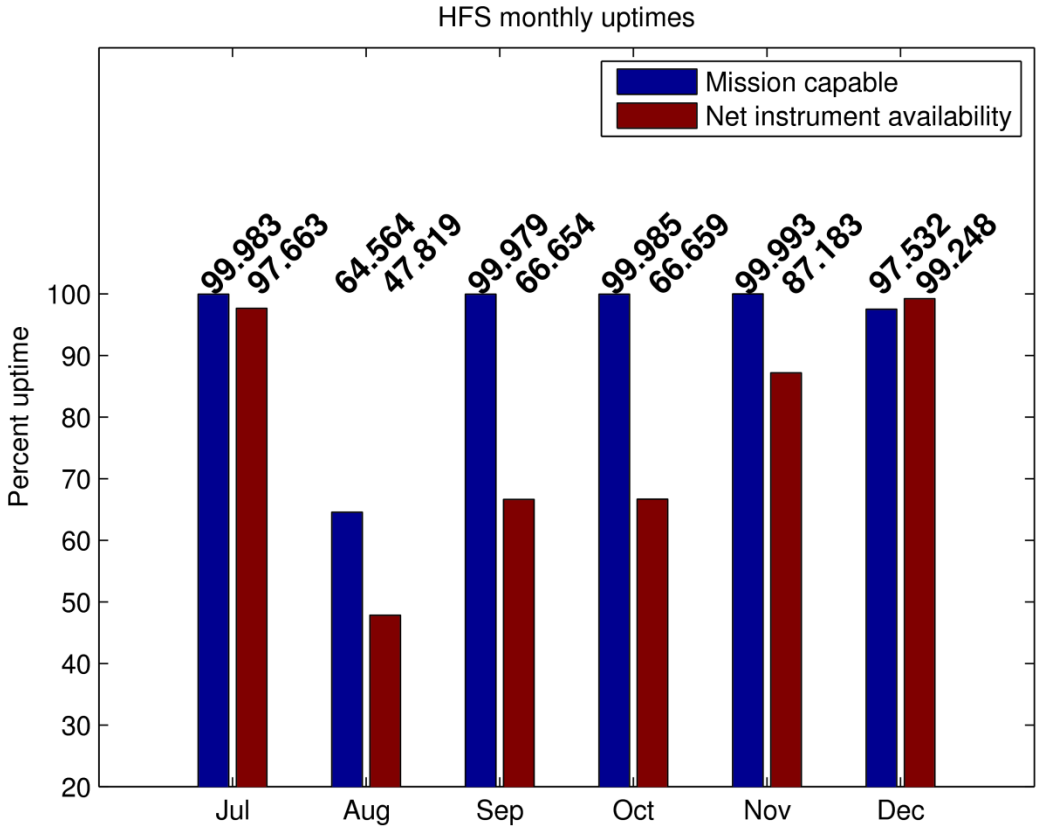

Fig. 3.2.1 Monthly uptimes for HFS for the period July - December 2014. Hagfors was struck by lightning 3 August 2014. 5 out of 9 fiber optic modems were destroyed and four sites stayed down until the array was repaired on 13 November 2014.

B. Paulsen

3.2.1 Hagfors event detection operation

Hagfors array detections

The number of detections (phases) reported from day 182, 2014, through day 365, 2014, was 152,036, giving an average of 879 detections per processed day (173 days processed).

Events automatically located by the Hagfors array

During days 182, 2014, through day 365, 2014, 6,334 local and regional events were located by the Hagfors array, based on automatic association of P- and S-type arrivals. This gives an average of 36.6 events per processed day (173 days processed). 76% of these events are within 300 km, and 92% of these events are within 1000 km.

U. Baadshaug

3.3 FINES (IMS Station PS17)

Data from the FINES array are made available continuously to NORSAR through a cooperative agreement with Finnish authorities.

The mission-capable data statistics were 99.596%, as compared to 99.067% for the previous reporting period. The net instrument availability was 99.132%.

Monthly uptimes for the FINES on-line data recording task, taking into account all factors (field installations, transmissions line, data center operation) affecting this task were as follows:

	Mission Capable	Net instrument availability
July 2014:	97.636	96.652
August 2014:	99.988	99.988
September 2014:	99.980	99.980
October 2014:	99.986	99.986
November 2014:	99.997	99.134
December 2014:	99.992	99.050

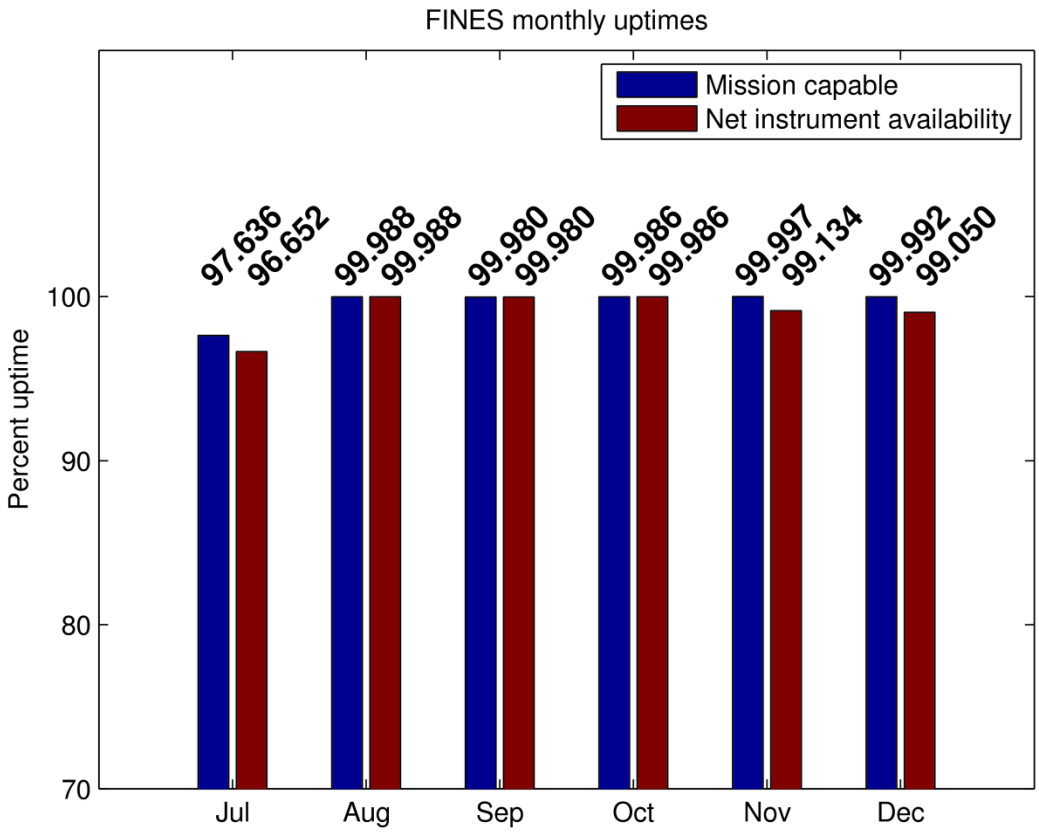

Fig. 3.3.1 Monthly uptimes for FINES for the period July - December 2014.

B. Paulsen

3.3.1 FINES event detection operation

FINES detections

The number of detections (phases) reported during day 182, 2014, through day 365, 2014, was 33,796, giving an average of 189 detections per processed day (179 days processed).

Events automatically located by FINES

During days 182, 2014, through day 365, 2014, 1,965 local and regional events were located by FINES, based on automatic association of P- and S-type arrivals. This gives an average of 11.0 events per processed day (179 days processed). 88% of these events are within 300 km, and 94% of these events are within 1000 km.

U. Baadshaug

3.4 Åknes (AKN)

Monthly uptimes for the AKN on-line data recording task, taking into account all factors (field installations, transmission lines, data center operation) affecting this task are given in the following table:

	Data availability
July 2014:	100.000
August 2014:	92.677
September 2014:	99.997
October 2014:	99.991
November 2014:	83.331
December 2014:	100.000

U. Baadshaug

3.5 TROLL, Antarctica

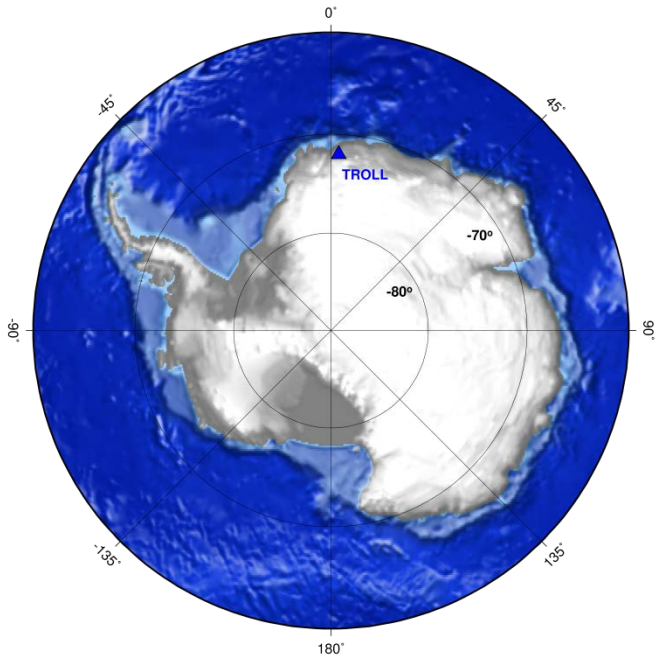

Fig. 3.5.1
Location of the 3-component seismic station TROLL in Antarctica.

Monthly uptimes for the TROLL on-line data recording task, taking into account all factors (field installations, transmission lines, data center operation) affecting this task are given in the following table:

	Data availability
July 2014:	100.000
August 2014:	89.628
September 2014:	100.000
October 2014:	100.000
November 2014:	92.238
December 2014:	100.000

The low data availability numbers in August and November were caused by an Ethernet switch which probably failed because of static electricity.

U. Baadshaug

3.6 Jettan (JETT)

The seismic broadband station JETT was installed in Novmber 2014 on top of an unstable rock slope at Jettan, Nordnes, Kåfjord kommune, Troms. Its primary purpose is the monitoring of local seismic activity related to the movement of the slope. The station has been sending continuous real-time data (40 and 200 Hz sampling rate) to NORSAR since 5 November 2014.

Monthly uptimes for the JETT on-line data recording task, taking into account all factors (field installations, transmission lines, data center operation) affecting this task are given in the following table:

	Data availability
July 2014:	
August 2014:	
September 2014:	
October 2014:	
November 2014:	85.128
December 2014:	99.988

U. Baadshaug

3.7 Regional Monitoring System Operation and Analysis

The Regional Monitoring System (RMS) was installed at NORSAR in December 1989 and has been operated from 1 January 1990 for automatic processing of data from ARCES and NORES. Several updates have been installed, and the current version of RMS that accepts data from an arbitrary number of arrays and single 3-component stations and has also the capability of locating events at teleseismic distances. All array data available at the NDC is being automatically processed and all data, including 3-component single stations are made available to the analyst for review of events.

3.7.1 Phase and event statistics

Table 3.6.1 gives a summary of phase detections and events declared by RMS. From top to bottom the table gives the total number of detections by the RMS, the number of detections that are associated with events automatically declared by the RMS, the number of detections that are not associated with any events, the number of events automatically declared by the RMS, and finally the total number of events worked on interactively (in accordance with criteria that vary over time; see below) and defined by the analyst.

New criteria for interactive event analysis were introduced from 1 January 1994. Since that date, only regional events in areas of special interest (e.g., Spitsbergen, since it is necessary to acquire new knowledge in this region) or other significant events (e.g., felt earthquakes and large industrial explosions) were thoroughly analyzed. Teleseismic events of special interest are also analyzed.

The GBF program is used as a pre-processor to RMS, and only phases associated with selected events in northern Europe are considered in the automatic RMS phase association. All detections, however, are still available to the analysts and can be added manually during analysis.

	Jul 14	Aug 14	Sep 14	Oct 14	Nov 14	Dec 14	Total
Phase detections	165480	207704	224703	217504	199867	185434	1200692
- Associated phases	8422	10133	10754	8531	7316	6970	52126
- Unassociated phases	157058	197571	213949	208973	192551	178464	1148566
Events automatically declared by RMS	1628	2237	2453	1936	1411	1319	10984
No. of events defined by the analyst	67	45	41	41	70	43	307

Table 3.7.1. RMS phase detections and event summary 1 July – 31 December 2014.

U. Baadshaug
B. Paulsen

4 The Norwegian National Data Center and Field Activities

4.1 NOR-NDC Activities

NORSAR functions as the Norwegian National Data Center (NOR-NDC) for CTBT verification. Six monitoring stations, comprising altogether 87 seismic and infrasound waveform sensor sites plus radionuclide monitoring equipment, are located on Norwegian territory as part of the IMS, as described elsewhere in this report. All six IMS stations are in full operation, and are providing data to the CTBTO/PTS on a regular basis. They are all certified by the CTBTO. Data recorded by the Norwegian stations are being transmitted in real time to the NOR-NDC, and provided to the IDC through the Global Communications Infrastructure (GCI). Norway is connected to the GCI with an MPLS link to Vienna.

Operating the Norwegian IMS stations continues to require significant efforts by personnel both at the NOR-NDC and in the field. Strictly defined procedures as well as increased emphasis on regularity of data recording and timely data transmission to the IDC in Vienna have led to increased reporting and calibration activities and implementation of new procedures for the NOR-NDC. The NOR-NDC carries out all the technical tasks required in support of Norway's treaty obligations. NORSAR will also carry out assessments of events of special interest, and advise the Norwegian authorities in technical

matters relating to treaty compliance. A challenge for the NOR-NDC is to carry 40 years' experience over to the next generation of personnel.

4.1.1 Verification functions; information received from the IDC

After the CTBT enters into force, the IDC will provide data for a large number of events each day, but will not assess whether any of them are likely to be nuclear explosions. Such assessments will be the task of the States Parties, and it is important to develop the necessary national expertise in the participating countries. An important task for the NOR-NDC will thus be to make independent assessments of events of particular interest to Norway, and to communicate the results of these analyses to the Norwegian Ministry of Foreign Affairs.

4.1.2 Monitoring the Arctic region

Norway will have monitoring stations of key importance for covering the Arctic, including Novaya Zemlya, and Norwegian experts have a unique competence in assessing events in this region. On several occasions in the past, seismic events near Novaya Zemlya have caused political concern, and NORSAR specialists have contributed to clarifying these issues.

4.1.3 International cooperation

After entry into force of the treaty, a number of countries are expected to establish national expertise to contribute to the treaty verification on a global basis. Norwegian experts have been in contact with experts from several countries with the aim of establishing bilateral or multilateral cooperation in this field.

4.1.4 NORSAR event processing

The automatic routine processing of NORSAR events as described in NORSAR Sci. Rep. No. 2-93/94, has been running satisfactorily. The analyst tools for reviewing and updating the solutions have been continually modified to simplify operations and improve results. NORSAR is currently applying teleseismic detection and event processing using the large-aperture NOA array, as well as regional monitoring using the network of small-aperture arrays in Fennoscandia and adjacent areas.

4.1.5 Communication topology

Norway has implemented an independent subnetwork, which connects the IMS stations AS72, AS73, PS28, RN49 and IS37 operated by NORSAR to the GCI at the NOR-NDC. VSAT is used for communication for PS28 and AS73. VSAT antennas for 6 of the PS27 subarrays have been installed for intra-array communication. The seventh subarray is connected to the central recording facility via a leased land line. The central recording facility for PS27 is connected directly to the GCI (Basic Topology). All VSAT communication is functioning satisfactorily. Since 10 June 2005, AS72 and RN49 have been connected to the NOR-NDC through a VPN link. IS37 is also connected to the NOR-NDC through two redundant VPN links; one based on a WIFI Internet service, an one based on GSM service. The IS37 system for communication has proven to be very successful, with a lot of available capacity, and is a model for changing communication for PS27 and PS28.

J. Fyen

4.2 Status Report: Provision of Data from Norwegian IMS Stations to the IDC

4.2.1 Introduction

This contribution is a report for the period July - December 2014 on activities associated with provision of data from Norwegian seismic IMS stations to the International Data Centre (IDC) in Vienna. This report represents an update of contributions that can be found in previous editions of NORSAR's Semiannual Technical Summary. All four Norwegian seismic stations providing data to the IDC have been formally certified.

4.2.2 Norwegian IMS stations and communications arrangements

During the reporting interval, Norway has provided data to the IDC from the five waveform (seismic, infrasound) stations shown in Fig. 4.2.1. PS27 — NOA is a 60 km aperture teleseismic array, comprising of 7 subarrays, each containing five vertical broadband sensors and one three-component hybrid broadband instrument. PS28 — ARCES is a 25-element regional array with an aperture of 3 km, whereas AS72 — Spitsbergen array (station code SPITS) has 9 elements within a 1-km aperture. AS73 — JMIC has a single three-component broadband instrument. IS37 is a 10-element infrasound array.

The intra-array communication for NOA utilizes a land line for subarray NC6 and VSAT links based on iDirect technology for the other 6 subarrays. The central recording facility for NOA is located at the Norwegian National Data Center (NOR-NDC).

Continuous ARCES data are transmitted from the ARCES site to the NOR-NDC using the same iDirect network as NOA.

Continuous SPITS data are transmitted to NOR-NDC via the central recording facility (CRF) for the SPITS array at the University Centre in Svalbard (UNIS). Data from the array elements to the CRF are transmitted via a 2.4 Ghz radio link (Wilan VIP-110). A 512 Kbps SHDSL link has been established between UNIS and NOR-NDC. Both AS72 and RN49 data are now transmitted to NOR-NDC over this link using VPN technology.

A minimum of 14-day station buffers have been established at the IS37, ARCES and SPITS sites and at all NOA subarray sites, as well as at the NOR-NDC for IS37, ARCES, SPITS and NOA. In addition, each individual site of the IS37, SPITS and NOA arrays has a 14-days buffer.

The NOA and ARCES arrays are primary stations in the IMS network, which implies that data from these stations are transmitted continuously to the receiving International Data Centre. Since October 1999, these data have been transmitted (from NOR-NDC) via the Global Communications Infrastructure (GCI) to the IDC in Vienna. Data from the auxiliary array station SPITS — AS72 have been sent in continuous mode to the IDC storage facility during the reporting period. AS73 — JMIC is an auxiliary station in the IMS, and also this station is transmitted in continuous mode to the same IDC storage facility. In addition, continuous data from all three arrays are transmitted to the US_NDC under a bi-lateral agreement.

NORSAR also provides broadband data from Norwegian IMS stations to ORFEUS and IRIS.

4.2.3 Uptimes and data availability

Figs. 4.2.2, 4.2.3 and 4.2.4 show the monthly uptimes for the Norwegian IMS primary stations ARCES and NOA, and the IMS infrasound array IS37, respectively, for the reporting period given as the red (taller) bars in these figures. These barplots reflect the percentage of the waveform data that is available in the NOR-NDC data archives for these three arrays. The downtimes inferred from these figures thus represent the cumulative effect of field equipment outages, station site to NOR-NDC communication outage, and NOR-NDC data acquisition outages.

Figs. 4.2.2, 4.2.3 and 4.2.4 also give the data availability for these three stations as reported by the IDC in the IDC Station Status reports.

4.2.4 NOR-NDC automatic processing and data analysis

These tasks have proceeded in accordance with the descriptions given in Sci. Rep. No. 2-95/96 (Mykkeltveit and Baadshaug). For the reporting period NOR-NDC derived information on 307 events and submitted this information to the Finnish NDC as the NOR-NDC contribution to the Bulletin of seismic events in northern Europe. These events are plotted in Fig. 4.2.5.

4.2.5 Current developments and future plans

NOR-NDC is continuing the efforts towards improving and hardening all critical data acquisition and data forwarding hardware and software components, so as to meet the requirements related to operation of IMS stations.

The NOA array was formally certified by the PTS on 28 July 2000, and a contract with the PTS in Vienna currently provides partial funding for operation and maintenance of this station. The ARCES array was formally certified by the PTS on 8 November 2001, and a contract with the PTS is in place which also provides for partial funding of the operation and maintenance of this station. The operation of the two IMS auxiliary seismic stations on Norwegian territory (Spitsbergen and Jan Mayen) is funded by the Norwegian Ministry of Foreign Affairs. Provided that adequate funding continues to be made available (from the PTS and the Norwegian Ministry of Foreign Affairs), we envisage continuing the provision of data from all Norwegian seismic IMS stations without interruption to the IDC in Vienna.

The IS37 station was certified on 19 December 2013 and a contract with the PTS is in place for the operation and maintenance of this station.

The PS27 - NOA equipment was recapitalized during 2010-2012, and the station has been revalidated. The PS28 - ARCES equipment was acquired in 1999, and it is no longer possible to get spare digitizers. A recapitalization plan for the array was submitted to the PTS in October 2008. The recapitalization of the array started in September 2014; see a description in section 2.2 above.

U. Baadshaug
S. Mykkeltveit
J. Fyen

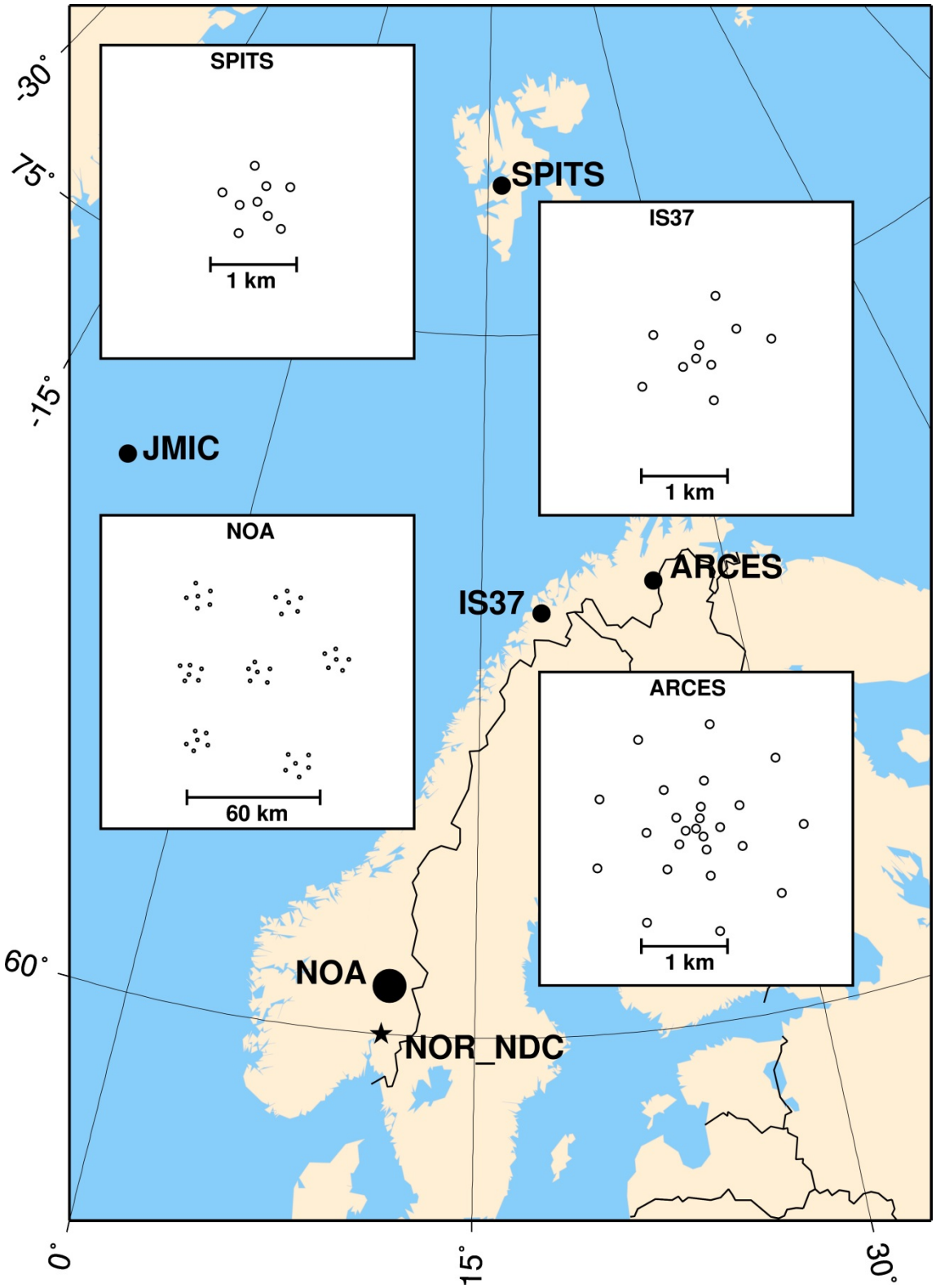

Fig. 4.2.1. The figure shows the locations and configurations of the three Norwegian seismic IMS array stations that provided data to the IDC during the period July - December 2014. The data from these stations and the JMIC three-component station are transmitted continuously and in real time to the Norwegian NDC (NOR-NDC). The stations NOA and ARCES are primary IMS stations, whereas SPITS and JMIC are auxiliary IMS stations. JMIC is a three-component station, the other stations are arrays. IS37 is an IMS infrasound station.

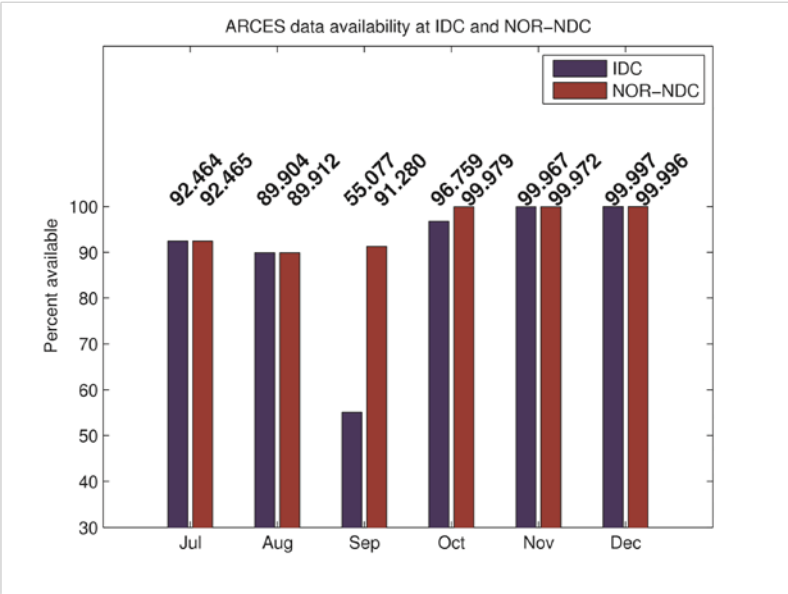

Fig. 4.2.2 The figure shows the monthly availability of ARCES array data for the period July - December 2014 at NOR-NDC and the IDC. In the ARCES recapitalization, the channel names (se/sn/sz) of the data from the old Teledyne Geotech seismometers were replaced (by BHE/BHN/BHZ) for the new Guralp CMG-3T hybrid response seismometers. This name change was not introduced into the IDC CHAN_STATUS reports until 2 October 2014, and is the reason for the low IDC data availability in September 2014.

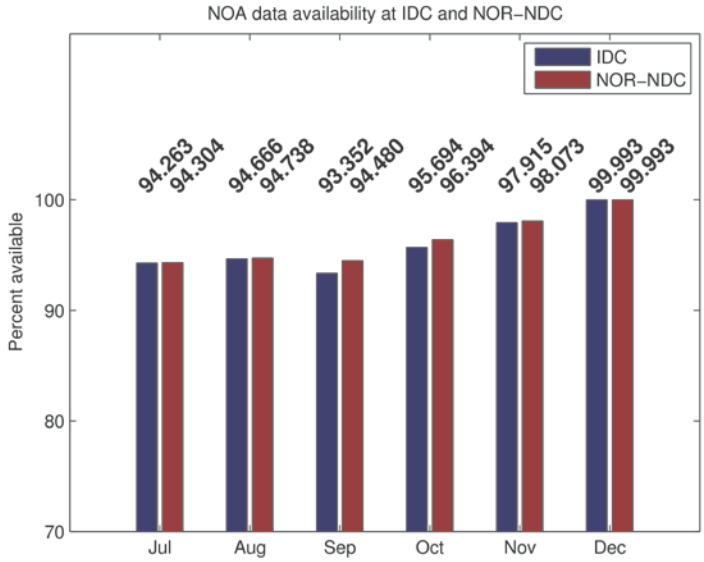

Fig. 4.2.3 The figure shows the monthly availability of NOA array data for the period July - December 2014 at NOR-NDC and the IDC.

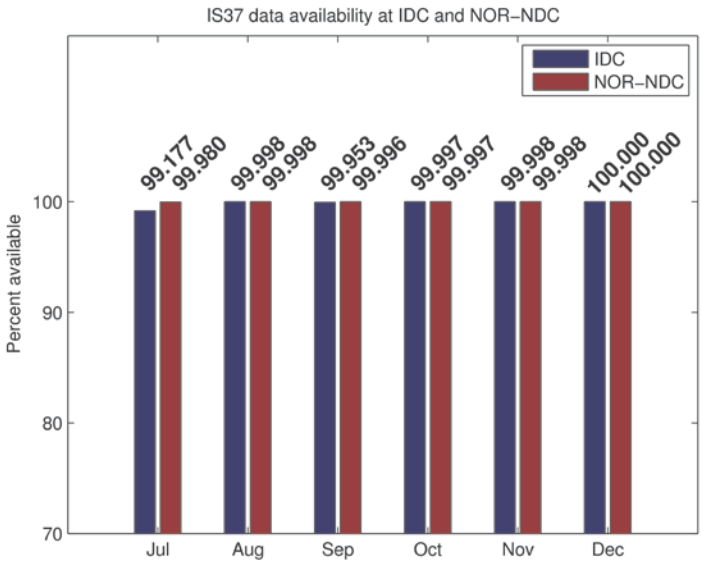

Fig. 4.2.4 The figure shows the monthly availability of IS37 infrasound array data for the period July - December 2014 at NOR-NDC and the IDC.

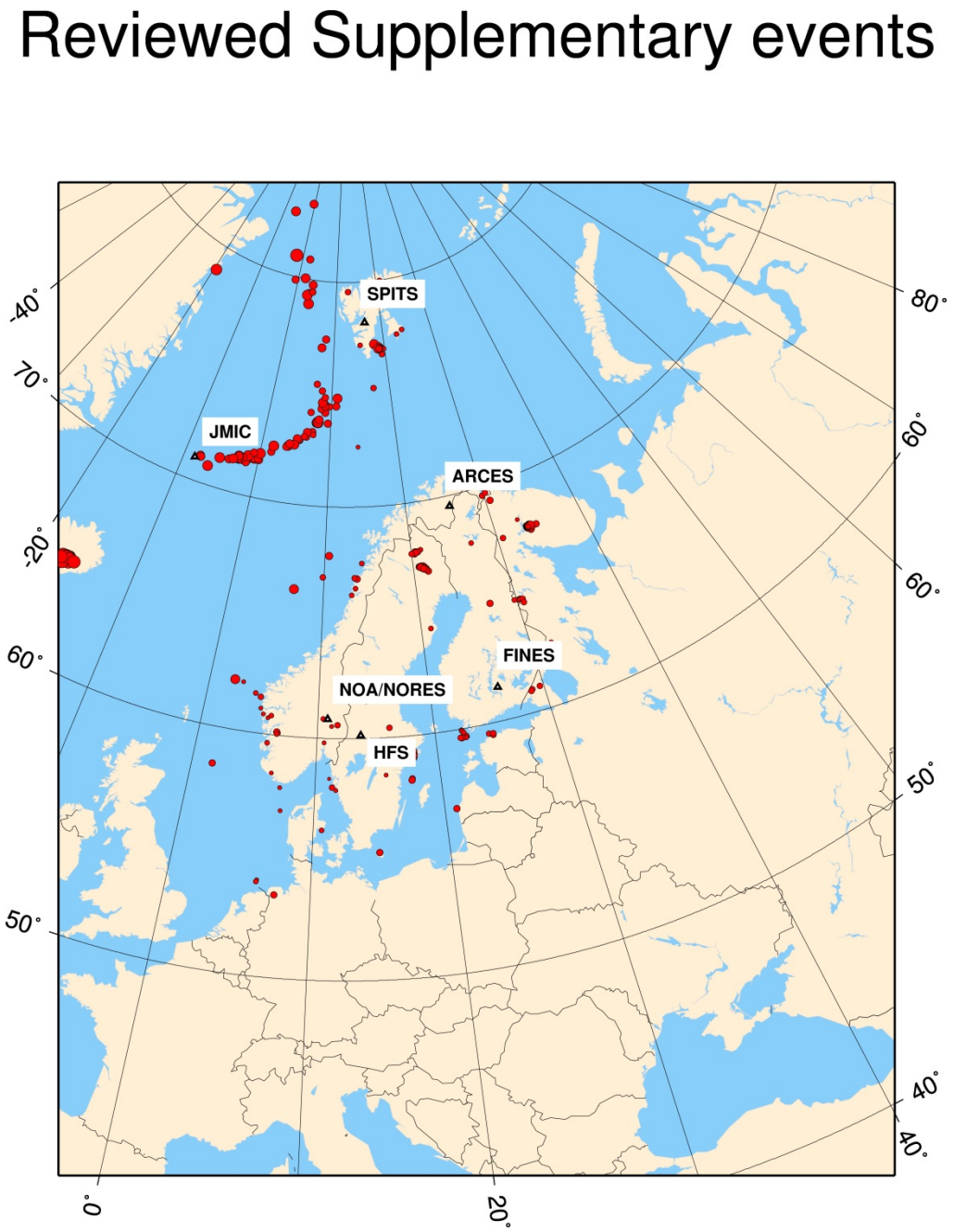

Fig. 4.2.5 The map shows the 307 events in and around Norway contributed by NOR-NDC during July - December 2014 to the Bulletin of seismic events in northern Europe compiled by the Finnish NDC. The map also shows the main seismic stations used in the data analysis to define these events.

4.3 Field Activities

The activities at the NORSAR Maintenance Center (NMC) at Hamar currently include work related to operation and maintenance of the following IMS seismic stations: the NOA teleseismic array (PS27), the ARCES array (PS28) and the Spitsbergen array (AS72). Some work has also been carried out in connection with the seismic station on Jan Mayen (AS73), the radionuclide station at Spitsbergen (RN49), and installation of the infrasound station IS37. NORSAR also acts as a consultant for the operation and maintenance of the Hagfors array in Sweden (AS101).

NORSAR carries out the field activities relating to IMS stations in a manner generally consistent with the requirements specified in the appropriate IMS Operational Manuals, which are currently being developed by Working Group B of the Preparatory Commission. For seismic stations these specifications are contained in the Operational Manual for Seismological Monitoring and the International Exchange of Seismological Data (CTBT/WGB/TL-11/2), currently available in a draft version.

All regular maintenance on the NORSAR field systems is conducted on a one-shift-per-day, five-day-per-week basis. The maintenance tasks include:

- Operating and maintaining the seismic sensors and the associated digitizers, authentication devices and other electronics components.
- Maintaining the power supply to the field sites, as well as backup power supplies.
- Operating and maintaining the VSATs, the data acquisition systems and the intra-array data transmission systems.
- Assisting the NDC in evaluating the data quality and making the necessary changes in gain settings, frequency response and other operating characteristics as required.
- Carrying out preventive, routine, and emergency maintenance to ensure that all field systems operate properly.
- Maintaining a computerized record of the utilization, status, and maintenance history of all site equipment.
- Providing appropriate security measures to protect against incidents such as intrusion, theft and vandalism at the field installations.

Details of the daily maintenance activities are kept locally. As part of its contract with CTBTO/PTS, NORSAR submits, when applicable, problem reports, outage notification reports and equipment status reports. The contents of these reports and the circumstances under which they will be submitted are specified in the draft Operational Manual.

P.W. Larsen
K.A. Løken

5 Documentation Developed

Antonovskaya, G., Y. Konechnaya, E. O. Kremenetskaya, V. Asming, T. Kværna, J. Schweitzer and F. Ringdal (2014). Enhanced Earthquake Monitoring in the European Arctic. *Polar Science* (September 2014), doi:10.1016/j.polar.2014.08.003

Celli, N. L., J. Schweitzer and J. Fyen (2014). The DPEP Long-Period Detector for the NOA Broadband Array. In: *NORSAR Scientific Report **2-2014***, Semiannual Technical Summary, 1 July – 31 December 2014.

Gal, M., A. M. Reading, S. P. Ellingsen, K. D. Koper, S. J. Gibbons and S. P. Näsholm. Improved implementation of the fk and Capon methods for array analysis of seismic noise. *Geophysical Journal International*, Vol. **198**, No. 2. (01 August 2014), pp. 1045-1054, doi:10.1093/gji/ggu183

Janutyte, I., E. Kozlovskaya, M. Majdanski, P. H. Voss, M. Budraitis, and PASSEQ Working Group (2014). Traces of the crustal units and the upper-mantle structure in the southwestern part of the East European Craton. *Solid Earth*, **5**, 821–836, doi:10.5194/se-5-821-2014.

Janutyte, I. and T. Kværna (2014). 3-D Crustal Model for Southern Norway. In: *NORSAR Scientific Report **2-2014***, Semiannual Technical Summary, 1 July – 31 December 2014.

Näsholm, S. P., S. J. Gibbons and T. Kværna (2014). Stratospheric and Thermospheric Infrasound Signals Recorded at IS37. In: *NORSAR Scientific Report **2-2014***, Semiannual Technical Summary, 1 July – 31 December 2014.

Schweitzer, J., M. Pirli, M. Roth and T. Kværna (2014). TROLL: a new, very broadband seismic station in Antarctica. *Seismological Research Letters*, **85**, (4), 852-862, doi: 10.1785/0220130223

6 Technical Reports / Papers Published

6.1 3-D Crustal Model for Southern Norway

6.1.1 Introduction

The presented study is a part of the Norwegian National Seismological Network (NNSN) project carried out by the University of Bergen (UiB) in cooperation with NORSAR. In this study we aim to obtain a 3-D crustal model of P and S waves for Norway. Here we present our results obtained for the southern part of Norway limited to 56-65° N latitude and 2-14° E longitude.

Development of the 3-D velocity model was divided into two steps:

1) To obtain the optimal 1-D velocity model of the Earth's crust in the study area. The model was obtained using the VELEST program (Kissling et al., 1994) which is implemented into the SEISAN program package (Ottemoller et al., 2014). The VELEST was modified at NORSAR implementing station naming of five symbols and transformation for a spherical earth. The obtained model is used as a reference velocity model for development of the 3-D model.

2) To obtain the 3-D velocity model. The model was obtained using the FMTOMO program (Rawlinson and Sambridge, 2005).

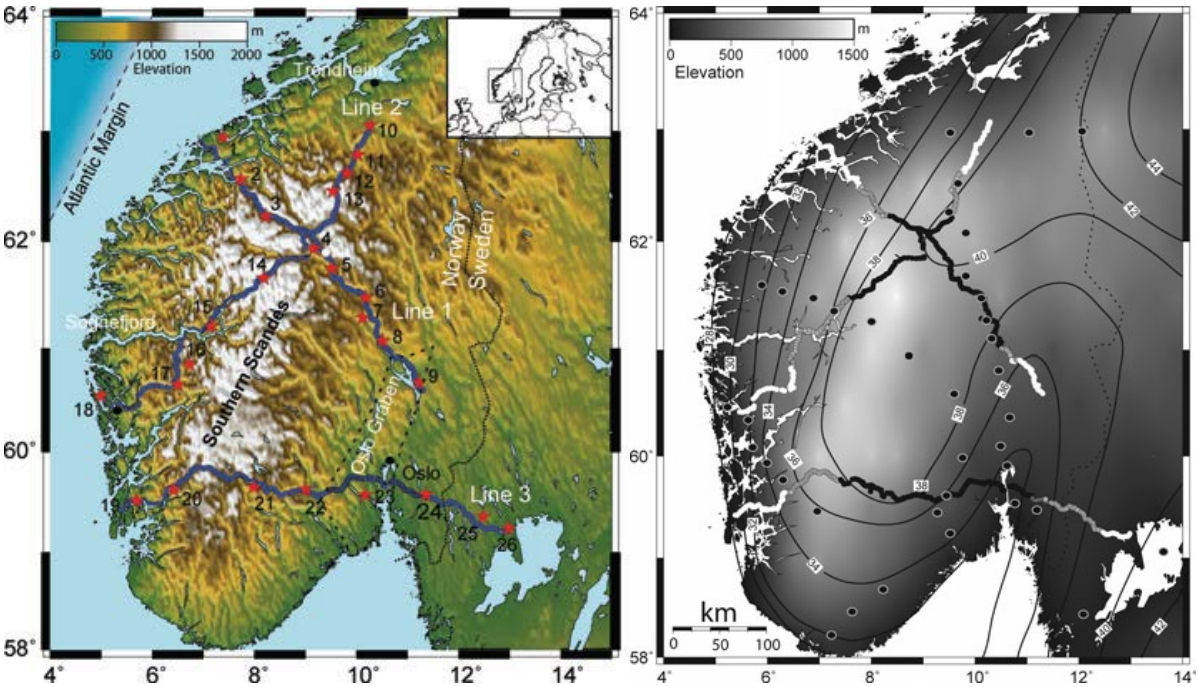

Fig. 6.1.1 (After Stratford et al., 2009) (Left panel) Study area of the Magnus-Rex project. Red stars indicate locations of shots, blue dots indicate the seismic stations. The shot lines 1, 2 and 3 marked in blue. Insert: map of northern Europe showing the study area. (Right panel) New Moho map for southern Norway. Labelled contours represent Moho depth in km.

The obtained 1-D and 3-D velocity models may improve the location results of the local seismic events originating in southern Norway.

6.1.2 Previous studies

The geological – tectonic conditions in Norway are very complicated. The territory of Norway experienced a number of different tectonic regimes: uplift and subsidence (Lidmar-Bergstrøm et al., 2000), folding and faulting which resulted in dislocation of nappes (Roberts and Gee, 1985). After the Caledonian orogeny the region experienced an extensional regime (Andersen, 1998). The uplift processes due to erosion (Faleide et al., 2002) and postglacial rebound (Balling, 1980) are still present.

Some studies of the Earth's crust in the southern part of Norway have previously been carried out. The early efforts to define depth of the Moho boundary were performed using data of refraction profiling. The results showed that the crust is about 38 km thick beneath the mountains (Sellevoll and Warrick, 1971), while more recent studies of receiver functions estimate the Moho to about 43 km depth in this part. In 2007 there was carried out a seismic refraction experiment Magnus-Rex (Stratford et al., 2009), during which three nearly 400 km long seismic lines were deployed in southern Norway. The results obtained from the studies of Magnus-Rex data indicate Moho depth variations from about 30 to about 40 km (Figure 6.1.1) along the indicated profiles in Figure 6.1.2. This result is quite consistent with the recent receiver function studies by Kolstrup (2015) (Figure 6.1.3).

6.1.3 Study area and dataset

The study area is limited to 58-65° N latitude and 4-14° E longitude. We used seismological data recorded by seismic stations deployed in southern Norway during different projects (Figure 6.1.1). The compiled dataset contains 175 seismic events (Table 6.1.2):

1) 47 events from the original UiB seismological catalog (year 2009-2013). The events were re-picked and relocated at NORSAR using the same velocity model which is used by the UiB;

2) 72 events from the MAGNUS project (year 2007-2008). The data was analyzed at the UiB;

3) 32 events from NORSAR seismological bulletins (year 2014);

4) 24 explosions from the Magnus-Rex project; the data was analyzed at NORSAR.

Statistics for inversion with the VELEST program:

1) 175 local seismic events: 151 events (both natural and man-made quarry blasts) and 24 explosions from the Magnus-Rex project;

2) 105 seismic stations;

3) 4347 phase readings: 2922 P wave arrivals and 1425 S wave arrivals.

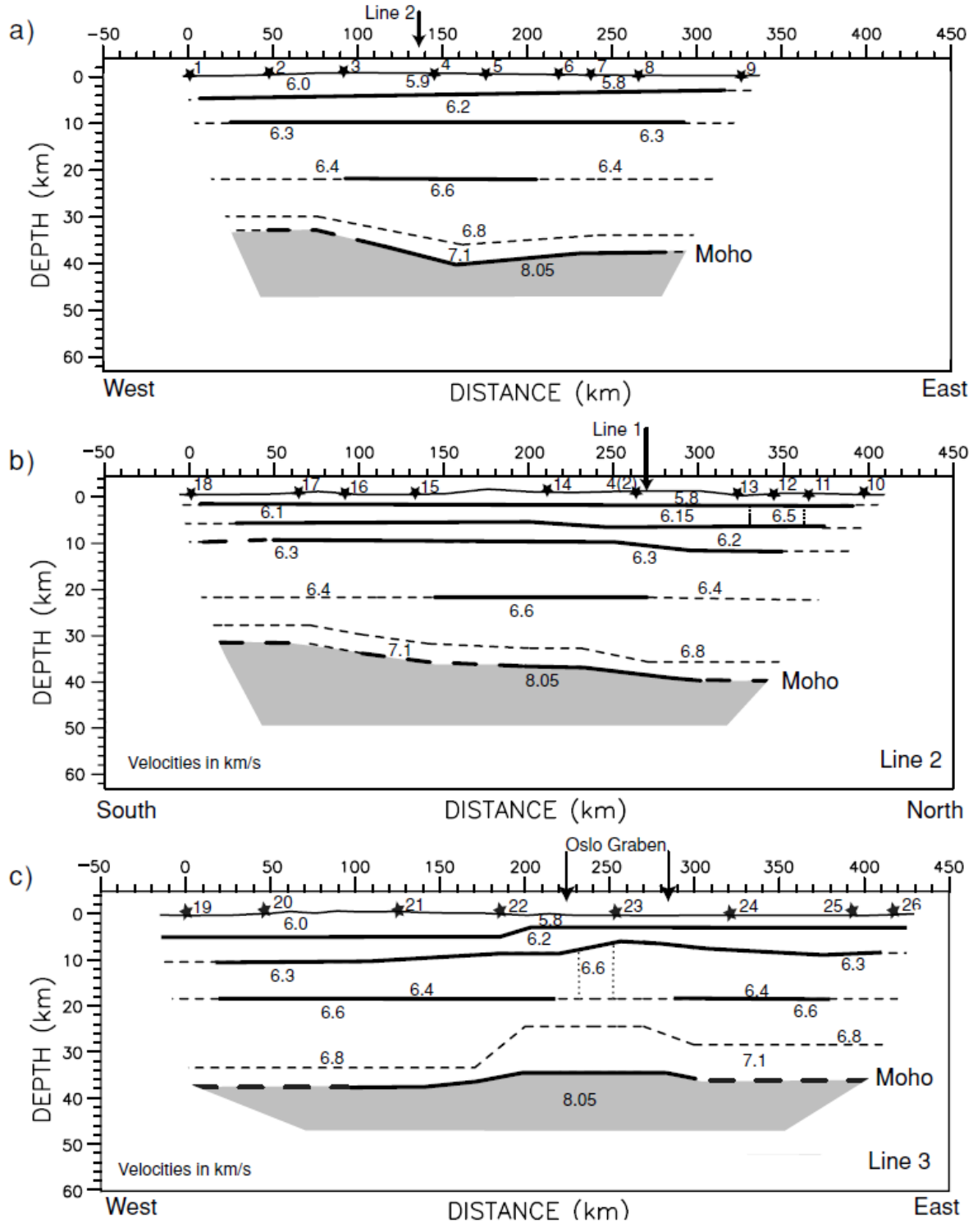

Fig. 6.1.2 (After Stratford et al., 2009) Forward modelling ray tracing solution for lines (a) 1, (b) 2 and (c) 3. The cross point between lines 1 and 2 is marked on the seismic models with labelled arrows. The surface expression of the Oslo Graben is marked on line 3.

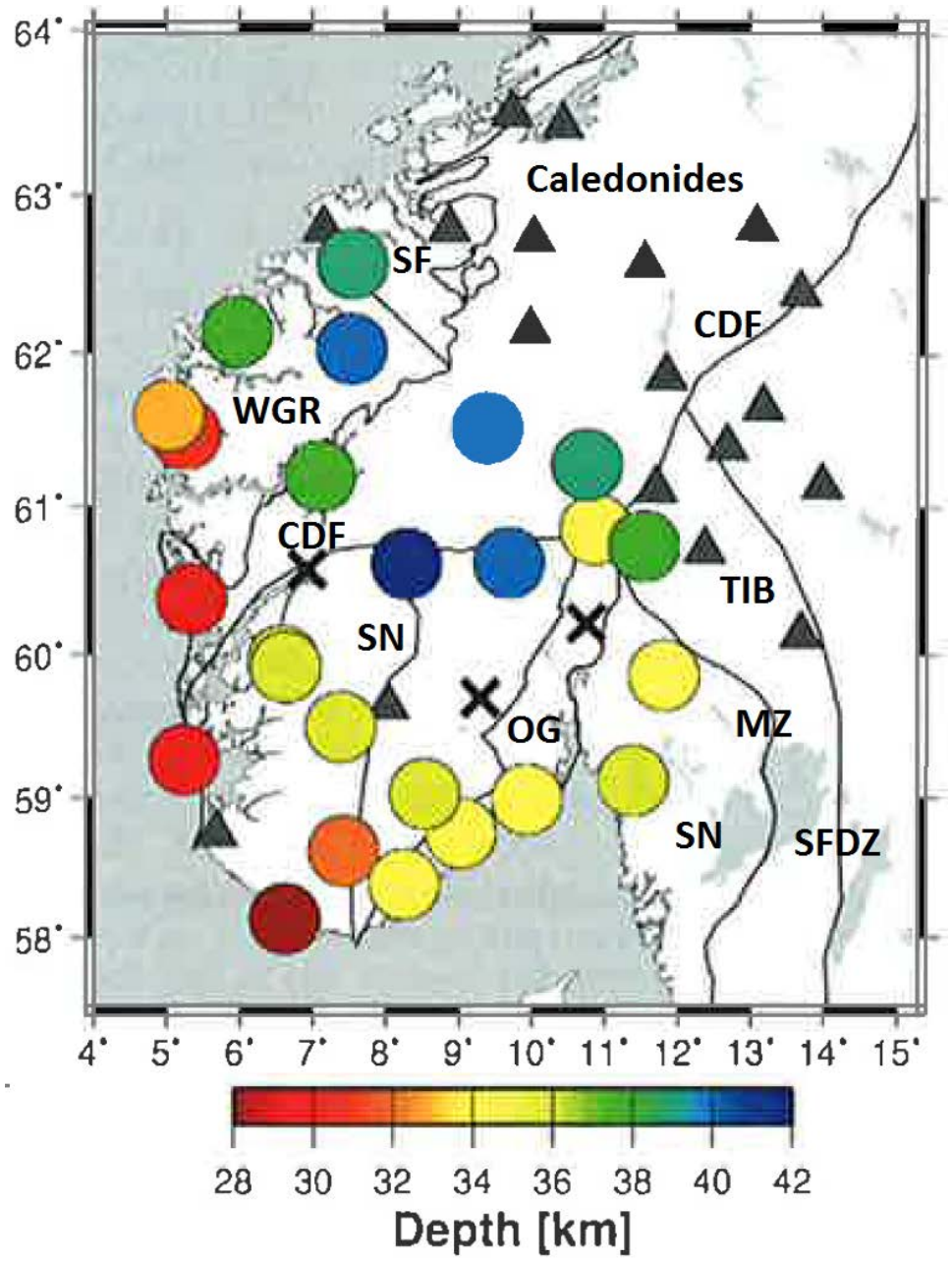

Fig. 6.1.3 (After Kolstrup, 2015) The Moho map. Colored circles indicate the Moho depths, grey triangles indicate locations of stations with gradual crust-mantle transition, black crosses indicate locations of stations where joint inversion was not performed, and black lines depict main geological units and boundaries: CDF, Caledonian front; MZ, Mylonite Zone, OG, Oslo Graben; SN, Sveconorwegian; SF, Sveconorwegian front; SFDZ, Sveconorwegian Frontal Deformation Zone, TIB. Transscandinavian Igneous Belt, WGR, Western Gneiss Region.

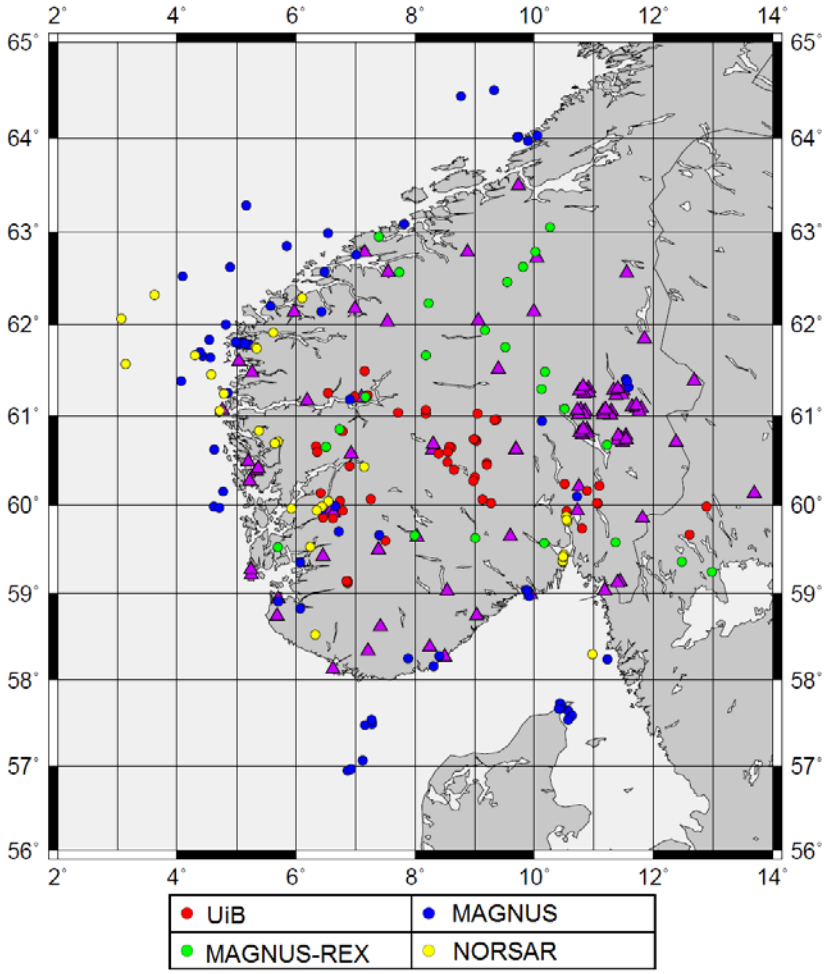

Fig. 6.1.4 Distribution of events used for development of the optimal 1-D velocity model for southern Norway. Triangles – seismic stations, circles – epicenters of seismic events: red – relocated events from the UiB catalog, blue – events from the MAGNUS project, green – explosions of the Magnus-REX project, yellow – events from the NORSAR catalog.

6.1.4 Development of the optimal 1-D velocity model

We performed inversions with the VELEST program using different settings, and defined optimal parameters for our dataset. We found that values of velocity and depth adjustments are, respectively, 0.2 km/s and 5.0 km for each iteration. We inverted for both P and S waves simultaneously, keeping the Vp/Vs ration equal to 1.74. We did not investigate the influence of different damping values and used the default values: 0.01 for epicenter coordinates, hypocenter depth and station corrections, and 1.00 for velocity values. The inversions with the VELEST program were performed in simultaneous mode. During each iteration (we performed 5 iterations) an inversion for all hypocenters and velocity model, including station corrections, was performed.

The input 1-D velocity models for both P and S waves were parameterized from the surface down to 80 km depth. Three different input velocity models were tested (Figure 6.1.5):

- Model ***b***: is the velocity model used by the UiB to locate seismic events in the southern part of Norway.

- Model ***mt***: is an averaged velocity model compiled from the results by Stratford and Thybo (2011) obtained from the MAGNUS project.

- Model ***m2***: is a modified ***mt*** model (i.e. fewer layers).

We analyzed the inversion results obtained with the different velocity models ***b***, ***mt*** and ***m2*** to define which one of them is the most suitable. We analyzed the data variance and final RMS values (Figure 6.1.6), distribution of the RMS values (Figure 6.1.7), hypocenter depth (Figure 6.1.8), and geographical distribution of hypocenter depths (Figure 6.1.9) and RMS values (Figure 6.1.10) of the relocated events. From the analysis we concluded that an optimal 1-D velocity model for southern Norway is the output model from the VELEST inversion with the input ***m2*** model (Table 6.1.1).

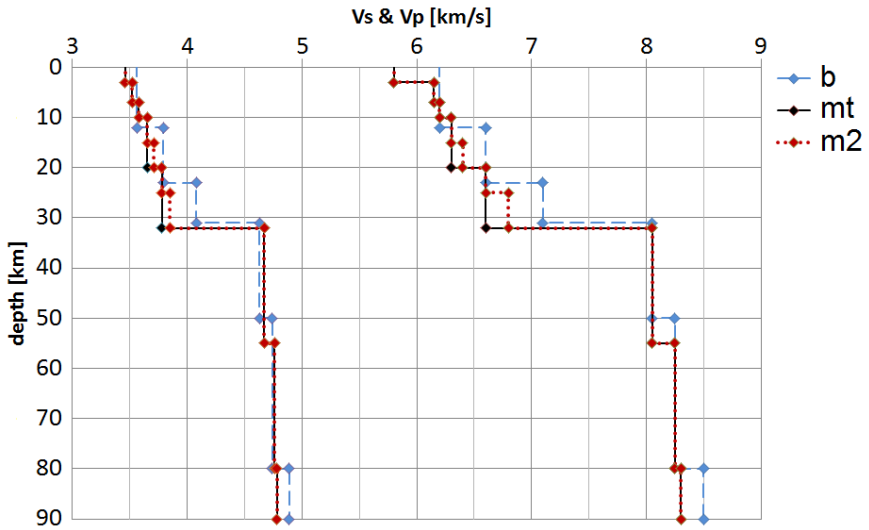

Fig. 6.1.5 Tested input velocity models b, mt and m2 for S waves (left curves) and P waves (right curves).

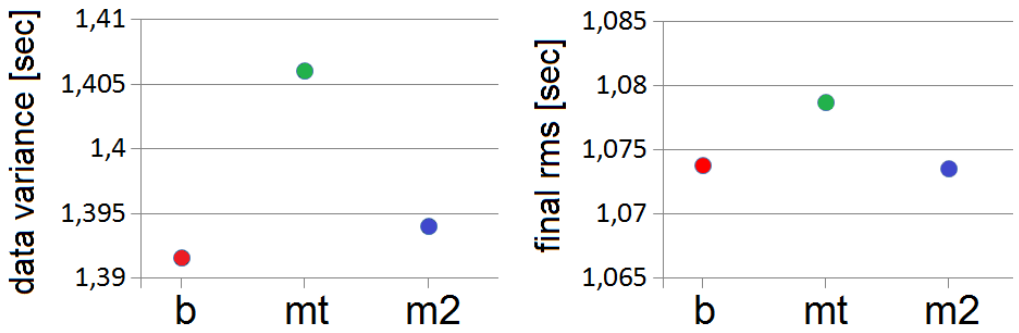

Fig. 6.1.6 Data variance and final RMS values after the VELEST inversions with different velocity models. Models are indicated on the abscissa.

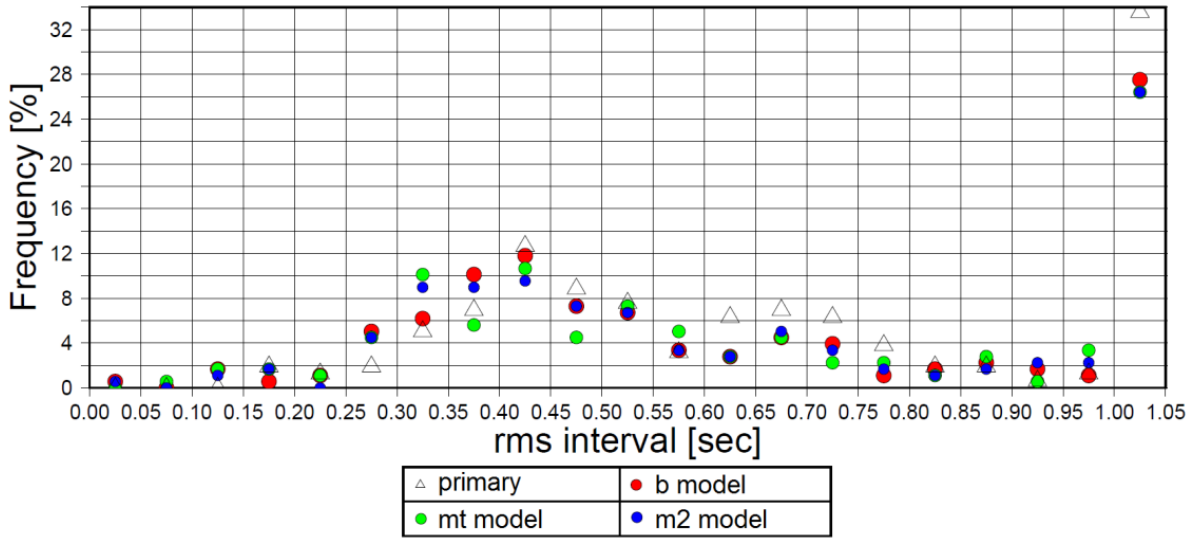

*Fig. 6.1.7 Distribution of the RMS values of the primary dataset (triangles) (from the original UiB seismological catalogs) and the output velocity models obtained using different input velocity models **b**, **mt** and **m2** (colorful circles).*

Table 6.1.1 Optimal 1-D velocity model for southern Norway. Seismic velocities of P and S waves are expressed in km/s, depth is in km. Moho boundary indicated by an arrow.

depth	Vp	Vs	Vp/Vs	
0.00	5.99	3.46	1.731	
3.00	6.18	3.50	1.765	
7.00	6.34	3.53	1.796	
10.00	6.46	3.70	1.746	
15.00	6.47	3.70	1.748	
20.00	6.52	3.74	1.743	
25.00	6.52	3.74	1.743	
32.00	7.76	4.35	1.784	← Moho
55.00	8.18	4.77	1.715	
80.00	8.30	4.78	1.736	

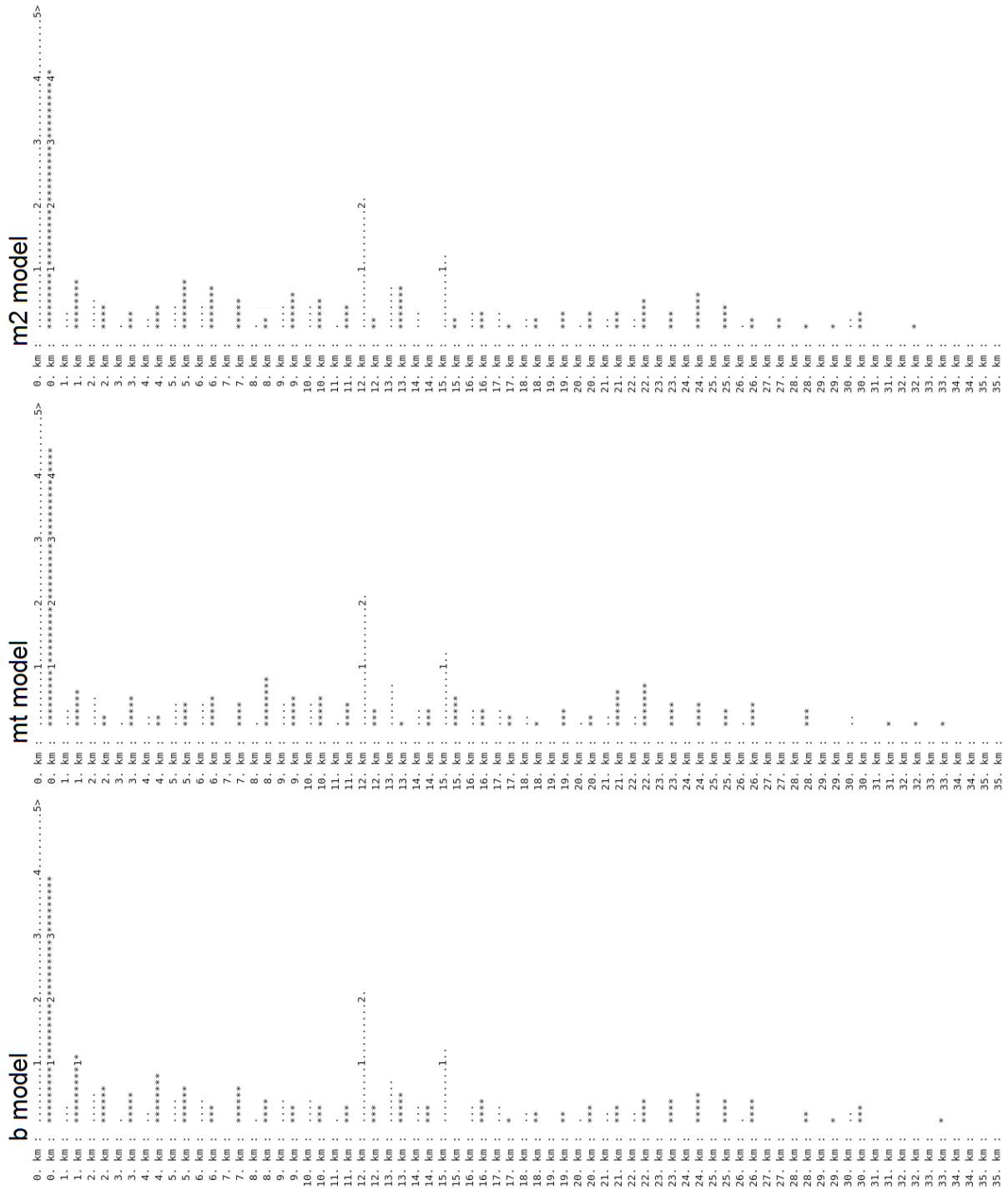

*Fig. 6.1.8 Distribution of depths of hypocenters after the VELEST inversions with different input velocity models **b**, **mt** and **m2**. Dots – primary depth values, stars – output hypocenter depths.*

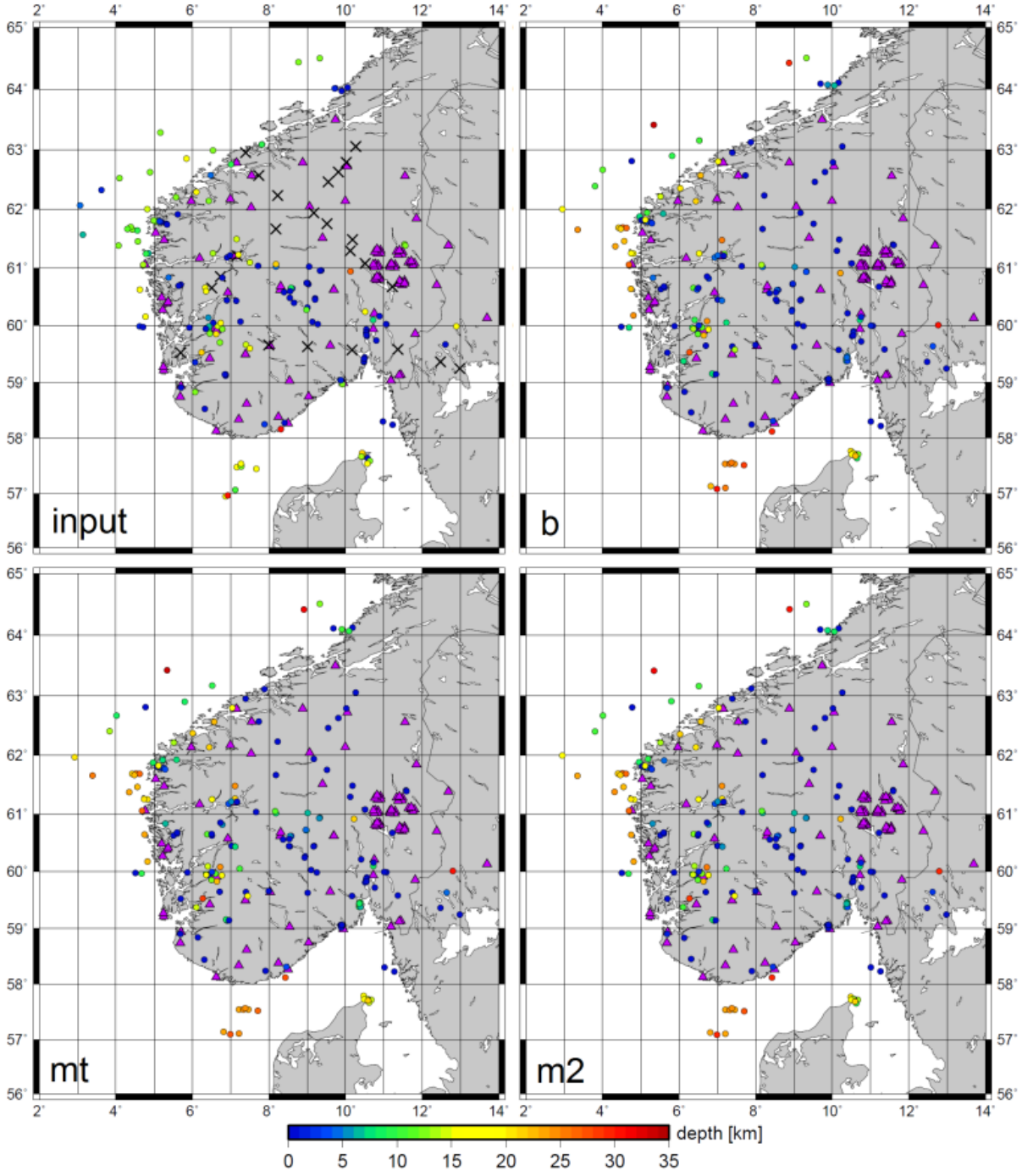

Fig. 6.1.9 Map of locations of events with indicated hypocenter depths for input and output of different models. x – explosions of the Magnus-REX project blasted close to the surface, circles – other seismic events. Depth of the explosions were fixed during the inversion.

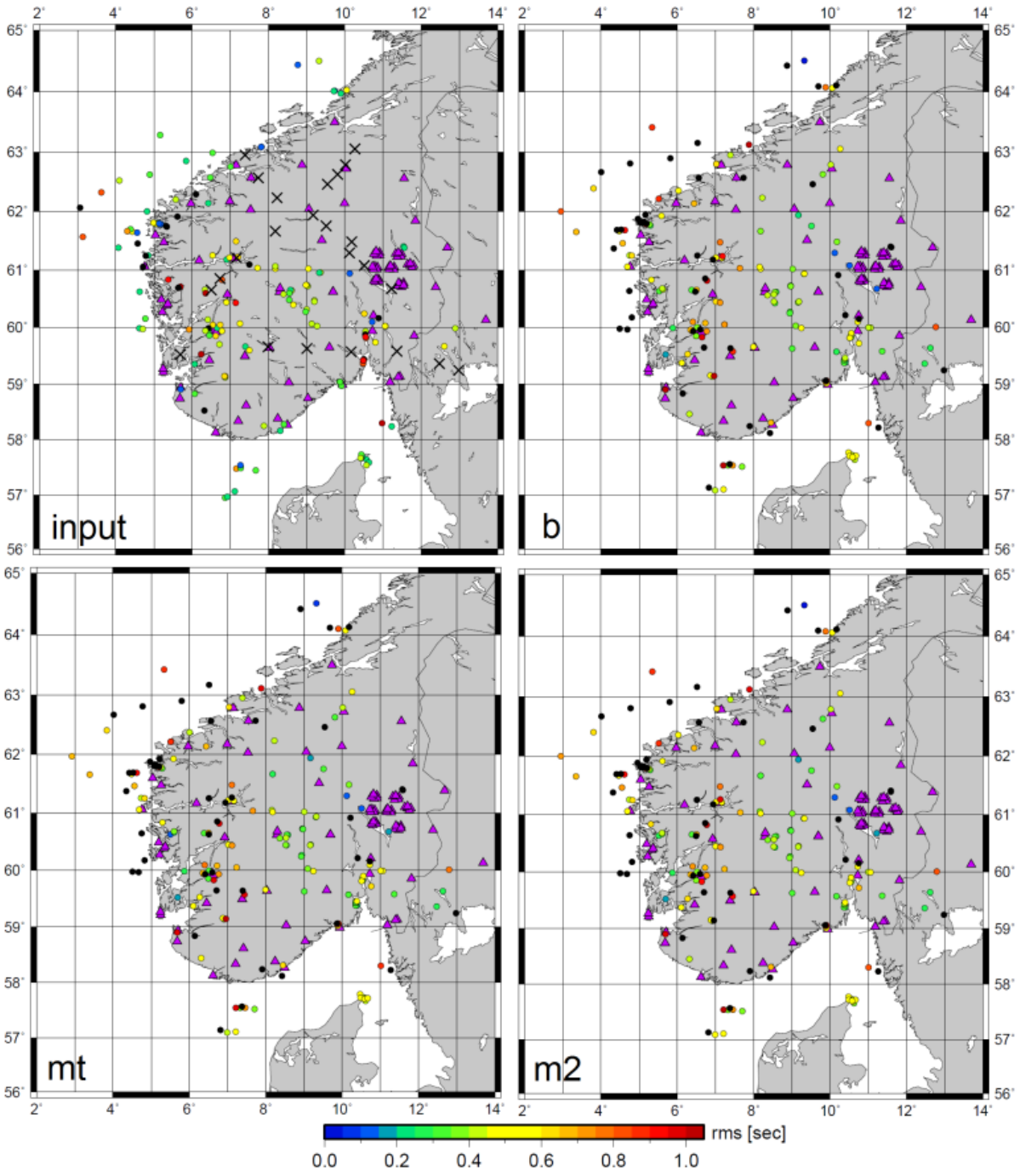

Fig. 6.1.10 Map of locations of events with indicated RMS value of the location for input and output of different models. x – explosions of the Magnus-REX project blasted close to the surface, circles – seismic events.

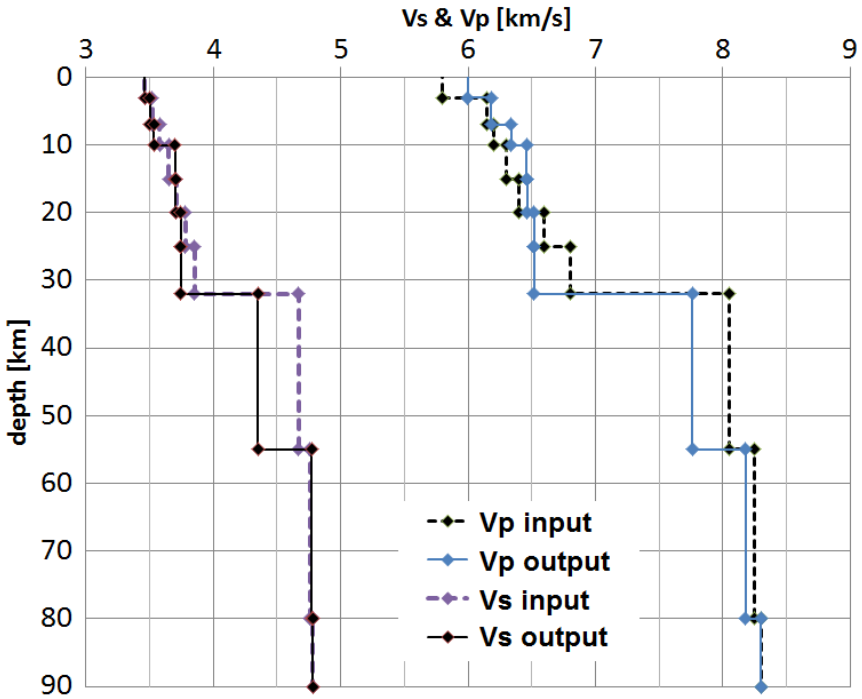

Fig. 6.1.11 Curves of m2 input and output velocity models for S (left) and P waves (right). The m2 output velocity model is regarded as an optimal 1-D velocity model for the southern part of Norway.

6.1.5 Development of the 3-D velocity model

6.1.5.1 Model parameterization

We defined the study area to 56-65° N latitude and 2-14° E longitude, and parameterized the model with two layers extending from the surface down to 80 km deep. The size of the model cells was selected taking into account the frequency content of the seismic signals and distribution of sources and receivers within the area. The size of the model cell is 0.9 degree in longitude and 0.7 degree in latitude, while the vertical spacing between the grid nodes is about 3 km in the upper layer and 4 km in the lower layer.

The 1-D velocity model (Figure 6.1.11) obtained with the VELEST program was used as a reference velocity model for further studies using the FMTOMO program. Before implementing the velocity model into the FMTOMO program, it was modified according to the studies by Stratford et al. (2009) and Stratford and Thybo (2011), and was transformed into a velocity model with two layers of gradient velocities increasing with depth (Figure 6.1.12). The upper layer extends from the surface to 32.1 km depth, and Vp in the layer gradually increases from 6.0 to 7.1 km/s, while the lower layer extends from 32.1 km to 80.0 km depth, and Vp in the layer changes from 8.05 to 8.30 km/s.

In the study we used damping of 1.0 for the velocity inversion and 0.1 for interface inversion. We did not investigate the influence of using different damping values.

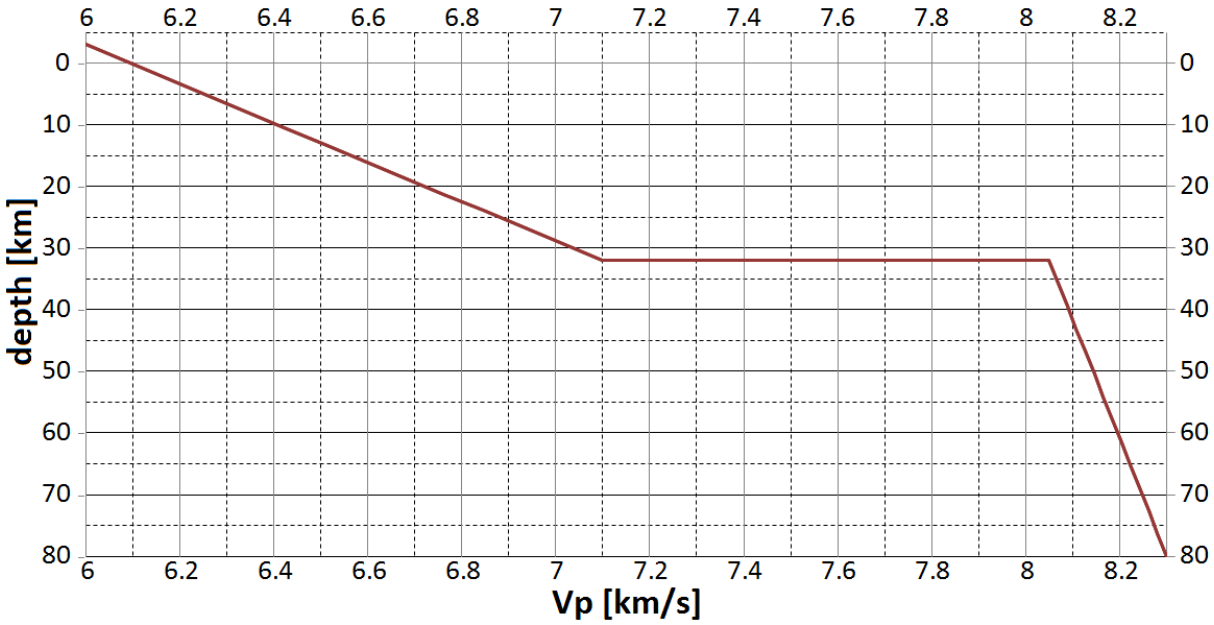

Fig. 6.1.12 Reference 1-D velocity model for southern Norway used to perform inversions with the FMTOMO program.

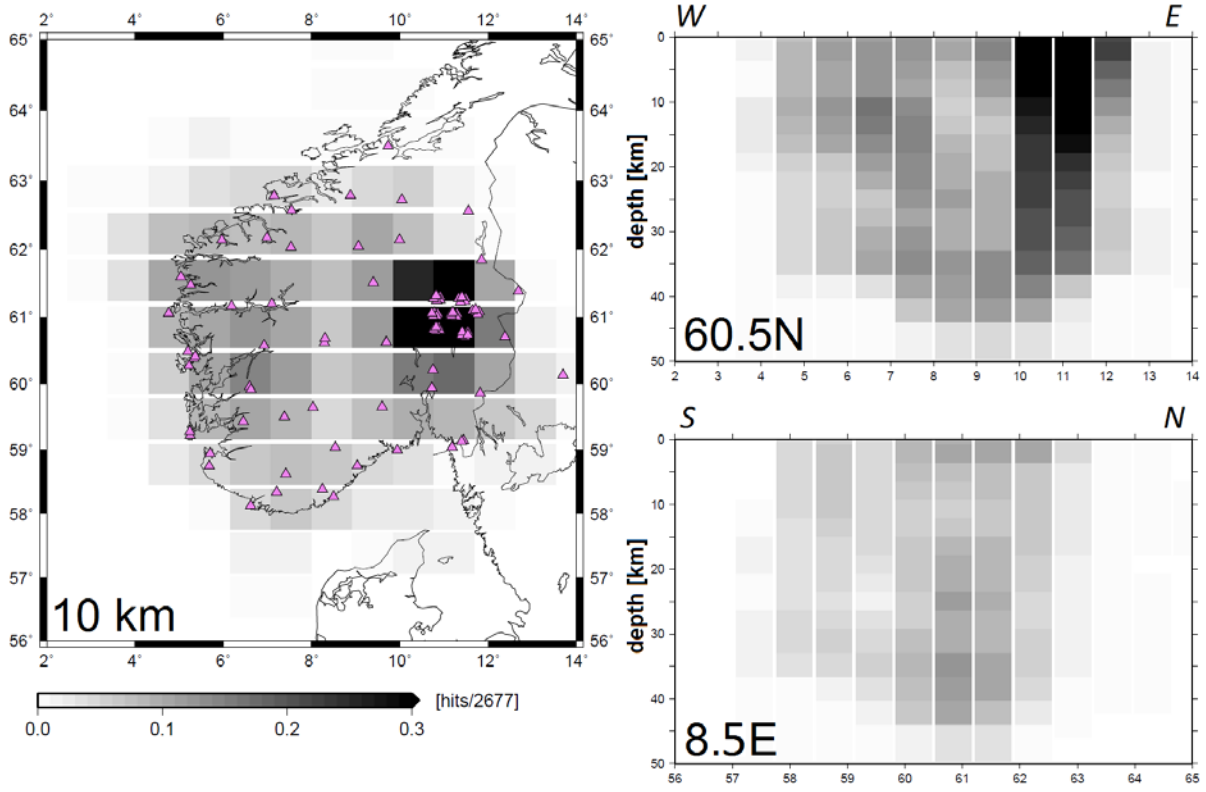

Fig. 6.1.13 Horizontal and two vertical perpendicular slices of the hit matrix in the study volume. The values are normalized to the total number of the rays.

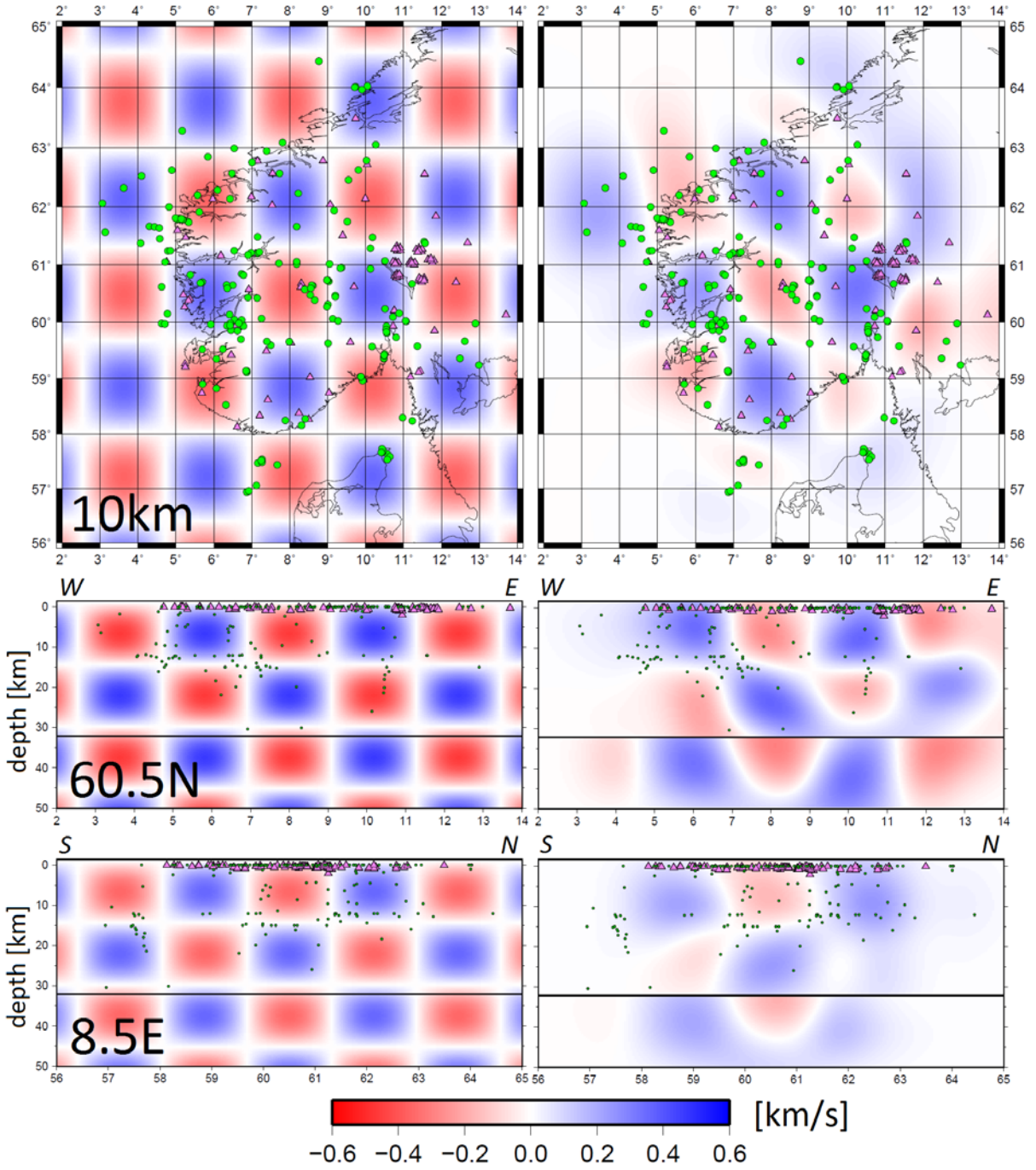

Fig. 6.1.14 Checkerboard test. (Left) Input checkerboard velocity model with synthetic blocks of ± 0.6 km/s velocity variations compared to the reference velocity model, and (right) the resolved model.

6.1.5.2 Resolution

Before analyzing the results with the real data it is very important to assess resolution. In this study we applied two methods: 1) the synthetic checkerboard test, and 2) the hit matrix, in order to obtain the ray coverage and define areas with good and poor resolution capabilities. The hit matrix shows how many rays cross the particular cell (Figure 6.1.13). However, the hit matrix method alone does not show the ray crossing, thus we need additional tools, such as checkerboard test, to define the regions, which could be confidently resolved with the current configuration of sources and receivers.

We used a synthetic checkerboard model (Figure 6.1.14) with synthetic blocks embracing two cells in all directions with alternating velocity variations of ±0.6 km/s compared to the reference velocity model. The inversion results with the checkerboard model show that the best resolved part of the study area is the central part down to about 35-40 km depth, while going to the outskirts the resolution depth decreases (Figure 6.1.14).

6.1.5.3 Inversion results

We performed an inversion with the real dataset and as a result we obtained a distribution of velocity variations within the study volume (Figure 6.1.15). In the inversion we introduced a constant Moho boundary at 32.1 km depth. The inversion was performed simultaneously for P wave perturbations and the Moho interface.

The model for seismic S waves can be obtained using the Vp/Vs ratios obtained from the VELEST program. The ratios are indicated in Table 6.1.1.

In the study we obtained a distribution of velocity variations within the study area from surface down to about 35-40 km depth (Figure 6.1.13, 6.1.14, 6.1.15). The amplitudes of velocity variations depend on the damping value, model grid, reference velocity model and errors in the dataset (i.e. phase picking). Our results show that P wave velocities in the areas with reasonable resolution vary about ±0.4 km/s compared to the reference velocity model. The higher velocity values are observed in the middle part of the study area, i.e. beneath the mountain plateau of southern Norway. We indicate that the deepest Moho boundary in this part is reaching 34-35 km, while the shallowest Moho of 31 km is found slightly to the north of the Oslo Graben. The shallow Moho depth is also found beneath the SW part of the study area, along the coast. Stratford et al. (2011) indicate a slightly deeper Moho boundary in the study area compared to our study. Their study indicates the deepest Moho at about 38-39 km beneath the mountain plateau and the shallowest Moho at about 32 km depth along the SW coast, while the study by Kolstrup (2015) indicates a variation of the Moho depth from about 40 km in the central part to about 28 km on the SW coast.

Oslo Graben is in many studies characterized as a pronounced tectonic structure (e.g. Stratford et al., 2011). Our results for the Oslo Graben indicate lower velocity values compared to the reference velocity model in the upper and the lower parts of the model, and slightly higher values between 10 and 15 km depth. Stratford et al. (2011) report on a higher velocity body beneath the Oslo Graben from 10 to 20 km. Stratford et al. (2011) estimate a Moho boundary at about 34 km depth, while we observe it at about 31 km, however, our checkerboard test indicates quite poor resolution at this depth.

In the southernmost part, most likely, we recognize a continuation of the most significant tectonic boundary in Europe, the Trans-European Suture Zone (TESZ); its northern part is called the Sorgenfrei–Tornquist Zone (STZ). The STZ in our results could be related with the higher velocity area extending downwards from at least 10 km. However, the resolution in this part is relatively poor.

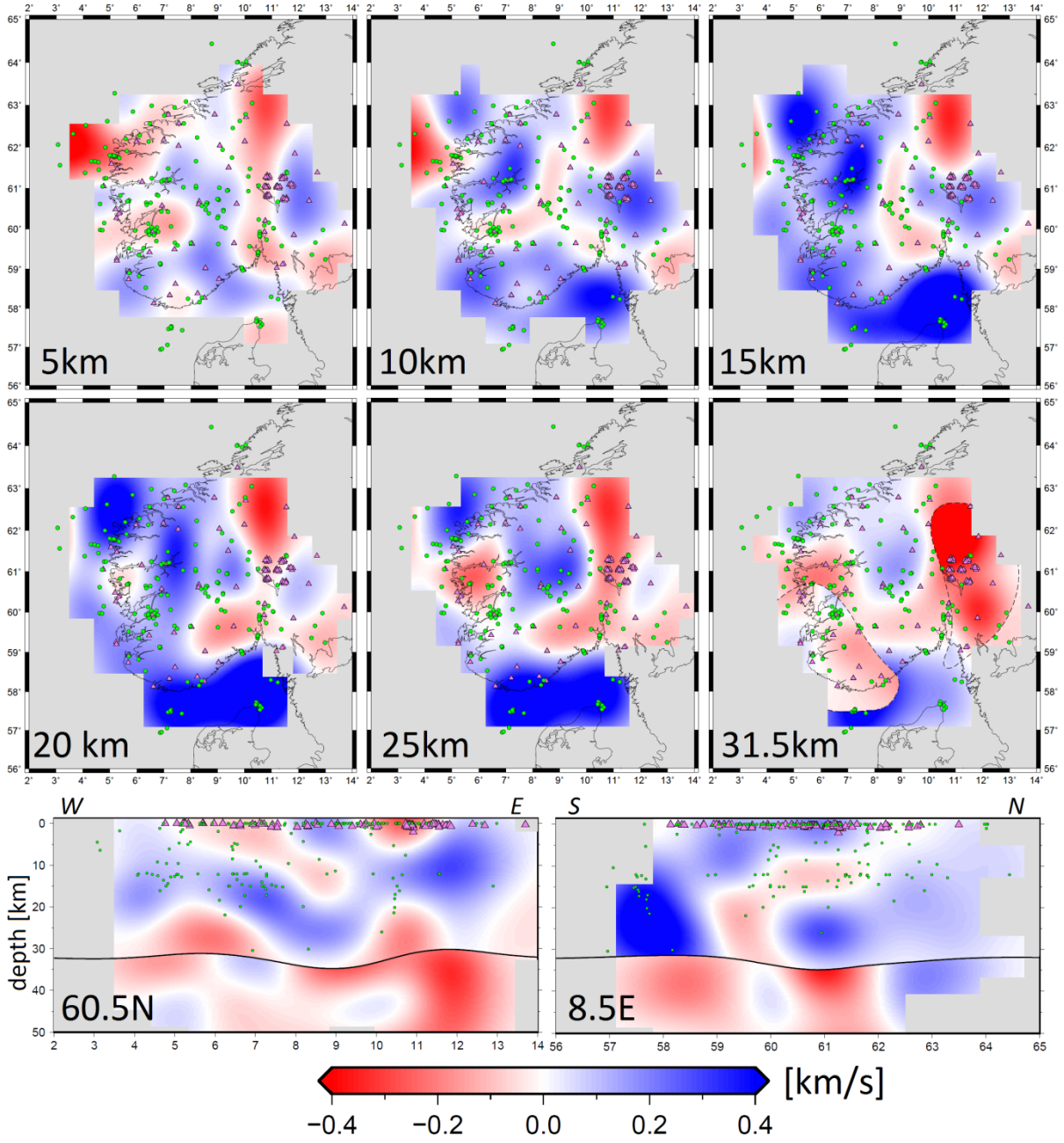

Fig. 6.1.15 Inversion results with the real dataset. Horizontal and vertical slices of the target volume are shown. Blue and red colors indicate velocity perturbations which are, respectively, higher and lower compared to the reference velocity model (Figure 6.1.12). Grey color indicates areas of poor ray coverage (less than 0.75 % of total ray hits). Dashed contours on the horizontal slice at 31.5 km depth and solid lines on vertical profiles mark the Moho intersection.

6.1.6 Conclusions

The main conclusions obtained from our study are as follows:

- The velocity perturbations vary ±0.4 km/s compared to the reference velocity model.
- The Moho boundary ranges from 31 km beneath the Oslo Graben and SW coast to about 35 km beneath the mountain plateau. However, the checkerboard test indicates relatively poor resolution below 35-40 km.
- The higher seismic velocities compared to the reference velocity model dominate under the mountain plateau.

I. Janutyte
T. Kværna

Appendix

Table 6.1.2 List of seismic events in Nordic format used to develop a velocity model for southern Norway. Notations: mmdd – month and day; ss.s – seconds, t – type of event at observation distance (L for local); latitu – latitude in degrees; longit - longitude in degrees; dept – depth in km; agg – reporting agency; st – number of stations with observations; res – location time residual in seconds; magTagg – magnitude, type of magnitude and the reporting agency.

Year	mmdd	hhmi	ss.s	t	latitu	longit	dept	agg	st	res	magTagg	magTagg	magTagg
2007	2	1	0211	26.1	L	57.063	7.120	10.4F	BER	26	0.2	1.7LBER	2.3CBER	1
2007	5	1	1411	30.1	L	57.644	10.572	0.0	BER	27	0.2	1.8LBER	2.3CBER	2.1LNAO1
2007	2	1	1426	8.7	L	61.177	6.904	0.0	BER	36	0.2	1.9LBER	1.6CBER	1.9LNAO1
2007	11	2	0818	3.3	L	62.852	5.844	15.9	TES	25	0.2	1.8LTES	2.2CTES	2.1WTES1
2007	10	2	1107	25.6	L	57.589	10.636	12.3	TES	30	0.2	1.8LTES	2.1WTES	1.9LNAO1
2007	10	2	1227	53.4	L	57.679	10.448	18.0	TES	24	0.2	1.7LTES	2.2WTES	1.8LNAO1
2007	10	2	1520	55.3	L	57.691	10.451	19.7	TES	25	0.2	1.7LTES	2.5CTES	2.2WTES1
2007	10	2	2000	3.8	L	57.703	10.460	17.0	TES	23	0.2	1.8LTES	2.2WTES	1.9LNAO1
2007	10	3	0959	37.0	L	57.666	10.424	5.3	TES	28	0.2	1.7LTES	2.6CTES	1.9LNAO1
2007	10	3	1235	19.9	L	57.735	10.430	21.4	TES	25	0.3	1.7LTES	2.4CTES	1.9LNAO1
2007	7	3	1425	1.9	L	58.163	8.313	30.1	BER	29	0.2	2.1LBER		2.0LNAO1
2007	10	3	2128	6.4	L	60.154	4.777	15.0	TES	42	0.3	2.1LTES	2.1WTES	2.0LNAO1
2007	5	4	0910	59.8	L	62.989	6.536	12.1	BER	44	0.3	2.2LBER	2.1CBER	2.2LNAO1
2007	7	4	1353	56.8	L	64.025	10.049	0.0F	BER	21	0.5	1.7LBER		2.1LNAO1
2007	7	4	1427	8.7	L	58.240	11.231	0.0	BER	16	0.2	1.4LBER		2.1LNAO1
2008	5	4	2257	23.9	L	62.525	4.095	12.1	TES	34	0.4	2.0LTES	2.4CTES	2.1WTES1
2007	12	5	1108	30.1	L	57.671	10.411	13.1	TES	13	0.4	1.6LTES	1.8WTES	1
2007	4	5	1736	7.6	L	60.621	4.628	16.1	BER	33	0.2	2.0LBER	1.7CBER	1.8LNAO1
2007	11	6	0907	59.0	L	59.662	7.399	14.7	TES	45	0.2	2.6LTES	2.6CTES	2.4LNAO1
2007	3	8	1055	42.1	L	64.015	9.735	0.0	BER	12	0.1	1.1LBER	2.5CBER	1
2007	12	8	1310	52.7	L	62.001	4.821	14.4	TES	12	0.2	1.2LTES	2.3CTES	1.4WTES1
2006	12	8	2240	13.8	L	57.477	7.160	15.0	BER	30	0.7	1.9LBER	1.0CBER	1
2008	4	9	1210	24.7	L	56.944	6.868	15.0	TES	26	0.3	2.1LTES	2.2WTES	1.8LNAO1
2008	4	9	1702	11.8	L	58.279	8.409	0.0	TES	23	0.3	1.5LTES	1.9WTES	1
2008	6	9	1900	7.0	L	62.202	5.571	12.1	TES	24	0.4	1.6LTES	1.7WTES	1
2006	1110	0854	20.0	L	60.938	10.128	26.0F	BER	20	0.1	1.5LBER	1.8WBER	1
2007	510	1341	13.8	L	61.803	5.104	4.7F	BER	39	0.1	2.1LBER	1.8CBER	1.8LNAO1
2007	110	2312	53.1	L	61.658	4.435	12.2	BER	46	0.5	2.5LBER	2.3CBER	2.2LNAO1
2007	111	1035	4.9	L	59.987	6.660	14.6	BER	30	0.2	1.9LBER	1.6CBER	2.0LNAO1
2006	1011	1200	25.3	L	61.784	5.193	1.5	BER	32	0.2	2.1LBER	1.5CBER	2.3WBER1
2008	612	1005	33.3	L	64.438	8.769	12.1	TES	10	0.1	1.9LTES	2.6CTES	1.9WTES1
2007	912	1413	42.9	L	59.038	9.862	2.6	BER	22	0.3	1.7LBER	2.2CBER	1
2008	212	1420	11.3	L	61.797	5.131	0.1	TES	25	0.3	1.8LTES	2.2WTES	2.0LNAO1
2007	1212	1427	15.8	L	59.024	9.888	0.0	TES	21	0.3	1.5LTES	1.7WTES	1
2008	612	1619	9.8	L	64.502	9.327	12.1	TES	6	0.4	1.3LTES		1

```
2007  912 2256 41.5 L  61.699   4.386 12.1  TES 50 0.3 2.9LTES 2.7WTES 2.8LNAO1
2007 1113 1731 20.0 L  63.088   7.814  9.6  TES  9 0.1 1.0LTES 1.5WTES        1
2007 1115 1432 36.2 L  58.826   6.071 12.2  TES 27 0.3 1.7LTES 1.9WTES        1
2007 1115 1514 27.8 L  58.966   9.916 12.1  TES 20 0.3 1.4LTES 1.6WTES        1
2008  615 2211  3.6 L  59.950   6.426  8.5  TES 31 0.3 1.7LTES 1.7WTES        1
2008  416 1453  7.5 L  61.404  11.540 12.1  TES 18 0.2 1.6LTES 2.2WTES 2.2LNAO1
2007  317 0006 27.0 L  59.702   6.715 12.1  BER 47 0.4 2.2LBER 1.9CBER 2.1LNAO1
2006 1117 1213 28.0 L  59.355   6.070  1.9  BER 19 0.2 1.2LBER 2.1CBER 1.3WBER1
2007  417 1216  0.1 L  61.785   5.177  0.0  BER 33 0.1 2.0LBER 1.4CBER 2.0LNAO1
2007  118 1205 27.7 L  59.983   4.624  1.2  BER 33 0.2 2.0LBER 1.9CBER 2.0LNAO1
2007  118 1213  3.7 L  59.973   4.712  0.0  BER 30 0.4 2.0LBER 1.5CBER 1.8LNAO1
2007  419 0419 29.5 L  64.008   9.713  1.0  BER 12 0.2 1.1LBER 2.2CBER        1
2007 1219 1333 52.6 L  57.511   7.272 12.6  TES 24 0.3 2.0LTES 2.2WTES        1
2006 1219 1740 40.8 L  61.315  11.586 22.4  BER 20 0.2 1.7LBER 2.1CBER 1.9WBER1
2007  920 1100 38.3 L  61.802   5.078  9.6  TES 18 0.2 1.8LTES 2.0WTES 2.0LNAO1
2006  920 1143 23.7 L  63.284   5.166 12.8  BER 21 0.3 1.9LBER 1.9CBER 2.0WBER1
2007  821 0153 47.3 L  58.251   7.883  2.4  BER 19 0.4 1.3LBER 2.0CBER        1
2007  121 1345 22.4 L  62.571   6.477  4.8  BER 48 0.3 3.6LBER 3.5CBER 3.8LNAO1
2007  521 2022 13.3 L  61.641   4.565  9.2  BER 42 0.1 2.3LBER 2.1CBER 2.1LNAO1
2007  622 0542  2.2 L  61.249   4.856  6.1  BER 39 0.2 1.9LBER 1.9CBER        1
2007  222 0722 20.3 L  62.756   7.009  9.0  BER 31 0.3 2.0LBER 1.9CBER 2.0LNAO1
2008  522 1259  2.2 L  61.787   5.043 12.2  TES 40 0.4 2.2LTES 2.5WTES 2.1LNAO1
2008  222 1321  4.9 L  61.792   5.076 12.2  TES 26 0.5 1.9LTES 1.8CTES 2.2WTES1
2008  122 1339  0.3 L  61.809   4.991 12.7  TES 34 0.5 2.0LTES 2.3WTES 2.1LNAO1
2008  424 0059 19.4 L  62.138   6.430 12.1  TES 35 0.2 1.7LTES 1.9WTES        1
2007  724 1224 41.2 L  61.777   5.225  3.5  BER 31 0.3 1.9LBER 1.7CBER        1
2007  524 1316 19.5 L  58.906   5.702  0.2  BER 14 0.1 1.4LBER                 1
2008  124 1851 51.3 L  57.488   7.272 12.1  TES 37 0.3 2.5LTES 2.4WTES 2.4LNAO1
2008  525 0110  5.6 L  60.097  10.718  7.6  TES 45 0.1 2.7LTES 3.0CTES 2.9LNAO1
2006  925 1244 57.4 L  57.542   7.269 17.2  BER 26 0.1 2.1LBER 1.9CBER 1.9LNAO1
2008  425 1522 46.4 L  59.036   9.879  1.1  TES 28 0.3 1.6LTES 1.8WTES        1
2008  425 1806  7.3 L  57.540  10.569 16.1  TES 34 0.4 1.9LTES 2.2WTES 2.1LNAO1
2007  627 1230 18.0 L  61.796   5.142  2.0  BER 39 0.1 2.0LBER 1.7CBER        1
2007  727 2330 22.2 L  61.832   4.545 18.9  BER 42 0.1 2.1LBER 2.0CBER 1.9LNAO1
2007  928 2156  8.3 L  56.961   6.923 30.4  TES 27 0.2 2.0LTES 2.2WTES 2.0LNAO1
2008  529 0828 49.5 L  62.623   4.894 12.8  TES 39 0.3 2.4LTES 2.3WTES 2.7LNAO1
2008  229 1308 28.4 L  61.382  11.562 12.1  TES 20 0.2 1.6LTES 2.1WTES 2.1LNAO1
2007  130 0834  5.5 L  61.381   4.073 12.4  BER 32 0.2 1.6LBER 1.9CBER 1.9WBER1
2007  530 1125 54.9 L  63.969   9.899  0.0  BER 27 0.2 2.0LBER                 1
2009  424 1837 10.5 L  60.162  10.883  0.0  EXP 13 1.2 2.0LEXP 2.7CEXP 2.2LNAO1
2009  6 7 1730 56.7 L  60.134   6.415  5.5  EXP 15 0.4 1.9LEXP 2.1CEXP 1.7LNAO1
2009  610 2247 46.4 L  61.223   7.202 15.0  EXP 11 0.6 1.5LEXP 2.1CEXP        1
2009 1030 0058 14.7 L  60.217  11.092 15.0  EXP 13 1.0 1.7LEXP 2.5CEXP 1.2LNAO1
2010  421 1752 29.0 L  61.032   7.713  0.4  EXP 11 0.5 1.0LEXP 1.9CEXP        1
2010  615 0422  3.8 L  60.829   6.784  0.0F EXP 15 0.8 1.5LEXP 2.2CEXP 2.1LNAO1
2010 10 8 0408 32.3 L  59.598   7.501 15.0F EXP 13 0.5 1.5LEXP 2.5CEXP 1.8LNAO1
2011  112 0601 53.7 L  60.238  10.509 15.0  EXP 24 0.6 1.8LEXP 2.2CEXP 1.9LNAO1
2011  327 1134 20.8 L  59.983  12.892 15.0  EXP 12 0.4 1.9LEXP 3.0CEXP 2.0LNAO1
2011  428 2224  6.6 L  59.938   6.782 12.0F EXP 16 0.5 2.0LEXP 2.3CEXP 2.0LNAO1
2011 1111 2049 55.9 L  59.857   6.451 12.1  EXP  9 0.3 1.0LEXP 2.1CEXP        1
2011 1223 1418 20.8 L  60.655   6.337 15.0  EXP  9 0.4 1.4LEXP 1.8CEXP        1
2012  124 1454 51.9 L  59.850   6.622 20.9  EXP 12 0.6 1.3LEXP                 1
2012  324 1106 30.8 L  60.598   6.353 15.0  EXP 51 1.0 3.0LEXP         3.2LNAO1
2012  328 1527 37.8 L  60.436   6.897  0.0  EXP 10 0.5 1.6LEXP                 1
2012  426 0518 28.9 L  60.065   7.255  0.0  EXP 26 0.5 1.9LEXP         1.9LNAO1
2012 1030 0357 26.9 L  61.250   6.539 13.4  EXP 13 0.5 1.4LEXP                 1
2013  2 5 1056  3.7 L  60.393   8.656  0.0  EXP 10 0.5 1.2LEXP                 1
2012 1127 1425 53.6 L  60.019  11.066  0.1  EXP 10 0.5 0.9LEXP                 1
2013  325 1448 24.9 L  59.666  12.609  0.0  EXP 11 0.5 1.1LEXP                 1
2013  415 1451 31.4 L  60.642   8.609  0.1  EXP 14 0.4 1.4LEXP                 1
2013  527 1206 25.4 L  59.934  10.544  0.0  EXP 11 0.4 1.3LEXP                 1
2013  613 1112  1.2 L  59.115   6.868  0.0  EXP  9 0.4 1.0LEXP                 1
2013  619 1831  5.1 L  61.212   6.985  0.0  EXP 20 0.5 1.4LEXP                 1
2013  626 1304  0.6 L  61.022   9.046  0.0  EXP 12 0.5 1.2LEXP                 1
2013  7 1 0911 17.2 L  61.018   8.182  4.3  EXP 10 0.5 1.1LEXP                 1
2013  7 4 1509 26.8 L  59.138   6.870  0.0  EXP 13 0.6 1.0LEXP                 1
2013  7 9 1040 42.1 L  60.025  11.052  0.0  EXP 11 0.5 1.2LEXP                 1
2013  723 1359 31.2 L  59.138   6.847  0.1  EXP 13 0.6 1.1LEXP                 1
2013  723 1648 50.7 L  60.956   9.363  0.0  EXP 26 0.4                 1.7LNAO1
2013  828 1443 23.6 L  60.718   9.031  0.0  EXP 14 0.4 1.3LEXP                 1
2013  9 3 1339 11.3 L  61.062   8.183 21.8  EXP 10 0.4 1.0LEXP                 1
2013  9 3 1715 32.2 L  60.738   9.001  0.0  EXP 12 0.4 1.0LEXP                 1
2013  911 1708 58.3 L  60.738   8.982  0.0  EXP 14 0.5 1.5LEXP                 1
2013  920 0127  0.7 L  60.043   6.735 17.3  EXP 26 0.6 2.4LEXP         2.4LNAO1
2013  926 1214 28.4 L  59.738  10.803  0.0  EXP 11 0.5 1.2LEXP                 1
2013 1016 1900  4.1 L  60.063   9.135  0.1  EXP 12 0.4 0.8LEXP                 1
2013 1022 1221  1.1 L  60.025   9.273  0.0  EXP 13 0.4 1.3LEXP                 1
```

```
2013 1024 1213 52.3 L  60.313   9.005  0.1  EXP  9 0.4 1.3LEXP                1
2013 1113 1544 16.6 L  60.578   8.394  0.0  EXP 16 0.4 1.4LEXP                1
2013 1119 2341  8.2 L  61.490   7.152 14.0F EXP 36 0.6 2.9LEXP 2.9WEXP 2.7LNAO1
2013 12 3 1612 44.3 L  60.652   8.576  8.6  EXP 11 0.2 1.3LEXP                1
2013 12 5 1158  3.6 L  60.950   9.331  0.0  EXP 21 0.2 1.4LEXP         1.7LNAO1
2013 1210 1256  5.9 L  60.598   8.552  0.0  EXP 10 0.3 1.2LEXP                1
2013 1210 1735 12.2 L  60.474   9.202  0.0  EXP 16 0.4 1.5LEXP                1
2013 1211 1505  8.1 L  60.481   8.544  0.0  EXP 13 0.3 1.1LEXP                1
2013 1217 0945 23.3 L  60.274   8.979 11.4  EXP 10 0.3 1.0LEXP                1
2013 1219 1404 31.9 L  60.450   9.202  0.1  EXP 13 0.4 1.2LEXP                1
2014 0108 2048 11.8 L  61.568   3.141  6.4  NAO 11 0.8                 1.6LNAO1
2014 0115 1934 55.9 L  60.430   7.143       NAO 17 0.9                 2.1LNAO1
2014 0118 1425 10.6 L  60.045   6.546       NAO 16 0.6                 2.0LNAO1
2014 0119 0644 24.4 L  59.984   6.434  6.3  NAO  9 1.1                 1.6LNAO1
2014 0121 0639 03.4 L  61.053   4.717 13.6  NAO 14 1.3                 2.4LNAO1
2014 0123 0432 49.7 L  61.243   4.790  9.6  NAO 19 1.2                 2.6LNAO1
2014 0220 1320 47.2 L  61.753   5.319       NAO  7 1.1                 2.0LNAO1
2014 0224 1339 20.2 L  58.299  10.974       NAO  9 1.0                 2.1LNAO1
2014 0227 1502 19.4 L  60.831   5.381  4.4  NAO  9 0.9                 1.9LNAO1
2014 0308 1038 20.3 L  61.455   4.575 12.5  NAO  9 1.4                 1.9LNAO1
2014 0401 0947 25.9 L  59.357  10.480       NAO 17 0.8                    LNAO1
2014 0401 1235 29.5 L  59.442  10.498       NAO 15 1.2                    LNAO1
2014 0402 0737 02.1 L  59.394  10.478       NAO 13 1.1                 1.7LNAO1
2014 0402 0812 50.0 L  59.366  10.481       NAO 16 0.8                 1.8LNAO1
2014 0402 1044 54.5 L  59.413  10.493       NAO 14 0.8                 2.1LNAO1
2014 0402 1107 24.2 L  59.814  10.556       NAO 15 0.8                 1.8LNAO1
2014 0402 1226 01.7 L  59.419  10.484       NAO 16 0.9                 2.4LNAO1
2014 0402 1308 44.7 L  60.707   5.695       NAO  7 1.0                 1.6LNAO1
2014 0402 1432 15.4 L  59.877  10.538       NAO 15 1.1                 2.3LNAO1
2014 0402 1635 10.0 L  59.832  10.545       NAO 14 0.9                 1.7LNAO1
2014 0404 2330 48.6 L  59.963   5.920       NAO  6 0.7                 1.8LNAO1
2014 0408 0650 12.3 L  62.322   3.625  1.8  NAO 16 0.8                 2.7LNAO1
2014 0503 1724 20.2 L  59.526   6.240 21.9  NAO  9 1.0                 1.7LNAO1
2014 0505 1334 48.1 L  62.288   6.101 18.4  NAO  7 1.5                 2.4LNAO1
2014 0512 1604 46.1 L  61.739   5.338       NAO  8 1.1                 2.0LNAO1
2014 0523 1318 51.2 L  58.528   6.321       NAO  4 1.5                 1.7LNAO1
2014 0616 1231 04.7 L  60.689   5.652       NAO  6 0.9                 1.9LNAO1
2014 0623 1100 52.8 L  60.692   5.646       NAO  8 1.2                 1.7LNAO1
2014 0626 0131 15.5 L  61.911   5.619       NAO  8 1.1                 1.9LNAO1
2014 0702 0528 28.0 L  62.064   3.069  4.5  NAO  7 1.4                 1.8LNAO1
2014 0705 1334 30.5 L  61.666   4.303 11.9  NAO  8 0.7                 2.0LNAO1
2014  9 6 1656 38.1 L  59.942   6.347  0.2  BER 24 0.4 2.4LBER                1
2007 1001 1939 52.0 L  62.568 007.733  0.0F                                   1
2007 1001 1950 05.0 L  61.293 010.123  0.0F                                   1
2007 1001 2000 06.6 L  62.948 007.390  0.0F                                   1
2007 1001 2009 52.7 L  61.751 009.515  0.0F                                   1
2007 1001 2020 00.0 L  59.242 012.984  0.0F                                   1
2007 1001 2030 19.5 L  63.053 010.265  0.0F                                   1
2007 1001 2040 14.9 L  62.627 009.809  0.0F                                   1
2007 1001 2051 24.8 L  62.461 009.546  0.0F                                   1
2007 1001 2101 03.3 L  61.209 007.163  0.0F                                   1
2007 1001 2110 01.2 L  60.848 006.733  0.0F                                   1
2007 1001 2120 04.7 L  61.074 010.511  0.0F                                   1
2007 1001 2129 59.9 L  62.233 008.223  0.0F                                   1
2007 1001 2340 01.7 L  59.630 009.010  0.0F                                   1
2007 1002 0400 02.2 L  59.657 007.990  0.0F                                   1
2007 1002 1949 53.1 L  61.482 010.183  0.0F                                   1
2007 1002 2009 57.6 L  60.675 011.223  0.0F                                   1
2007 1002 2019 47.4 L  62.789 010.020  0.0F                                   1
2007 1002 2030 00.9 L  61.939 009.168  0.0F                                   1
2007 1002 2040 00.4 L  61.663 008.183  0.0F                                   1
2007 1002 2050 00.8 L  60.652 006.504  0.0F                                   1
2007 1002 2210 03.9 L  59.581 011.363  0.0F                                   1
2007 1002 2230 02.7 L  59.525 005.698  0.0F                                   1
2007 1003 0150 00.9 L  59.363 012.481  0.0F                                   1
2007 1003 0210 05.0 L  59.573 010.167  0.0F                                   1
```

References

Andersen, T.B. (1998). Extensional tectonics in the Caledonides of southern Norway, and overview. *Tectonophysics*, 285, 333–351.

Balling, N. (1980). The land uplift of Fennoscandia, gravity field anomalies and isostasy. In *Earth Rheology, Isostasy and Eustasy* (ed. Mørner, N.A.), John Wiley & Sons, New York, pp. 297–321.

Faleide, J.I., Kyrkjebø, R., Kjennerud, T., Gabrielsen, R.H., Jordt, H., Fanavoll, S. and M.D. Bjerke (2002). Tectonic impact on sedimentary processes during the Cainozoic evolution of the northern North Sea and surrounding areas. *Geol. Soc. London Spec. Publication*, Vol. 196.

Kissling, E. (1995). Program VELEST user's guide – Short introduction. Institute of Geophysics, ETH Zurich, Second draft version 5th October, 1995.

Kolstrup, M.L. (2015). Old structures and plumes? – New geophysical investigations of the crust and upper mantle in southwestern Scandinavia. Doctoral dissertation, University of Oslo, Faculty of Mathematics and Natural Sciences, Department of Geosciences, ISSN 1501-7710, Nr. 1615, pp.147.

Lidmar-Bergstrøm, K., Ollier, C.D. and J.R. Sulebak (2000). Landforms and uplift history of southern Norway. *Global Planet. Change*, 24, 211–231.

Ottemoller, L., Voss, P.H. and J. Havskov (2014). SEISAN EARTHQUAKE ANALYSIS SOFTWARE FOR WINDOWS, SOLARIS, LINUX and MACOSX , 2014.

Rawlinson, N., and M. Sambridge (2005). The fast marching method: an effective tool for tomographic imaging and tracking multiple phases in complex layered media. *Exploration Geophysics* 36 (4), 341-350.

Roberts, D. and D.G. Gee (1985). An introduction to the structure of the Scandinavian Caledonide Orogen. John Wiley & Sons, Chichester.

Sellevoll, M.A. and R.E. Warrick (1971). A refraction study of the crustal structure in southern Norway. *Bull. seism. Soc. Am*., 61, 457–471.

Stratford, W., Thybo, H., Faleide, J.I., Olesen, O., and A. Tryggvason (2009). New Moho Map for onshore southern Norway. *Geophys. J. Int*, 178, 1755–1765.

Stratford, W. R., and H. Thybo (2011). Seismic structure and composition of the crust beneath the southern Scandes, Norway. *Tectonophysics*, Vol. 502, No. 3-4, p. 364-382.

6.2 The DPEP Long-Period Detector for the NOA Broadband Array

6.2.1 Introduction

Since the NOA array upgrade to broadband sensors on all 42 sites in 2012, no automatic procedure was operating at NORSAR to analyze the new long-period part of the data. A long-period detector is therefore designed for near real-time, automatic detection focusing on teleseismic long-period surface-wave signals, specifically Rayleigh waves, using the broadband data from all 42 vertical sensors of the array.

Surface waves consist of Raleigh and Love waves, which can be recorded on horizontally and vertically oriented seismic sensors. Horizontal components are usually recording a mixture of Rayleigh and Love waves, which have different propagation characteristics. The detector searches for Rayleigh waves only, as these signals are easier to detect than Love waves. It is possible to isolate Rayleigh from Love waves by using vertical-component recordings only. This also allows exploiting the full beamforming power using all 42 vertical channels of the NOA array. Because of the large aperture of the NOA array, we focus on processing of teleseismic / far regional events where plane-wave approximation of the arriving wavefronts is valid.

Surface waves are dispersive, which means that their propagation velocity is frequency dependent. The goal of the developed detection routine is to detect the different portions of the incoming dispersive Rayleigh waves. To do that, the processing parameters had to be made frequency dependent. Real-time recognition of surface waves can be a significant improvement in nuclear explosion monitoring as well as a useful tool for earthquake seismology and noise analysis. A major issue is the differentiation between microseismic noise and seismic surface wave signals, as the polarization characteristics of these two signal types are of the same kind (Rayleigh waves) and their frequency and velocity contents are also very similar.

The new array processing algorithm for long-period data at NORSAR consists of two steps:

1. Detection Processing (DP).
2. Signal Attribute Processing (SAP).

These steps have been implemented by extensions to the NORSAR DP/EP program systems (Fyen 1987, 1989). Detection Processing (DP) consists of an STA/LTA detection and beamforming procedure. The STA/LTA detection processing parameters were found to be frequency dependent and were set for optimized triggering of the dispersive Rayleigh wavetrains. The steering parameters of the beam with the highest signal-to-noise ratio (SNR) are used as initial estimates of the apparent velocity and backazimuth (BAZ) of the detected signal.

During the Signal Attribute Processing (SAP) the detection parameters are refined. Onset time analysis is performed to find the best phase onset of the triggering signal and to estimate its dominant period, while a broadband frequency-wavenumber (f-k) analysis of the filtered data estimates its apparent velocity and backazimuth (BAZ). After beamforming with the SAP-estimated apparent velocity and BAZ values, the signal amplitude is measured and the onset time and dominant period are again recalculated.

To validate the results of the new processing algorithm, the detected Rayleigh-wave phases have been associated to and compared with seismic events reported in CTBTO's International Data Centre (IDC) Reviewed Event Bulletin (REB).

6.2.2 DP

The main goal of the Detection Processing is to detect the incoming dispersive Rayleigh waves using different frequency bands. In order to take account for the dispersion of surface waves, the array beams processed by the detector are constructed using multiple bandpass filter – propagation velocity combinations.

6.2.2.1 Frequencies

To reduce computing time, the original 40 Hz raw data are low-pass filtered and decimated to 1 Hz, yielding a Nyquist frequency of 0.5 Hz.

By assuming a minimum propagation velocity of 3.1 km/s of the arriving signals, the large-aperture geometry of the NOA array provide correct, spatially un-aliased sampling of signals up to a period of 40 seconds. For signals with higher propagation velocities this limit can be reasonably well extended to 50 second periods.

At very low frequencies, man-made noise has little influence on seismic recordings. The main noise sources at NOA in the long-period data are primary (6 – 8 s) and secondary (12 – 16 s) ocean microseisms. These are often referred to as “ocean noise”, and are often pronounced at the NOA array, which is located only $\sim$ 200 km from the North Atlantic Ocean. Atmospheric low pressure systems are regularly observed in the North Atlantic, and are very strong sources of microseisms. The dominant BAZ at NOA of these signals varies between 225° and 345° and thus also coincident with parts of the seismicity in the Pacific Ocean region. These BAZ values, previously observed by e.g., Köhler et al. (2011), have been also confirmed during the detector testing. Since microseisms have the form and particle motions of propagating Rayleigh waves (Haubrich et al., 1963, Longuet-Higgins, 1950) and are very coherent among the different traces (see Figure 6.2.1), ocean noise can lead to incorrect classification of Rayleigh wave signals from earthquakes. Secondary microseisms have, as mentioned above, typical periods of 12 – 16 s. This means that these kind of microseisms are broadly overlapping in the period range with the shorter surface-wave periods of about 10 – 20 s. Since empirical tests on the available data showed that teleseismic Rayleigh waves recorded at NOA have little energy at shorter periods, the DPEP LP detector analyzes data in the 10 – 50 s period range to avoid both aliasing and the influence of primary microseisms.

6.2.2.2 Dispersion curves

For the DPEP LP Detector, the dispersion curves computed by Köhler et al. (2012) are used as reference for the expected dispersion behavior of Rayleigh waves. For each NOA subarray, Köhler et al. (2012) report phase- and group-velocity dispersion curves in the 3 – 70 s period range. Since differences among the NOA subarrays are small, a single set of filter – velocity combinations samples the whole set of dispersion curves. Numerous real-data tests show a clear correlation between the reference phase-velocity curve and the observed frequency-depending propagation velocities estimated by f-k analysis on the triggered signals. Therefore, the applied filter-velocity combinations used by the DPEP LP Detector (Table 6.2.1) are based on the Rayleigh wave phase-velocity curves.

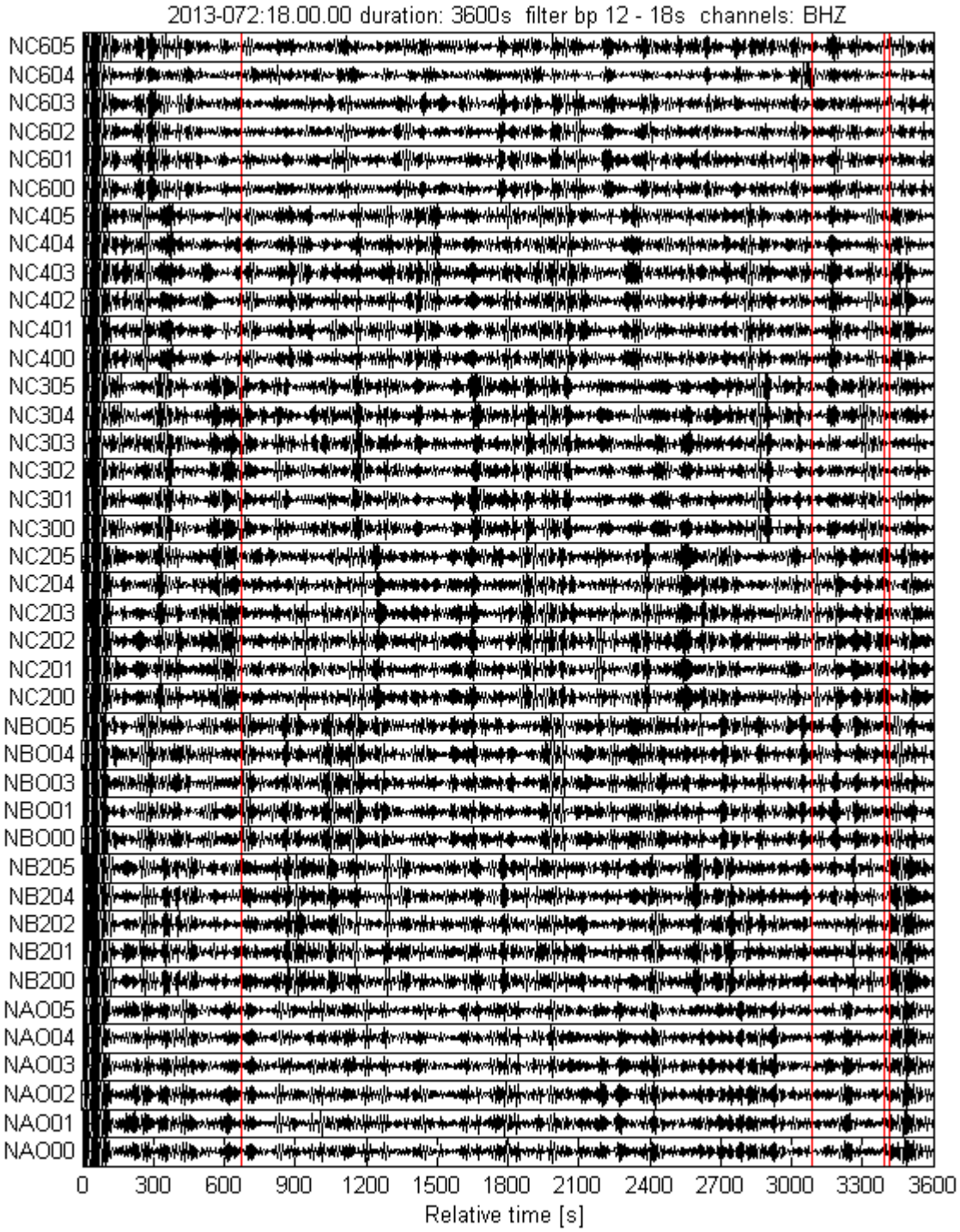

Fig. 6.2.1 Trace stack for 41 available (out of in total 42 total) vertical channels, showing records of 13 March 2013 at 18.00 in the 0.02 – 0.1 Hz frequency band. Most of the visible signals are due to ocean microseisms, whose coherency can be seen among the traces. The red lines are microseism-triggered signals. At the beginning of the record, a filtering artifact can be observed.

6.2.2.3 Filter – velocity combinations

The filter-velocity combinations are set to sample the chosen reference-phase-velocity dispersion curves. To reduce the influence of the secondary ocean microseisms we use filters with a relatively wide bandwidth. A set of six filters covers the period range of interest (10 – 50 s), where the lower frequency of each filter is always half of the upper frequency limit (Table 6.2.1). The geometrical progression of the filter bandwidths provides a sufficiently large bandwidth to reduce the detector sensitivity in the noisy 10 – 20 s range, and also prevents any monochromatic signal oscillations to be present in any filter band. The order of the Butterworth filters is set to the standard value of 3 to avoid ringing artifacts.

Table 6.2.1 Ranges (F1 – F2 Hz or T1 – T2 s) of the chosen Butterworth bandpass filters, their middle periods and the corresponding phase velocity used for beamforming.

f1 [Hz]	f2 [Hz]	T1 [s]	T2 [s]	Mid T[s]	Phase Velocity [km/s]
0.05	0.1	20	10	15	3.4
0.04	0.08	25	12.5	18.25	3.5
0.033	0.066	30	15	22.5	3.6
0.028	0.057	35	17.5	26.25	3.7
0.025	0.05	40	20	30	3.8
0.020	0.04	50	25	25	3.9

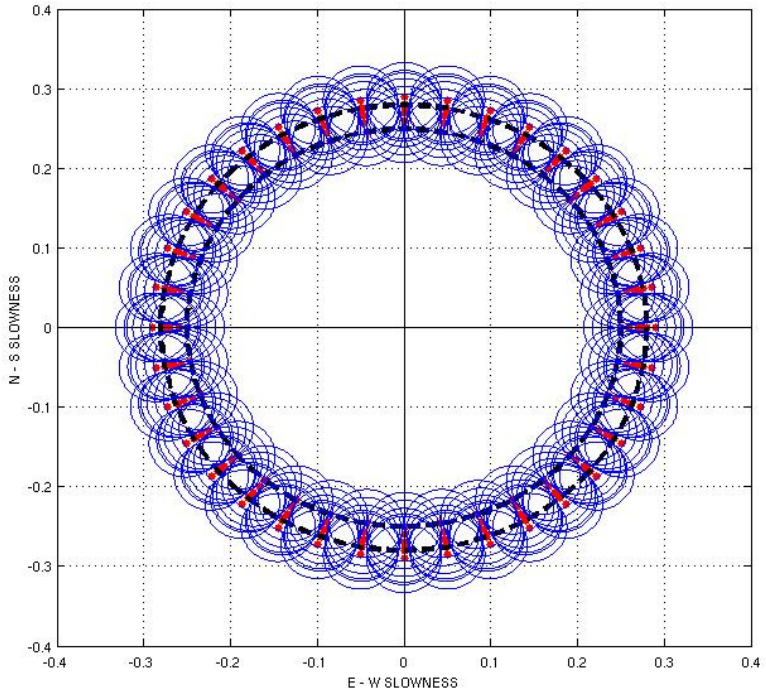

Fig. 6.2.2 Horizontal slowness plot displaying the set of steering parameters for the detection beams computed by the DPEP LP Detector. Red points show the beam steering points and the surrounding circles represent a radius of 10 degrees. The black dotted lines show reference velocity/slowness values of 3.5 and 3.9 km/s for surface waves.

6.2.2.4 Beamforming

The DPEP LP Detector computes a set of multiple beams at selected BAZ intervals, using the six different filter-velocity combinations listed in Table 6.2.1. Figure 6.2.2 shows the coverage in slowness space of the different detection beams. Empirical tests demonstrated that a 10° BAZ sampling yields good resolution in terms of recognizing the true seismic wave source direction (see Figure 6.2.3.

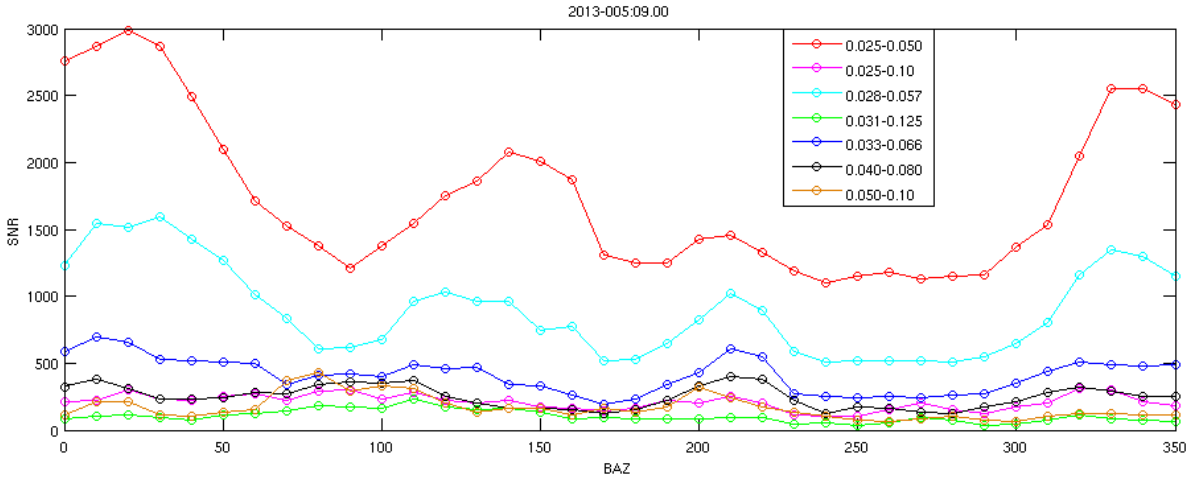

Fig. 6.2.3 The curves are showing the SNR of the detections found on all 216 beams computed in a time window including only the P-wave arrival of the 5 January 2013 08:58, Mw 7.5 Alaska event. It is clearly possible to recognize the source BAZ from the SNR maxima. The theoretical BAZ of the arriving signal is ~0°. Different curves represent different bandpass filters, as shown in the figure legend.

6.2.2.5 STA/LTA detector

STA/LTA parameters test

After beamforming, an STA/LTA detection algorithm runs on each of the computed beams. This allows detecting and extracting apparent velocity and BAZ of the triggering signal in the different frequencies. The parameters of the STA/LTA algorithm are tuned to maximize SNR values for Rayleigh waves only, in order to obtain a “clean” Rayleigh wave observation list while reducing the number of noise triggers and body-wave detections. This can be achieved by setting most of the parameters to be frequency-dependent.

For more detailed information on the definition of the different used STA/LTA parameters see Schweitzer et al. (2011) and Trnkoczy (1999). In order to optimize the settings of the detection parameters STA length, LTA delay, STA delta, and the LTA update parameter SIGMA, we first investigated the detection SNR of signals from three teleseismic earthquakes with good long-period signal radiation (Bougainville region, Papua New Guinea, 19 April 2014 13:28, Mw 7.5; Offshore Tarapaca, Chile, 1 April 2014 23:46, Mw 8.1 ; Vancouver Island, Canada, 24 April 2014 03:10, Mw 6.5).

The SNR has been investigated by systematically changing the STA length from 1/f1 to 1/f2, the LTA delay from 1/f2 to a maximum of 500s and of SIGMA from 4 to 8, where f1 and f2 refer to the higher and lower corner frequency of the Butterworth bandpass filters (see Table 6.2.1). The highest SNR is found for an STA length of 1/f2 s and an STA up-date interval delta of 1.0 s.

The results obtained with these values produce a very rugged SNR trace with several peaks, leading to a large number of triggers. The best compromise between resolution and non-redundant information has been achieved by smoothing the SNR trace by changing STA length and STA delta values to 2/f2 s and 2.0 s, respectively. The SNR loss caused by the smoothing is low and acceptable; as it affects mostly unwanted high SNR body wave phases (see Figure 6.2.4).

In the final implementation, the triggering SNR threshold is set to 4.5, the LTA delay to *4/f2* s and LTA smoothing parameter SIGMA to 5 (see Figure 6.2.5).

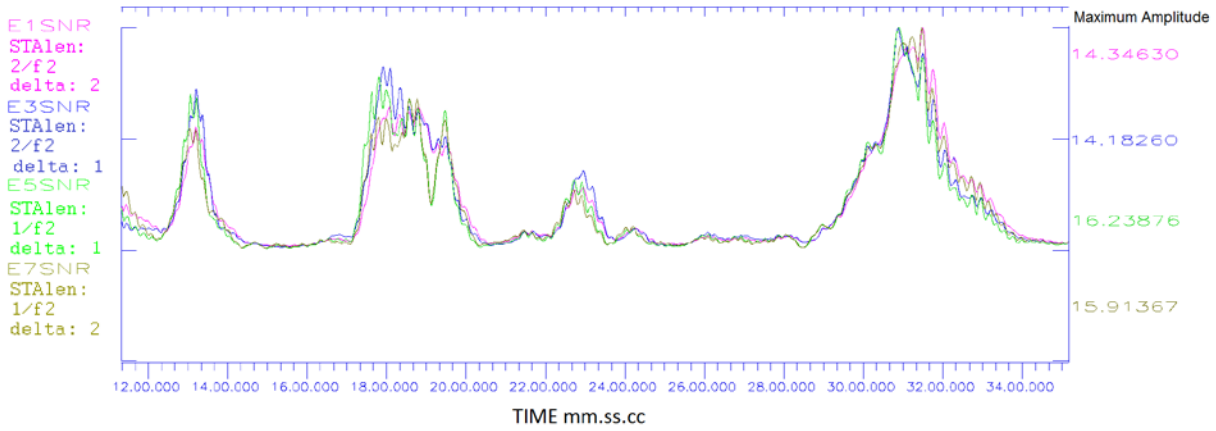

Fig. 6.2.4 SNR trace for later body waves and Rayleigh waves arrivals from the 5 January 2013 08:58, Mw 7.5 Alaska event. Each trace is calculated using different STA length and STA delta values. The trace names with the processing parameters are shown to the left.

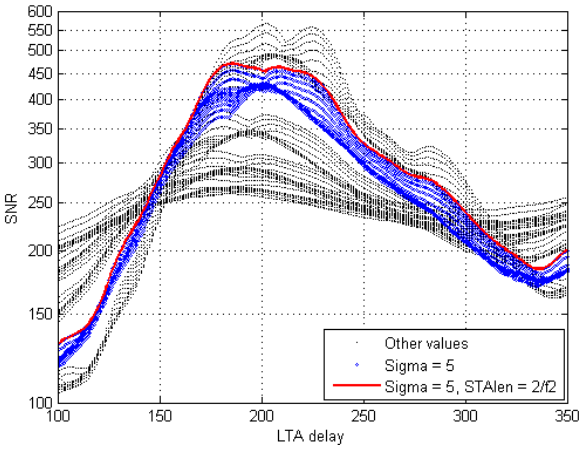

Fig. 6.2.5 Relationship between LTA delay and max SNR for data from the 19 April 2014 13:28, Mw 7.5 Papua New Guinea event. The max SNR for the Rayleigh-wave package is shown for all tested sigma, STA length and LTA delay values. Blue dots are computed with a sigma value of 5, while the red line is computed using the sigma-STA length combinations later implemented in the near-real time processing at NORSAR.

Reading and detecting

The detection processing employs the aforementioned STA/LTA parameters. To reduce the number of triggers within each signal, a detection reduction algorithm is running on each filtered beam. The procedure is summarized as follows, where *T* is the central period of the filter bands (see Table 6.2.1):

Triggers within a time window of 3*T are grouped as one detection

After a time period of 4*T, triggers are seen as part of a new signal.

The dependency on the different frequencies of the filters (and thus to an average period of the expected signal) allows the algorithm to merge triggers coming from high frequency SNR oscillations, while at the same time setting a reasonable limit to time-separate lower frequency signals.

After detection reduction, the detections are reported in an ASCII file (DPX file). For each group of triggered beams, only the parameters of the beam with the highest SNR are listed.

6.2.3 The signal attribute processing (SAP)

The DPX detection lists are then used as input for the parameters refinement operated in the SAP.

6.2.3.1 Onset time estimation

This part of the processing follows the original structure of the RONAPP processing package (Mykkeltveit and Bungum, 1984). Onset time estimation acts on each detection and is tuned to be dependent on the corner frequencies of the filters applied to the beams. The algorithm backtracks in time starting from the detection time, which is the time at which the signal exceeds the SNR threshold. This is usually quite different from the true signal onset time. The onset estimation process also estimates the signal period, which is fundamental to fine-tune the later processing related to the expected signal dispersion. Three parameters are set to stop the backtracking:

1) Maximum length of backtracking in [s]: **4*T1.** T1 is the longest period of the filter cutoff (see Table 6.2.1)

2) Minimum ratio (*first cycle amplitude / RMS noise level)*: **2.0**

3) Minimum ratio (*first cycle amplitude / maximum signal amplitude)*: **0.6**

The noise RMS is calculated in a time window starting *(T1 + T2)* before the detection time and backtracking by (*3 * T1)*. The maximum amplitude search is made in a *+/- T1* long time window around the detection time.

6.2.3.2 F-k analysis

Following the first onset time estimation, broadband f-k analysis (Kvaerna and Doornbos, 1986) is applied to the analyzed signal. The length of the time window is set to be frequency dependent. The length of the time window *t* should include at least a few periods of the signal (in our case ~6) and sample the slowest propagating frequency component. The window length is thus set to $t = a*T + d$, where *T* is the signal period estimated by preceding onset analysis. *a* is a user-defined constant which is set to larger values for the slow velocities typical of Rayleigh waves. *a* is introduced to take into account the longer duration of surface-wave signals, which travel with a lower velocity than S-waves. The *d* value is the minimum duration of the time window, which is set according to the slowness resolution of the array.

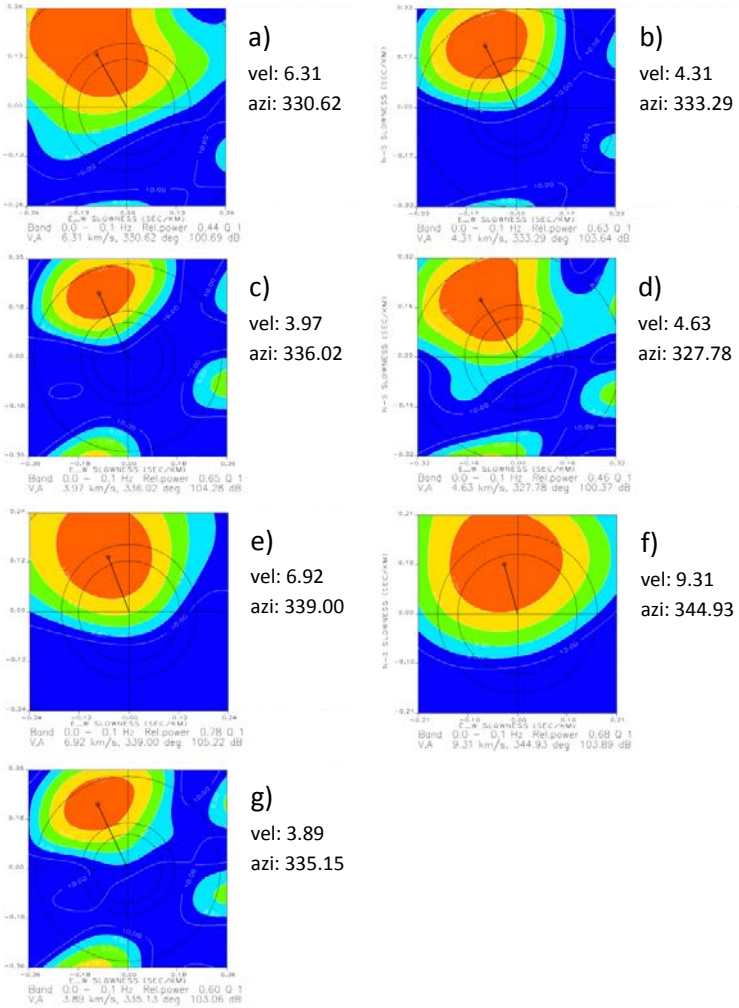

Fig. 6.2.6 Broadband f-k spectra computed in the different time windows for a single triggered phase of the 5 January 2013 08:58, Mw 7.5 Alaska earthquake:
***a**) Centered at the onset time from the onset estimation procedure; **b**) centered at the detection time; **c**) centered 2 x T1 after the detection time; **d**) centered 2 x T1 before the detection time; **e**) centered at the detection time with a window length of T1; **f**) centered at the onset time with half-long time window; **g**) centered at the onset time with 1.5 x long time window.*

The broadband f-k analysis is applied to a set of 7 to 8 different time windows having different start and end times, different durations, and centered either on the detection (trigger) time or the estimated onset time. The f-k analysis results from these different choices can differ significantly (see Figure 6.2.6). The apparent velocity and BAZ estimated in the time window having the highest value of (SNR * f-k power) is reported from the f-k analysis.

6.2.3.3 The f-k beam

A new beam is calculated using the velocity and BAZ reported from the f-k analysis. On this so-called f-k beam, a second search for the onset is made, using the same procedure as described in section 6.2.3.1. The SNR of the detection is also reestimated on the f-k beam using the reestimated onset time. Due to local noise and scattering of the long-period seismic energy, several detection beams with quite different BAZ values can exceed the SNR threshold, and the BAZ value of the detection beam with the highest SNR may not correspond to the "true" BAZ of the arriving signal. However, the beams calculated after fk-analysis ("f-k beams") show major differences if compared to the beams computed by the DP processing before the f-k analysis. For the f-k beams the SNR of seismic noise detections is lowered, and the consistency of the BAZ estimates for each event is much more stable than for the BAZ reported by the initial detector (DP), as shown in Figures 6.2.7 and 6.2.8. This improvement is due to optimizing the analysis window (onset time estimation) and the denser slowness gridding of the fk-analysis, as compared with the DP beam gridding shown in Figure 6.2.2.

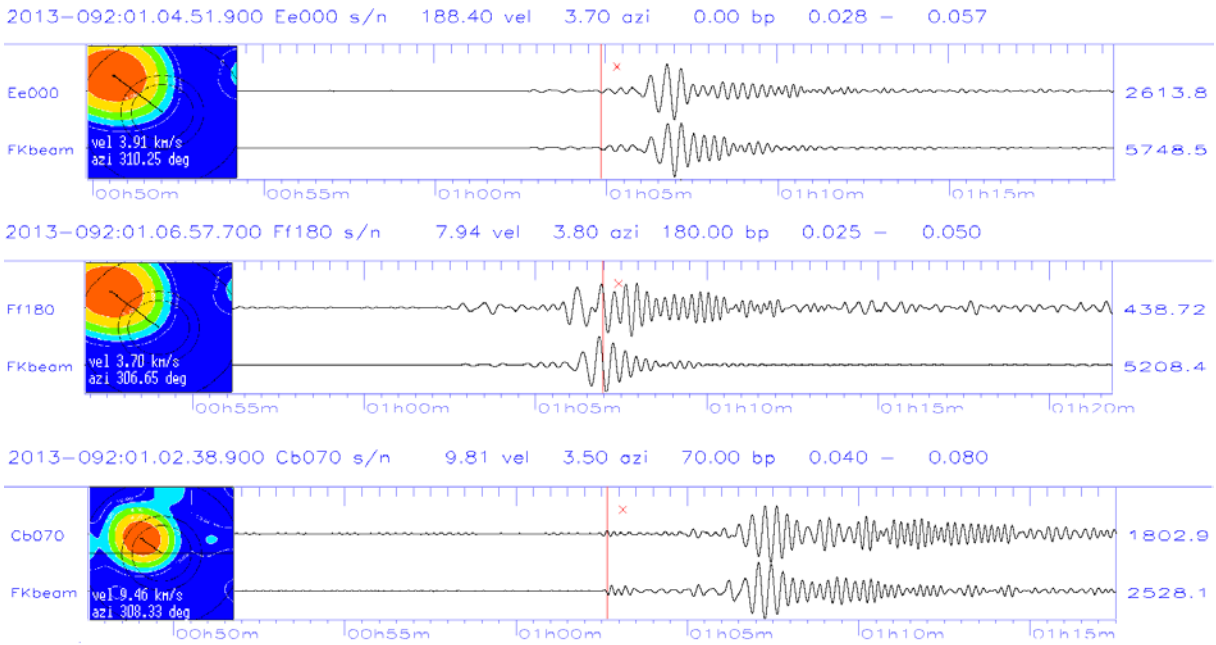

Fig. 6.2.7 Icelandic region event on 2 April 2013 00:59 recorded at NOA, showing three different detections within the wavetrain. The detection times are marked by red vertical lines. Each panel shows the detection beam (top) and the f-k beam (bottom). The parameters shown above each panel of beams refer to the detection-beam parameters. The f-k analysis results are plotted together with the corresponding apparent velocity and BAZ values. The detection beam BAZ ("azi" values on top of each panel) shows noticeable instability, whereas the back-azimuth values shown in the f-k plots are very consistent.

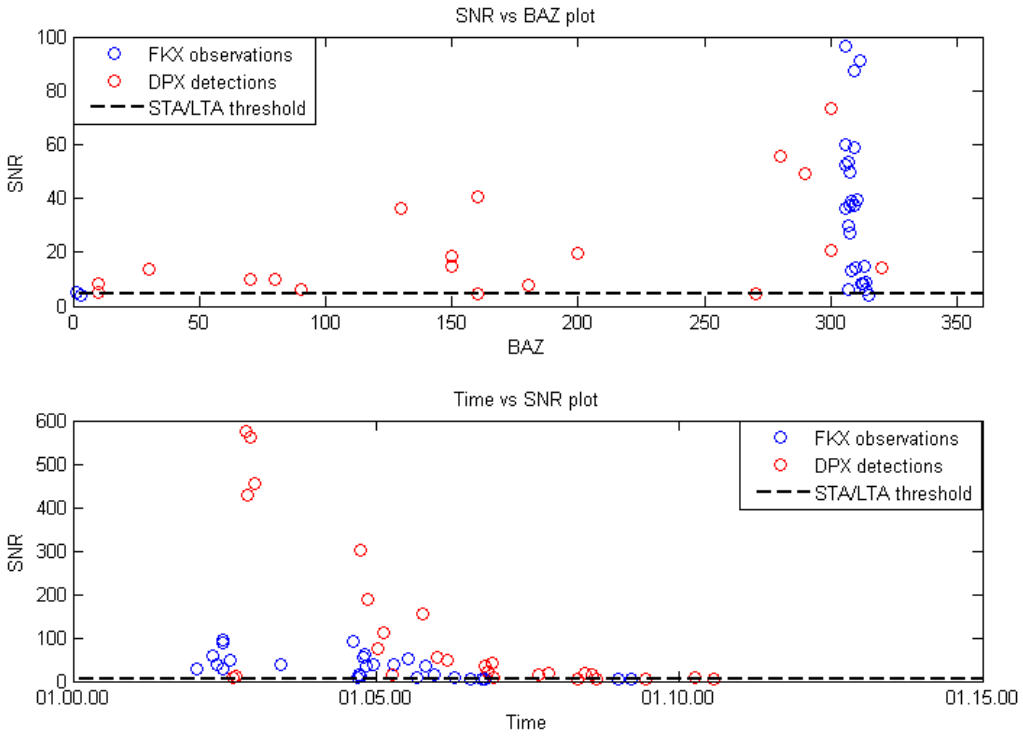

Fig. 6.2.8 Plot showing the differences between detection beam parameters (red) and signal parameters from f-k analysis (blue) for the 2 April 2013 00:59 Icelandic Region event (see also Figure 6.2.7). On top panel the SNR is plotted against the BAZ, while on bottom panel the SNR is plotting as function of time. The dotted line represents the SNR threshold level of 4.5. It is clear that the results of the f-k analysis improve the SNR and cluster at and azimuth close to the theoretical value of 305°.

6.2.3.4 Phase identification

The phase identification procedure is based on velocity estimates reported from the f-k analysis. As seismic arrays are capable of extracting velocity and period of the recorded waves, the phase naming criteria for Rayleigh waves are based on the signal's phase velocities and dominant period. All onsets with either an observed phase velocity between 3.1 and 4.5 km/s or an observed dominant period larger than 35 s are identified as LR (Rayleigh wave) by the algorithm.

By comparing the results of analyst reviewed phase recognition of the observations with the results of the automated processing for the time between 1 and 9 January 2013 it is possible to evaluate the quality of the automatic phase identification criteria (Figure 6.2.9). The automatic phase naming seems to separate reasonably well body- and surface wave detections, but fails in separating the LR observations from triggers by the secondary ocean microseisms because of their overlap in both the frequency and the velocity ranges (see Figure 6.2.9, bottom)

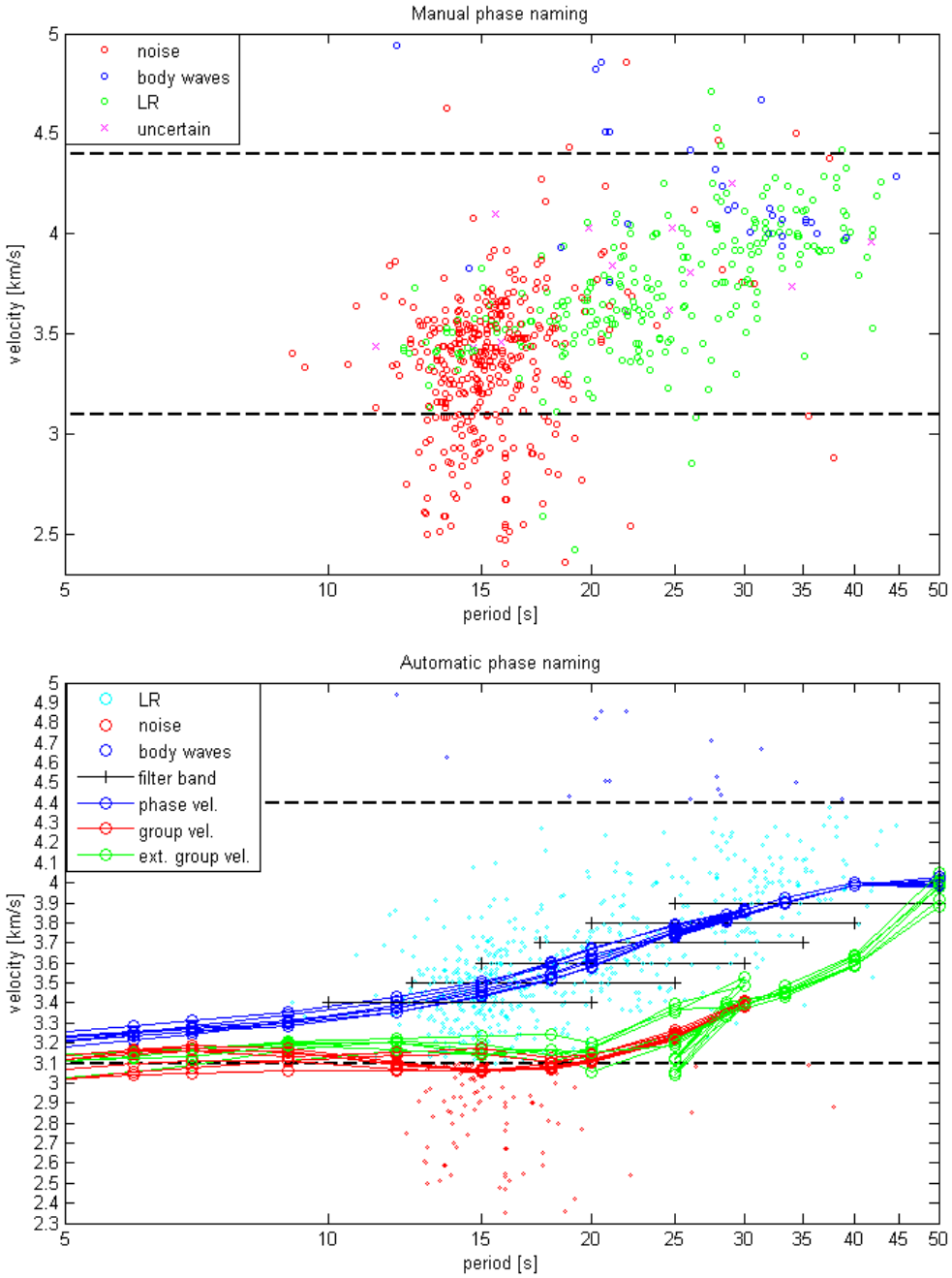

Fig. 6.2.9: The top panel shows the manual phase naming of the detections recorded between 1 and 9 January 2013. Noise detections are displayed in red, Rayleigh waves in green and body waves in blue. A cross marks unclear cases. It is possible to visually identify the critical areas in which the dispersive Rayleigh wave detections overlap with the noise observations and with the slowest propagating body waves.
At the bottom panel the automatic analysis results for the same time interval are shown. The dashed lines in both panels show the chosen velocity constraints to define LR waves. Cyan symbols within the velocity limits are assumed to represent LR arrivals, red are noise, and blue are body waves. The blue, red and green lines represent respectively the dispersion curves for phase-, group- and extended group velocities at the 7 NOA subarrays as reported by Köhler et al. (2012).

6.2.3.5 Recognizing the disperse character of surface waves

To improve the phase identification, further analysis on selected known events was performed. Of particular interest is the detector's ability to recognize surface-wave energy in the different frequency bands (see Figure 6.2.10).

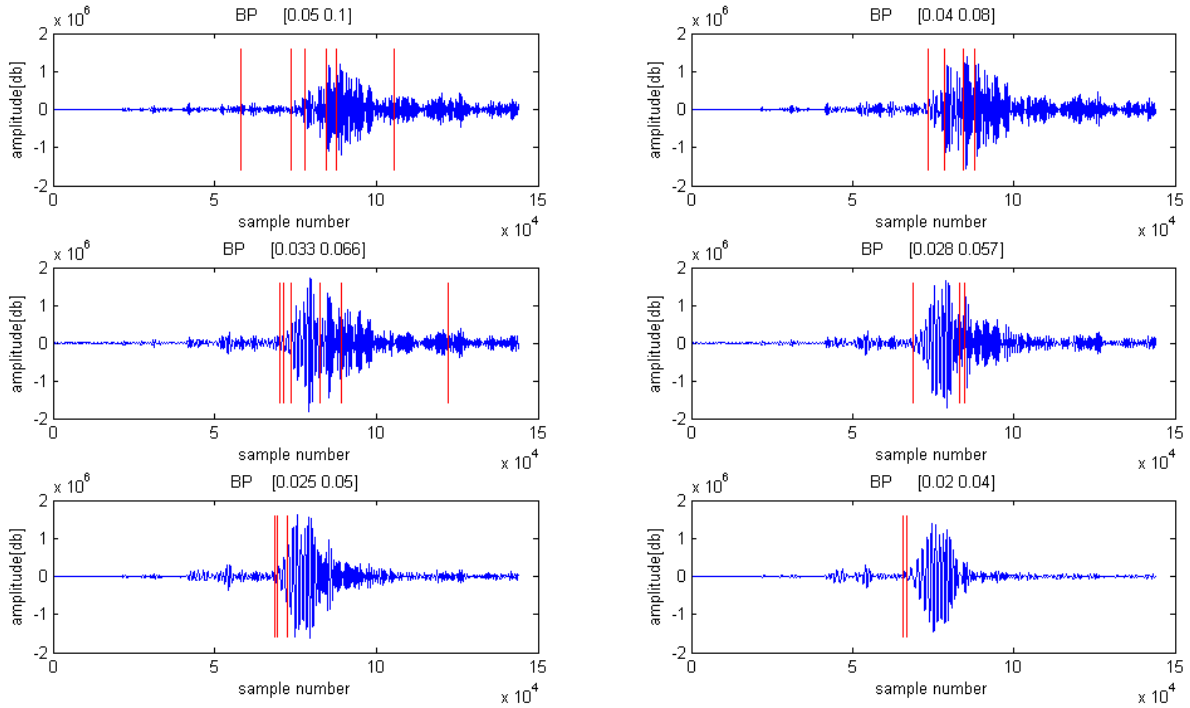

Fig. 6.2.10 Plots of automatic detections (red lines) in different frequency bands for the 05 January 2013 09:00 Alaska earthquake. Each seismogram shows the filtered data (not beams) as recorded at array site NAO01. The passband of the Butterworth filter is given on top of each panel (in Hz).

By plotting the detector results on top of Amplitude Spectral Density (ASD) plots for the 5 January 2013, 09:00 Ms 7.6 Alaska event, it is possible to evaluate the LR observations and how they show the dispersive behavior of the Rayleigh wavetrain both in time and frequency. Figure 6.2.11 shows such plots as a stack of all ASDs calculated for all 5 sites of the NB2 subarray of NOA. In addition are shown the onset time and frequency range of the corresponding DPX detections (upper panel), and the onset time and frequency range from the SAP processing. Note that the ASDs of the individual sensors were not phase delayed during the stacking as this would amplify only one specific phase velocity. It is clear that all major seismic onsets of the record were detected with the chosen set of detection beams.

For large events for which the detector create several triggers within the wavetrain, it is also possible to recognize and reconstruct the Rayleigh-wave dispersion curves by plotting the estimated signal period and corresponding velocity values as a function of time (see Figure 6.2.12).

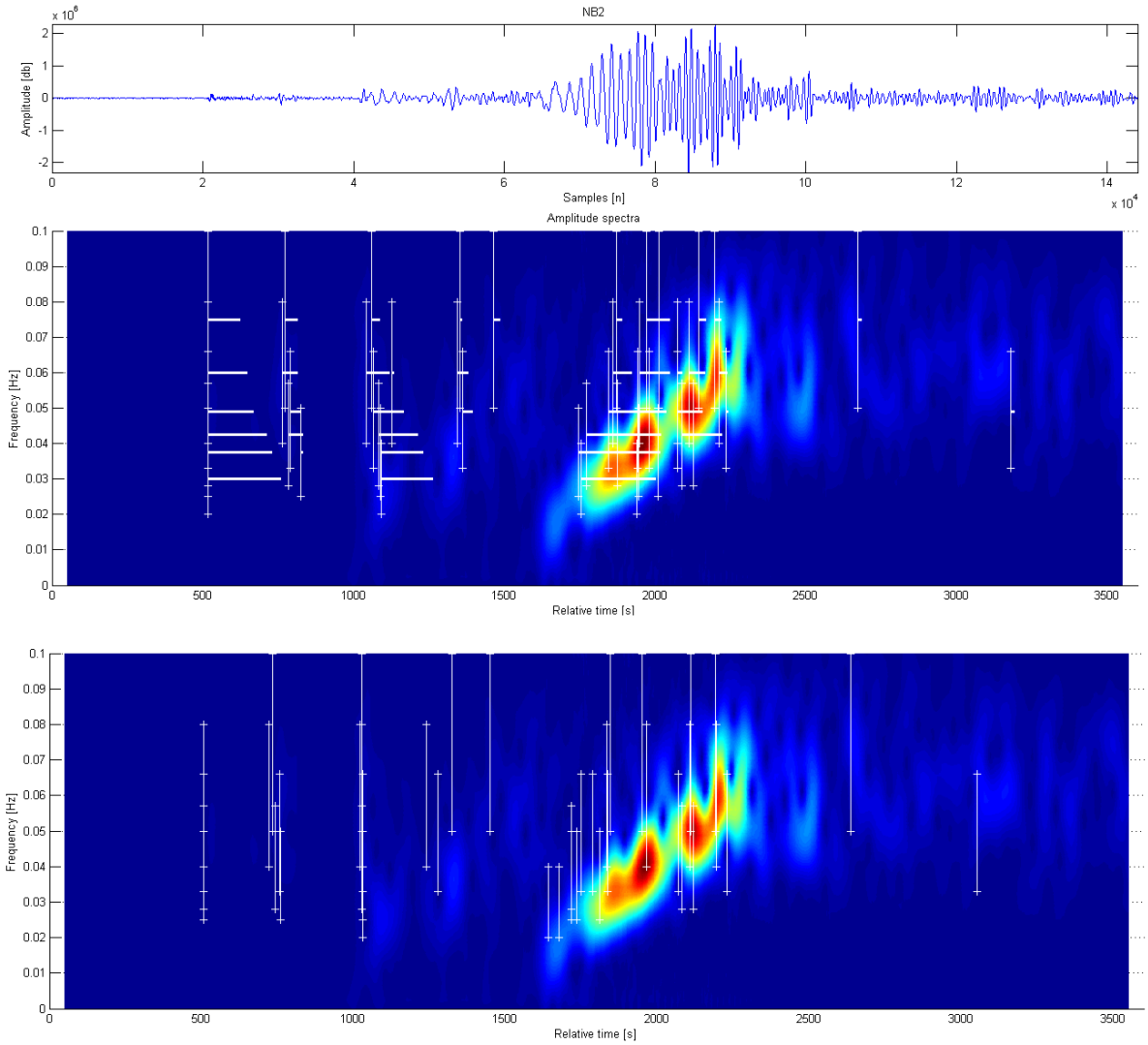

Fig. 6.2.11 TOP panel: stacked ASD for the 5 January 2013 09:00 Alaska event as recorded at subarray NB2. The vertical lines represent the DP detections as from the DP, with their length indicating the frequency range of the different triggers. The horizontal lines represent the time windows for which the detector is in triggering mode.
BOTTOM panel: ASD plot of the same event, with the vertical lines representing the onset time and frequency range of the phases as recognized by the SAP.

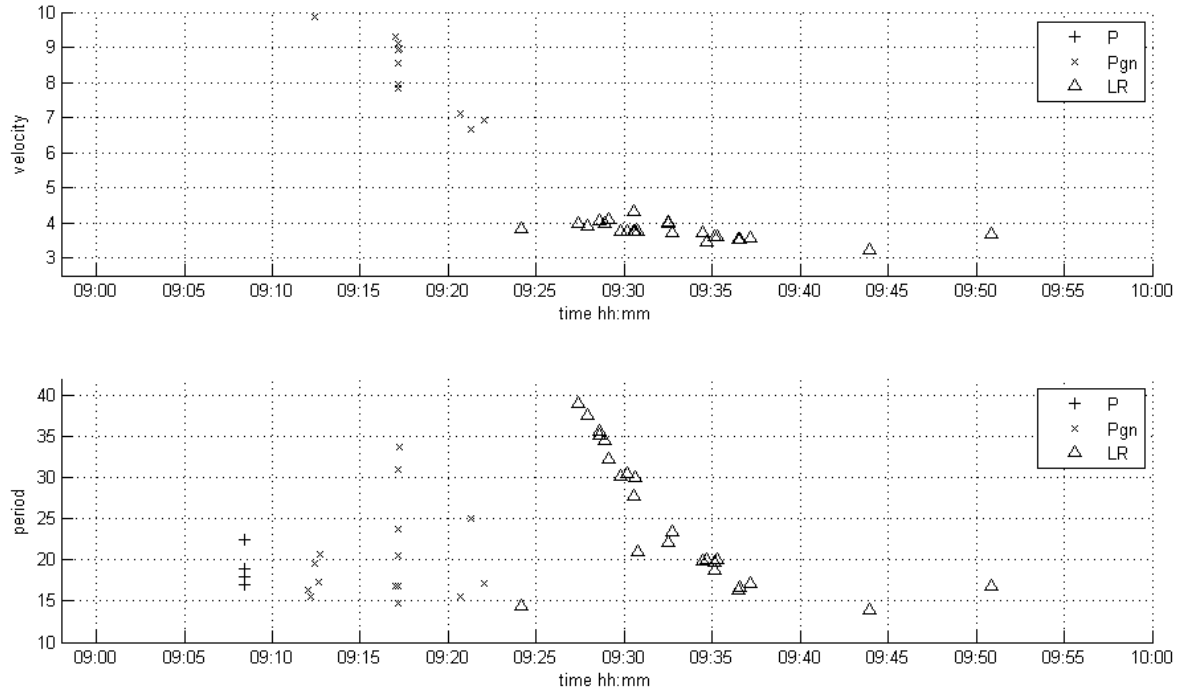

Fig. 6.2.12 The top panel shows the automatically estimated velocities from the f-k analysis plotted against time for the 5 January 2013 09:00 Alaska event. The lower panel shows the estimated dominant signal periods plotted as function of time. The theoretically expected decrease in signal period of the dispersive wavetrain can be clearly observed for the LR arrival, while P and other types of body-wave signals (Pgn/S) at 09:08 and 09:17 do not show any dispersive character. For LR a corresponding slight decrease in measured phase velocities is observed (upper panel).

6.2.4 Detector event coverage

In order to validate the results achieved by the detector on the recorded two-year dataset, a Matlab event association program for Rayleigh wave observations was written. By associating the observed Rayleigh waves to verified events we can estimate the capability (or "event coverage") of the new DPEP LP Detector to detect Rayleigh waves.

6.2.4.1 Associating Rayleigh wave observations to events in the IDC Reviewed Event Bulletin

As a reference we use reported Rayleigh waves (LR phases) in the IDC Reviewed Event Bulletin (REB). The results from the DPEP LP Detector (including f-k analysis) are compared to a selection of events from the REB which has a likelihood of producing "detectable" LR phases at NOA. Event selection criteria have been set up to select only events that could possibly produce surface waves, mainly avoiding very deep and small earthquakes and taking into account the higher detectability of closer events (40° from NOA) by including magnitude, depth and distance thresholds. Events are also included for which an LR phase detection is reported from any station of the International Monitoring System (IMS) or for which a body wave detection is reported from one of the North European arrays.

The event association program estimates for each listed event a possible Rayleigh-wave arrival time and a BAZ window, defining an "event box" to which each detection is compared. LR observations

with time and BAZ falling inside such an event box are considered as associated to that event (see Figure 6.2.13).

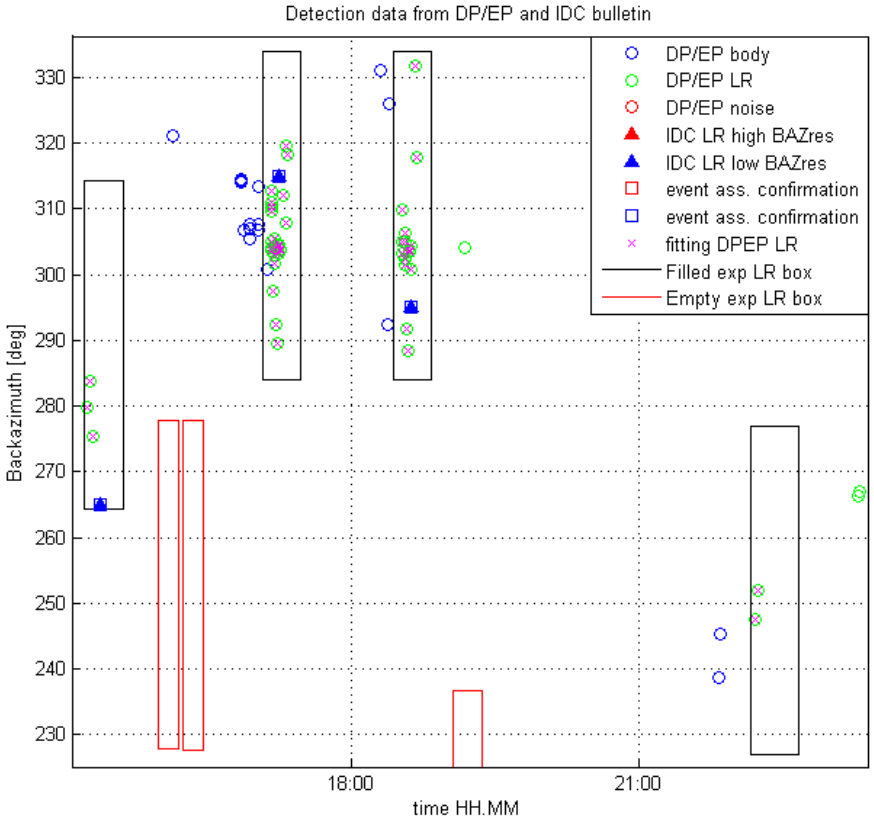

Fig. 6.2.13 Example of event boxes and the associated NOA surface wave detections both from the IDC (REBs) and the DPEP LP detector system.
Circles represent DPEP observations: blue - body waves, green – Rayleigh waves, and red - noise; associated LR detections are filled with a magenta cross.
Triangles are reported IDC (REBs) LR observations at NOA: red – LR with large BAZ residual, blue – LR with small BAZ residual. Event boxes are shown as rectangles: black if detected by the DPEP system, red if not.

A careful selection of minimum and maximum expected group velocities (2.8 and 4.1 km/s, respectively) for the definition of the expected arrival time window provided good automatic association results. The BAZ width of the event boxes is set to ±25° (see Figure 6.2.14).

The program also reassociates the LR observations detected by the IDC's own processing (see Stevens & McLaughlin (2001) when using NOA data (called IDC NOA LRs), allowing a comparison of the IDC long-period processing with the NORSAR DPEP LP Detector.

The IDC NOA LRs are included in the statistics only if the BAZ residual is smaller than 25°. This is because larger residuals mostly proved to be wrong associations. A large part of the wrongly associated LR phases have BAZ observations from the main noise directions between 225° and 345° (see Figure 6.2.14).

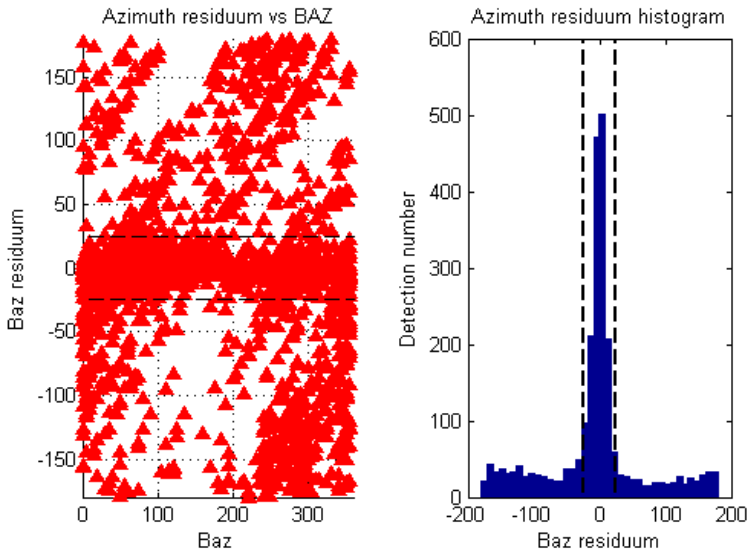

Fig. 6.2.14 BAZ residuals as reported in the REBs of the IDC. Left: BAZ vs. BAZ residual. Right: histogram of the same BAZ residuals. The dashed lines mark the ± 25° limits to define the event boxes in Figure 6.2.13.

6.2.4.2 Statistical analysis of event association results

This chapter presents the results of the statistical analysis over two years of available broadband data since the NOA recapitalization (31/08/2012 – 31/08/2014). From the event association results we have introduced several tests to evaluate the DPEP LP detector performance:

- Observe the amount of associated/non-associated LR detections and analyze their parameters to identify possible noise sources. As criteria were used all DPEP LR detections arriving within a time window defined by the group velocities between 2.8 and 4.1 km/s after the source time and which have a BAZ deviation of less than 25°.
- Observe the amount of events detected by the DPEP LP detector, the IDC detector, or both to compare their effectiveness using the same input data. Seismic events are defined as possibly detectable if they meet the conditions for event selection described in section 6.2.4.1.
- Analyze the capability of the new processing to detect events previously undetected by NOA as reported IDC REB.

The statistical analysis shows that using these criteria, 60% of the DPEP LR detections can potentially be associated with an event in the IDC REB, while the remaining 40% can be related to triggers due to ocean microseisms, to the detection of events excluded by the event selection process, or to seismic noise and instrumental noise.

Number of NOA LR detections from DPEP		
All DPEP detections	134950	100%
Associated to REB events	80189	60%
non-associated	54761	40%

Number of NOA LR detections from IDC		
All LR in REBs	4985	100%
With small BAZ residual	3043	61%
With large BAZ residual	1942	39%

"Detectable" REB events		
Total number of events	21760	100.0 %
Events without LR observation	15359	70.58 %
NOA events detected by IDC (with small BAZ residual) or DPEP	6401	29.4 %
NOA events detected by DPEP	5856	26.9 %
NOA events detected by IDC (with small BAZ residual)	3043	13.9 %
NOA events detected by DPEP only	3360	15.4 %
NOA events detected by IDC (with small BAZ residual) only	545	2.5 %
NOA events detected by both	2496	11.5 %
NOA events detected by IDC with large BAZ residual	1958	9.0 %

It is clear that the new processing scheme could provide a noticeable improvement in terms of event detection capabilities (see Figure 6.2.15). The proposed detector finds potential LR surface waves for 26.9% of the selected events from the IDC REB, while the IDC reports only for 13.9% of the events LR observations. Of the total number of events, 15.4% have potential DPEP LR detections and no IDC LR detection, while the amount of "missed" events, for which Rayleigh waves are detected by the IDC but not by the DPEP system, is only 2.5%. This percentage can be largely accounted by very dense seismic sequences otherwise correctly detected or in some cases the IDC association might be based on ocean microseism detections having by chance the correct BAZ. That this is a larger problem can be seen in Figure 6.2.16. Here observed BAZ values are plotted with respect to time. A band of non-associated LR detections is clearly visible when a low pressure system is located in the North-Atlantic.

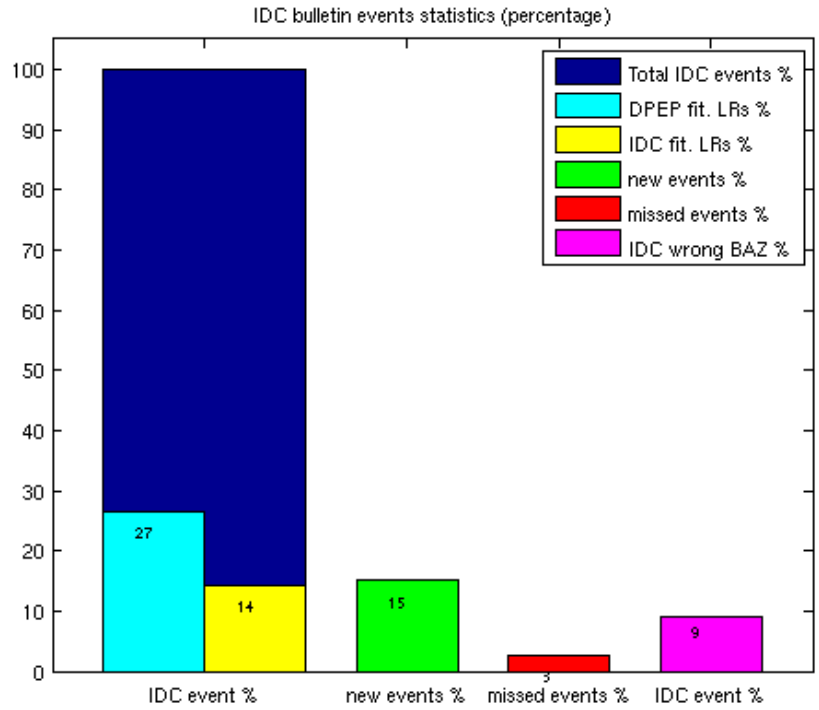

Fig. 6.2.15 IDC bulletin statistics for 2013. All the data are shown as % of the total selected events from the IDC REB.

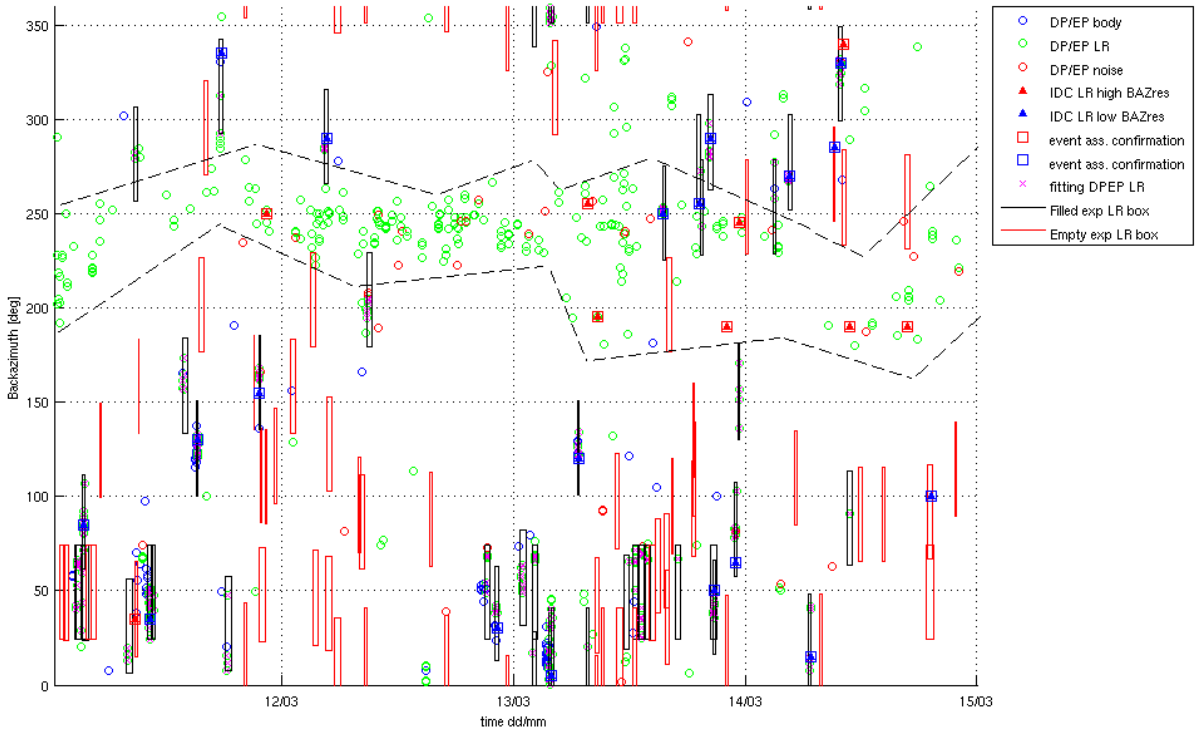

Fig. 6.2.16 Observed microseisms during a time window (11-15 March 2013) showing no major earthquakes. The clustering of unassociated DPEP LR (green circles) and IDC LR (red triangles within a square) observations in the contoured noise azimuthal area can be clearly seen.

The analysis of the surface-wave magnitudes Ms and Ms1 of the detected and undetected events also demonstrates that the new detector is able to observe LR phases for all major earthquakes (see Figure 6.2.17 and 6.2.18). The mean (median) of all surface magnitudes Ms and Ms1 is 3.8 (3.8) for the DPEP detected and 2.4 (3.1) for the DPEP undetected events.

The analysis of LRs detection parameters shows the noisy nature of most of the non-associated detections. The velocities, periods and BAZ are all displaying values that are typical for ocean microseisms, which have in the mean lower SNR, smaller periods, lower propagation velocities and less reliable f-k analysis results.

DPEP LRs extracted parameters for the year 2013						
Associated	Mean	Median		**Non-Associated**	Mean	Median
BAZ	117.04	69.90		BAZ	194.83	231.40
Velocity	3.73	3.70		Velocity	3.59	3.56
Rel. Power (F-K)	0.84	0.88		Rel. Power (F-K)	0.64	0.65
Dominant period	23.14	21.15		Dominant Period	18.41	17.15
SNR	7.6	6.1		SNR	5.3	4.9

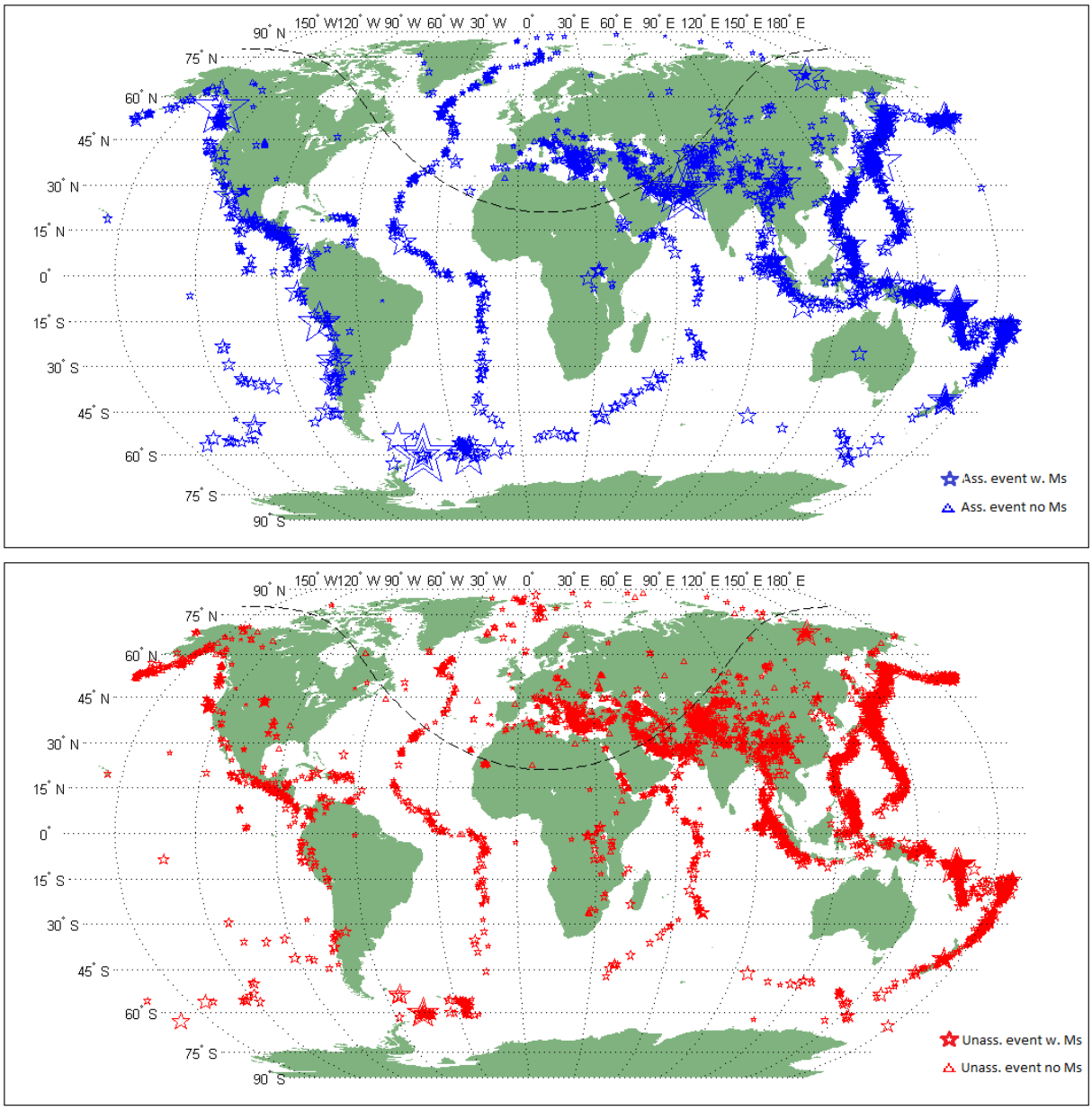

Fig. 6.2.17 World maps of the events listed selected as "detectable" in the association processing for the year 2013. Top plot displays the events with potential Rayleigh waves detected by the NOA DPEP LP detector, while bottom plots the undetected ones. In both plots events with an assigned Ms value are marked by a star, with its size being proportional to the event magnitude. Events with no Ms value in the REBs are displayed as triangles. The black dashed line defines a radius of 40° around NOA.

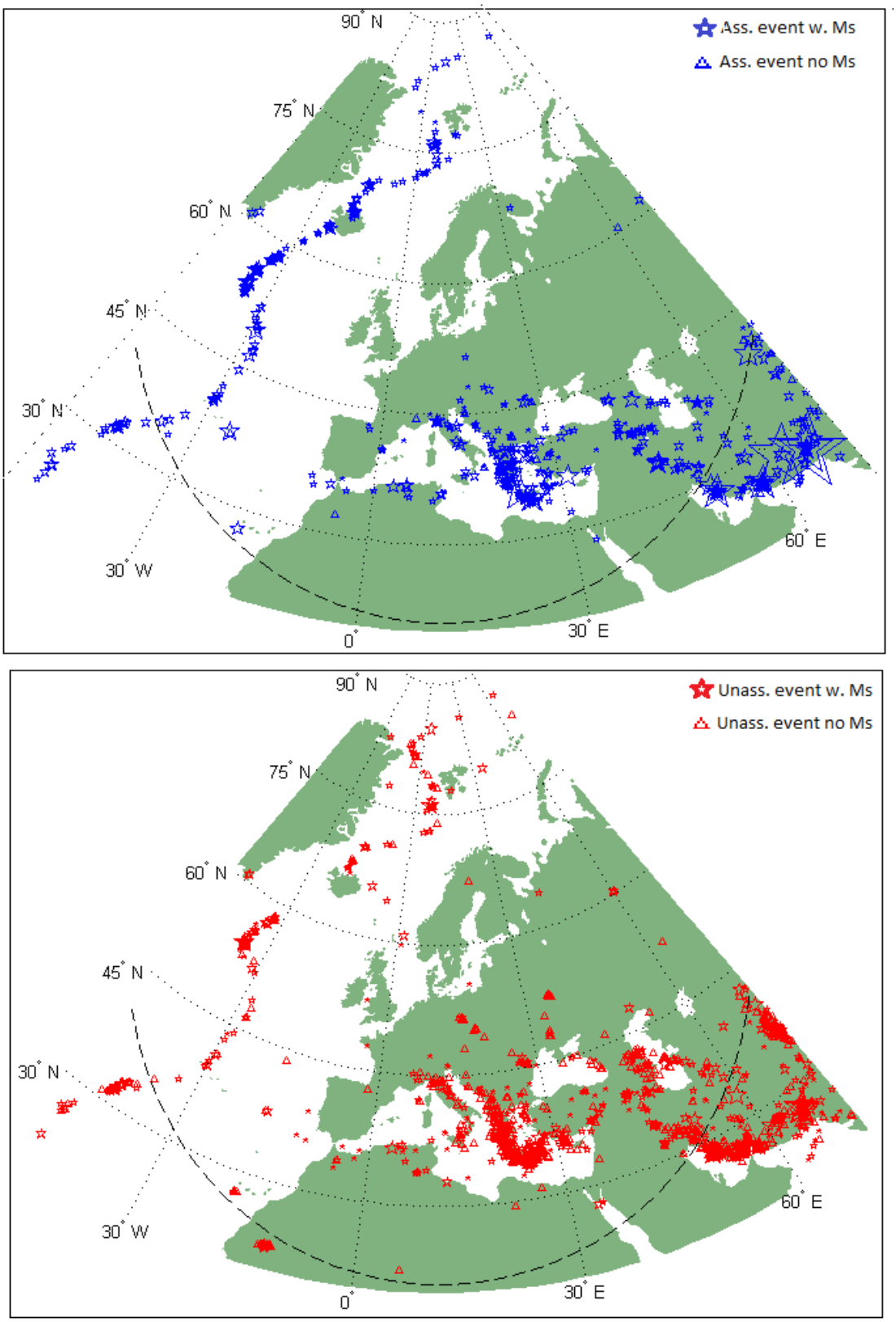

Fig. 6.2.18 European maps displaying the same data of Figure 6.2.17. The black dashed line defines a radius of 40° around NOA.

6.2.5 Conclusions

The NOA DPEP long-period detector achieved promising results in Rayleigh-wave signal detection and recognition. It detects potential surface-wave arrivals down to very low SNR, evaluates their BAZ, velocity, period and amplitude with very high resolution, and in many cases correctly separates body waves from LR detections.

Because of the Rayleigh-type nature of ocean microseisms, it has proven difficult to consistently separate microseism detections from surface waves produced by earthquakes or explosions. The development of a further processing step involving dispersion testing or pattern recognition in near-real time could remedy this shortcoming and potentially yield a powerful tool for surface waves analysis in the CTBT context. Furthermore, such a development could provide very useful information for seismic noise studies, e.g., ambient noise seismic tomography.

Acknowledgements

Most of the presented work was done during research visits of N.L.C. at NORSAR financed by the EC ERASMUS program and the EC research project NERA (#262330). The results were also used as part of the Master thesis of N.L.C. at the University of Trieste.

N. L. Celli, University of Trieste
J. Schweitzer
J. Fyen

References

Bungum, H., S. Mykkeltveit and T. Kværna, 1985, Seismic noise in Fennoscandia, with emphasis on high frequencies, *Bull. Seism. Soc. Amer*., 75, (6), 1489-1513.

Fyen, J. (1987): Improvements and modifications. Semiann. Tech. Summary., 1 Oct 1986 - 31 Mar 1987, *NORSAR Sci. Rep. No. 2-86/87*, Kjeller, Norway. (DP)

Fyen, J. (1989): Event processing program package. Semiannual Tech. Summary, 1 Oct 1988 - 31 March 1989, *NORSAR Sci. Rep. No. 2-88/89*, Kjeller, Norway. (DPEP)

Köhler, A., C. Weidle and V. Maupin, 2011, Directionality analysis and Rayleigh wave tomography of ambient seismic noise in southern Norway, *Geophys. J. Int*., 184, (1), 287–300.

Köhler, A., C. Weidle and V. Maupin, 2012, Crustal and uppermost mantle structure of southern Norway: results from surface wave analysis of ambient seismic noise and earthquake data, *Geophys. J. Int*., 191, 1441–1456.

Kværna T., and D. J. Doornbos, 1986, An integrated approach to slowness analysis with arrays and three-component stations, *NORSAR Sci. Rep*., 2-85/86, 60-69.

Haubrich, A., W. H. Munk and F. E. Snodgrass, 1963, Comparative Spectra of Microseisms and Swell, *Bull. Seism. Soc. Amer*., 53, (1), 27-37.

Longuet-Higgins, M.S., 1950, A Theory of the Origin of Microseisms, *Phil. Trans. R. Soc. London*, Series A, Mathematical and Physical Sciences, 243, (857), 1-35.

Mykkeltveit, S. and H. Bungum, 1984, Processing of regional seismic events using data from small aperture arrays, *Bull. Seism. Soc. Amer*., 74, (6), 2313-2333.

Schweitzer, J., J. Fyen, S. Mykkeltveit, S. Gibbons, M. Pirli, D. Kühn and T. Kværna, 2011, Seismic Arrays, in: IASPEI New Manual of Seismic Observatory Practice, Chapter 9, 80 pp.

Stevens J. and K. McLaughlin, 2001, Optimization of Surface Wave identification and Measurement, *Pure Appl. Geophys*., 158, 1547-1582.

Trnkoczy, A., 1999, Understanding and parameter setting of STA/LTA trigger algorithm, in: IASPEI New Manual of Seismic Observatory Practice, Information Sheet 8.1, 19 pp.

6.3 Stratospheric and Thermospheric Infrasound Signals Recorded at IS37

6.3.1 Introduction

The IMS infrasound array IS37 near Bardufoss in northern Norway, started providing data in October 2013. In August and September 2014, IS37 recorded for the first time infrasound signals from each of 15 ammunition destruction explosions at Hukkakero, a military site in Northern Finland at a distance of approximately 320 km.

The first 12 of the explosions were large blasts with yields of approximately 20 tons and, for each of these events, an extensive wavetrain is recorded. Approximately 18 minutes after the explosion, a long duration signal rich in high frequencies, is observed. Between 3 and 4 minutes later, signals of far shorter duration and lower frequency are observed with higher trace velocities, indicating refraction from greater altitudes.

Modelling supports the hypothesis that these distinct parts of the wavetrain are stratospheric and mesospheric/thermospheric phases respectively. We observe that the trace velocity for almost all of the stratospheric part of the wavetrain is essentially constant, whereas the thermospheric phases are associated with quite differing trace velocities: indicative of turning points at different altitudes.

The final three explosions at Hukkakero in 2014 were of far lower yield and only generated signal detections at IS37 in the stratospheric part of the wavetrain.

In this study we attempt to interpret features of the observed wavetrains, like the trace velocities and celerities, through modelling in perturbed atmospheric models. One goal for this study is to be able to create so-called celerity expectation lookup tables applicable for use in event location algorithms.

6.3.2 Hukkakero ground truth explosions in 2014

Between August 22 and September 3 in 2014, the Finnish military set off 15 explosions to demolish ammunition at the Hukkakero site in Northern Finland. All explosions occur within approximately 150 meters of the coordinates 67.934^{o}N 25.832^{o}E. The location of the explosion site in relation to the ARCI and IS37 infrasound arrays is displayed in Figure 6.3.1. Acoustic signals generated by Hukkakero blasts in previous years, recorded at other stations, have been considered by e.g. Gibbons et al. (2007, 2015), Israelsson (2013), and Liszka and Kværna (2008). Figure 6.3.2 shows observations at the IS37 central sensor of the 15 Hukkakero explosions in 2014. The leftmost part of each trace has been overlaid with the seismic recording at ARCES, colored red, which was used for detection and timing of the events and for associating the signals unambiguously with the source location. The apparent velocities of the infrasound signals arriving at IS37 are represented by the color background. It is clear that there are two distinct parts of the infrasonic wavetrain for these events. A long duration signal from around 18 to 20 minutes after the explosion time is rich in high frequency energy and arrives with an almost constant apparent velocity of the order of 340 m/s. Between 20 and 23 minutes after the explosion times, shorter duration signals are observed with lower frequency content. These arrive with higher apparent velocities and there is a significantly greater variability in the trace velocity, indicating ray turning points at different altitudes. The signal characteristics of the earlier and later parts of the wavetrain are consistent with those associated with stratospheric and

thermospheric returns respectively (Mutschlecner and Whitaker, 1999; Whitaker and Mutschlecner, 2008).

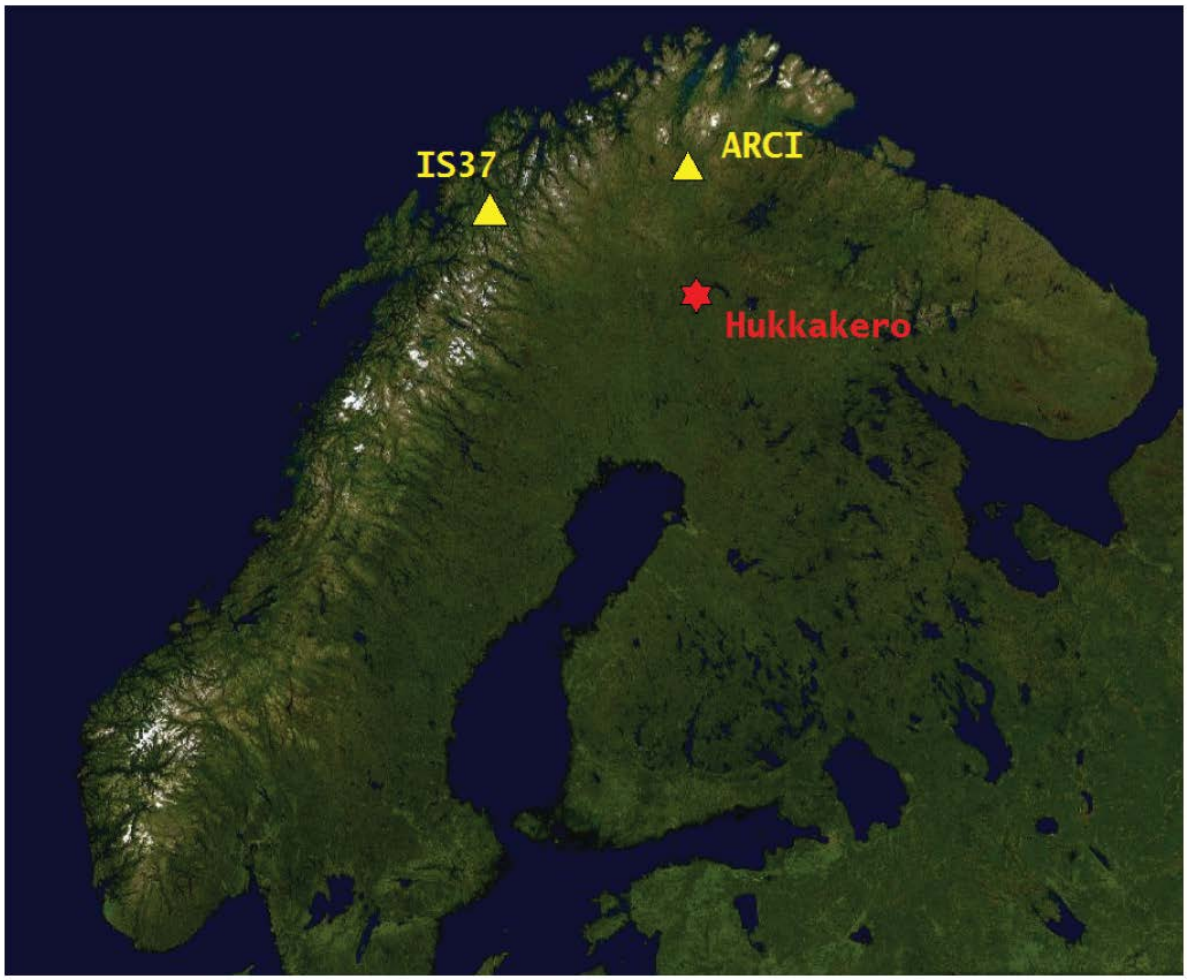

Fig. 6.3.1 Map showing the location of the explosion site at Hukkakero (67.934°N, 25.832°E) in relation to the infrasound arrays ARCI (69.538°N, 25.5078°E) and IS37 (69.0741°N, 18.6076°E).

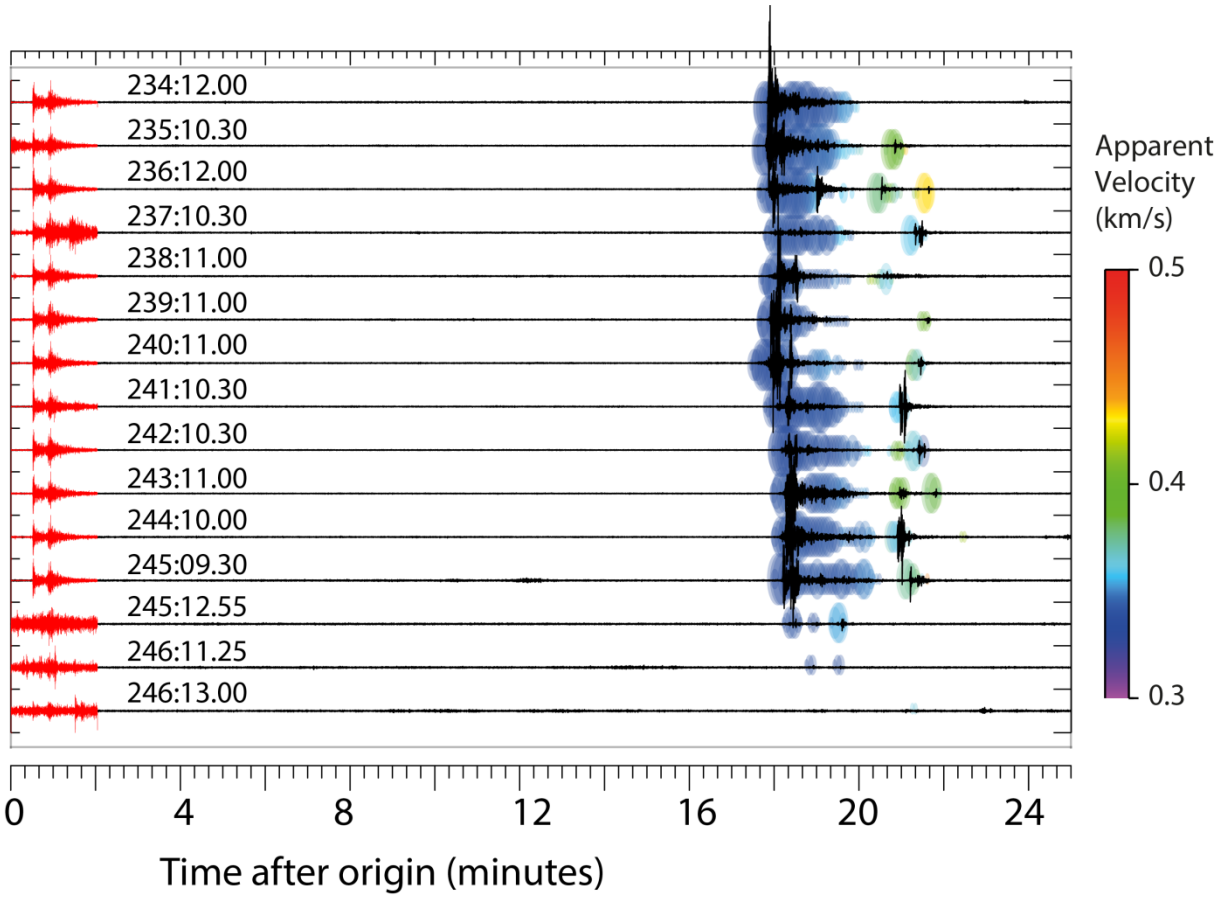

Fig. 6.3.2 Microbarograph data (1-4 Hz) at the IS37 central site (black) and seismic data (4-16 Hz) at the ARCES central site (red) for 15 Hukkakero events in 2014. The symbols behind the waveforms indicate the apparent velocity measured at IS37 and are sized proportional to the cross-correlation stack peak, provided consistency with a relevant infrasound signal. The cross-correlation values range between over 0.9 for the strongest signals to around 0.1 for signals right at the noise level. The first 12 events have a presumed explosive yield of approximately 20T, the final 3 are far smaller. The origin time is given to the nearest minute in the format ddd:hh.mm where ddd, hh, and mm are the day of year, the hour, and minute respectively. All waveforms are aligned using the seismic signals.

Figure 6.3.3 provides a closer look at the infrasonic signals recorded in the time-window 17 to 23 minutes following the blasts. The traces are filtered in a much broader frequency band (0.03 – 1.50 Hz) and show more clearly the differing frequency content of the two parts of the wavetrain. Instead of the trace from a single sensor, as is displayed in Figure 6.3.2, we show a beam of all 10 traces from the array steered with a backazimuth of 110 degrees and with an apparent velocity of 0.4 km/s. The beamforming provides a significant improvement in the signal-to-noise ratio (SNR) even though the constant apparent velocity chosen will not provide optimal waveform alignment for all parts of the wavetrain. The N- and U-shapes observed in the second part of the wavetrain typically result from nonlinear propagation and caustic effects (see, for example, Gainville et al., 2009).

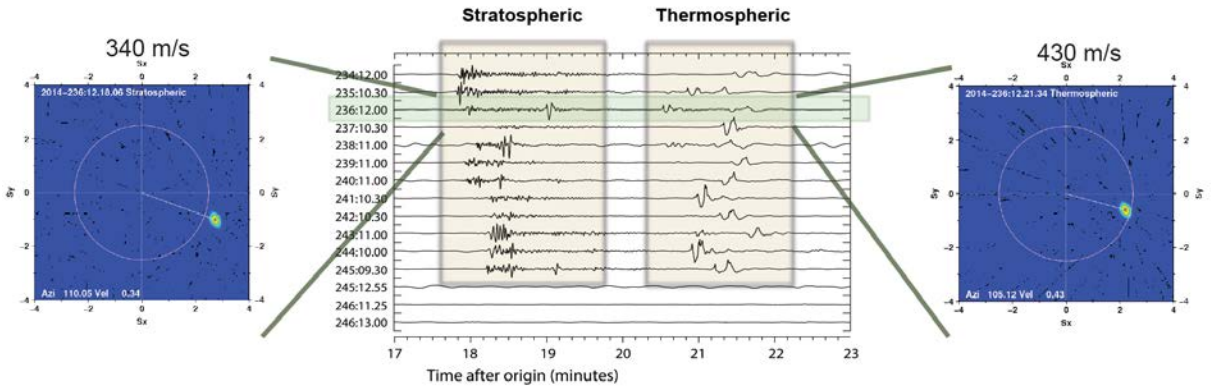

Fig. 6.3.3 Close in view of the infrasonic wavetrain at IS37 with a beam displayed for each of the events displayed in Figure 6.3.2. The beam is steered with an apparent velocity of 400 m/s and a backazimuth of 110 degrees and the waveforms displayed are filtered in the frequency band 0.03 Hz to 1.5 Hz. The slowness estimates are calculated using the channel to channel correlation procedure of Brown et al. (2002) in the 1-4 Hz frequency band.

6.3.3 Construction of atmospheric models for ray-tracing

We wish to use ray-tracing to model the infrasound propagation from the explosion site to the IS37 array. For this, we need both a ray-tracing algorithm and atmospheric specifications at the times of the events. The ray-tracing software used is ART2D (Walker, 2012), as used in Hedlin and Walker (2013). Using a philosophy akin to the one underlying the Ground-to-Space (G2S) model (Drob et al. 2003, 2010), we construct a compound model of the atmospheric wind and temperature using openly available sources for three ranges of altitude:

- For altitudes above 60 km, the most recent version of the Naval Research Laboratory (NRL) empirical Horizontal Wind Model (HWM; Drob et al., 2015) is applied while the temperature is extracted from the NRLMSISE-00 climatology (Picone et al., 2002).
- For altitudes between 25 and 70 km, we use the NASA Modern-Era Retrospective Analysis (MERRA; Rienecker et al., 2011) both for winds and temperature.
- For the lowest altitudes, up to 35 km, we apply the NCEP / NCAR reanalysis (Kalnay et al., 1996).

In the overlap altitude regions we apply a Hann-weighted average. For temporal and spatial coordinates where the underlying models are not available, we use multi-dimensional linear interpolation between the nearest grid points.

6.3.4 Introducing atmospheric wind perturbations due to gravity waves

It has long since been accepted that ray-tracing procedures through standard atmospheric models are unable to predict many infrasound arrivals which are repeatedly observed in the data. Such so-called shadow zone arrivals are usually interpreted as being caused by fine-scale inhomogeneities, in particular related to the presence of gravity waves (e.g. Gibson et al., 2008). Physics-based models have been sought to model the expected effect of gravity waves on infrasound propagation, and the

spectral model of Gardner et al. (1993) and Gardner (1994) was employed by Gibson et al. (2008) to generate many realizations of an atmosphere perturbed under the influence of gravity waves. Following the approach of Gibson et al. (2008), we generate wave spectra (Gardner et al., 1993; Gardner, 1994) at 4 different altitudes (see Figure 6.3.4).

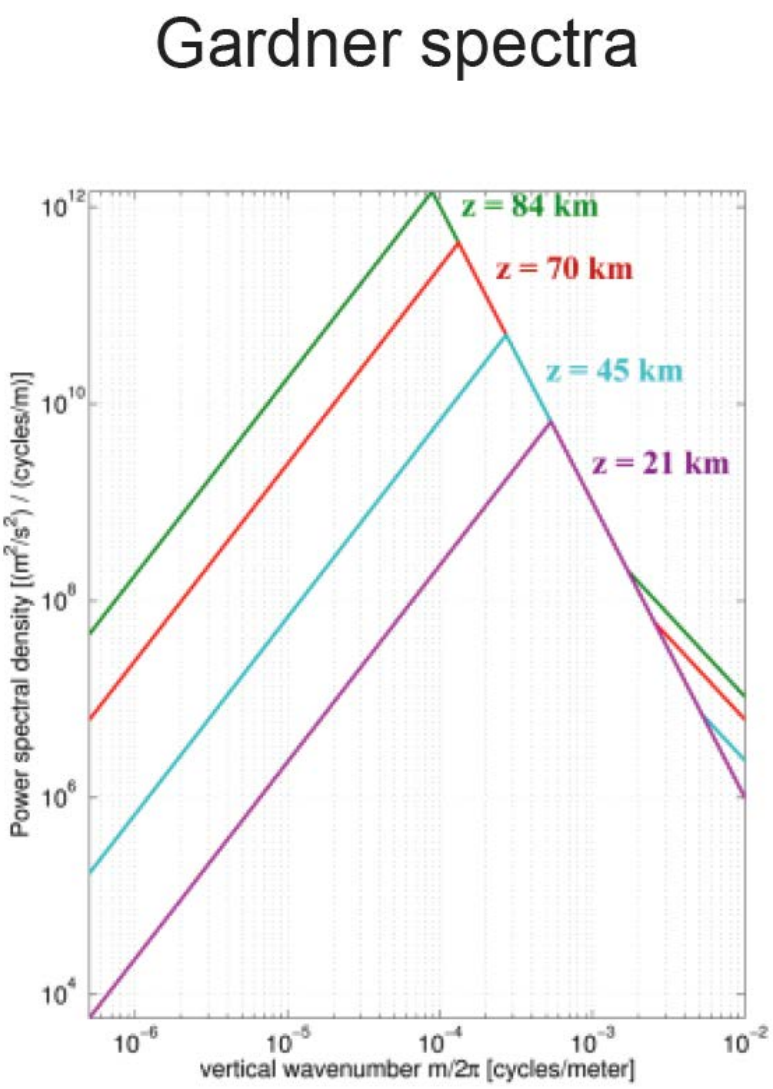

Fig. 6.3.4 Wind perturbation spectra from Gardner's gravity wave model for four different altitudes.

Each spectrum is then multiplied by a random phase factor and inverse Fourier transformed. By using different random phase factors we get different gravity wave realizations. Finally, compound gravity-wave profiles (dependent only upon altitude) are formed by weighted averaging over realizations corresponding to the 4 underlying altitudes. By varying the Gardner spectrum power, we hence vary the amplitude of the wind perturbations (Figure 6.3.5).

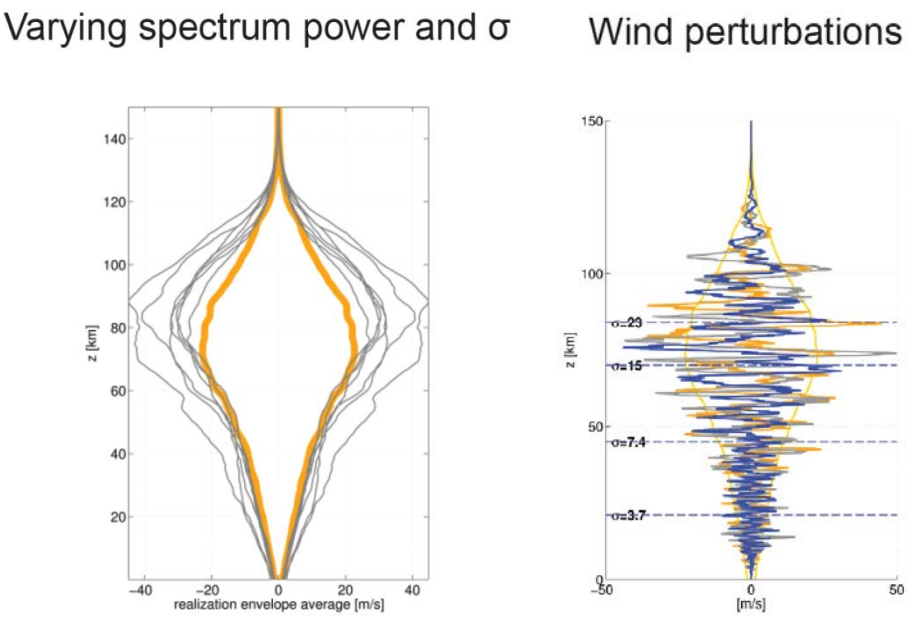

Fig. 6.3.5 Generation of wind perturbations from Gardner spectra. Left: varying spectrum power. Right: different compound realizations of gravity-wave induced disturbances to the wind profile.

6.3.5 Modelling of infrasound propagation in unperturbed models

We see from the data that the occurrence of infrasound arrivals varies from explosion to explosion. The atmospheric model will also change from day to day and we wish to assess the correspondence between the infrasound observed and that predicted to arrive by ray-tracing through a given model. Instead of traveltimes, we consider the celerity: the distance over the ground divided by the time taken. The first-arriving stratospheric signals have a higher celerity than the later arriving thermospheric phases. Figure 6.3.6 displays rays traced through the model with no perturbation for the August 24 explosion. It is clear that only high-altitude (thermospheric) rays reach the array in the unperturbed model.

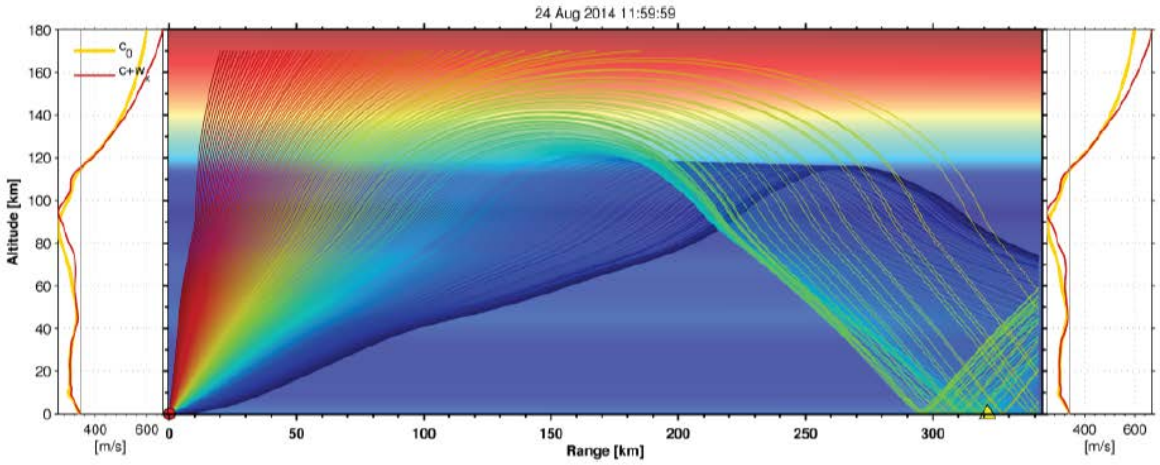

Fig. 6.3.6 Ray-paths obtained using ART2D through the unperturbed atmospheric profile for the August 24 Hukkakero explosion. The yellow triangle at 320 km is the IS37 array.

For each of the 12 largest Hukkakero explosions, we

- calculate celerities of observed coherent high-frequency (HF, 1-6 Hz) and low-frequency (LF, below 1 Hz) energy originating from the explosions.
- calculate celerities of signals modelled using ray-tracing through the atmospheric model at the time of the event.
- calculate the probability that infrasound energy with a given celerity is observed and/or modelled. (This is to say that, for a given celerity, we provide the proportion of the 12 occasions for which an infrasound signal was observed and/or predicted using ray-tracing through the atmospheric model for that time.)

Figure 6.3.7 confirms that, for the unperturbed models at the times of each of the 12 explosions, the only arrivals predicted to reach the array are thermospheric phases. Most of the thermospheric phase predictions are supported by observations although, for a number of events, only low frequency energy is observed. Both low and high frequency energy is observed for celerities between 280 and 300 m/s but none of these observed arrivals are confirmed by ray predictions through the unperturbed atmospheric models.

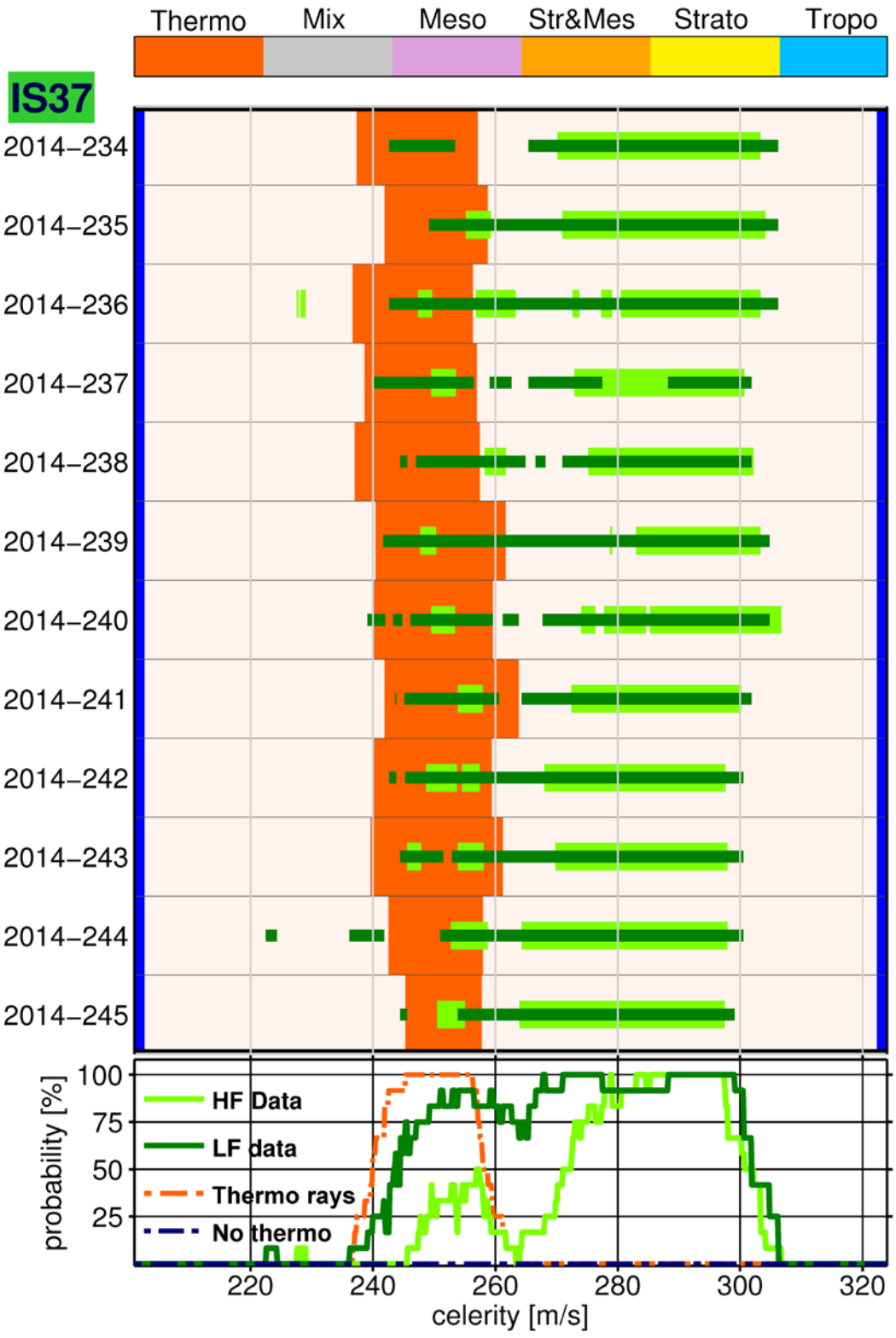

Fig. 6.3.7 Observed infrasound arrivals at IS37 as a function of celerity for the 12 largest Hukkakero blasts in 2014, together with modelled arrivals through an unperturbed atmospheric model. The light and dark green bars indicate respectively high frequency and low frequency infrasound energy actually recorded on the array for each explosion. The remaining colors indicate arrivals at the array that have been predicted by rays along the path indicated by the color. The lowermost panel indicates a probability distribution to indicate how frequently infrasound energy with a given celerity is observed/modelled.

6.3.6 Modelling in perturbed models

We introduced various wind perturbations to the atmospheric models by scaling of the perturbations introduced by Gibson et al. (2008). A large number of realizations were modelled by scaling the Gibson perturbations in the range 0.8 to 2.0.The best fit to the data were found using a scaling factor of 0.8, and the results are illustrated in 3 different realizations shown in the figure below, using the same type of display as above for the unperturbed model.

We see that for all of the events there is a good correspondence between the observed and predicted arrivals.

The lower part of the each panel shows a probability distribution of the observed and modelled celerities. The relatively good correspondence indicates that modelled probability distributions can be used to construct celerity expectation lookup tables which again can be useful in e.g. event location algorithms.

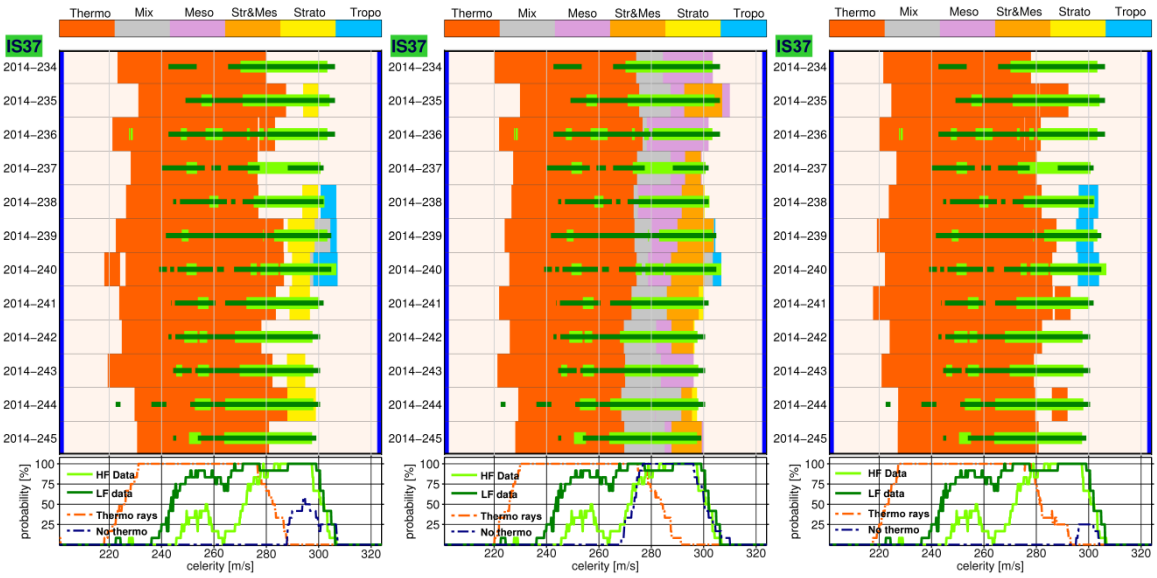

Fig. 6.3.8 Modelling results for 3 realizations of wind perturbations using a scale factor of 0.8 × Gibson.

Figure 6.3.9 further illustrates the great variation in modelled arrivals which can result when adding different perturbation realizations to the atmospheric models with 3 different amplitude scale factors. As expected we see a tendency that increased perturbation amplitude increases the occurrence of modelled returns.

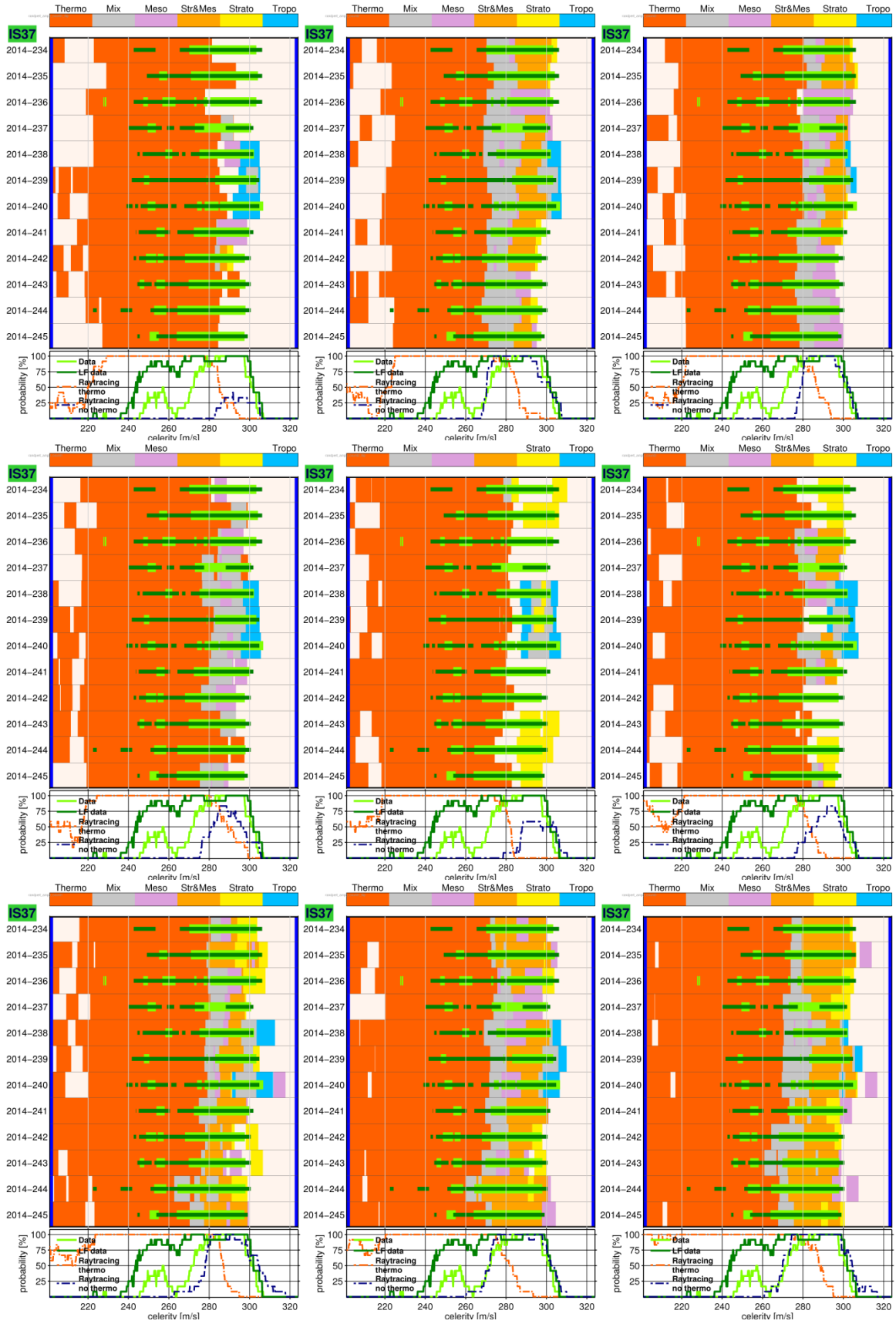

Fig. 6.3.9 Modelling results for 6 realizations of wind perturbations using a scale factor of 1 × Gibson (top row), 1.25 × Gibson (middle row), and 1.6 × Gibson (middle row)

6.3.7 Summary

We consider explosions at Hukkakero in Central Lapland, Northern Finland, from which infrasound was observed at the IS37 infrasound array near Bardufoss in northern Norway. We examine the celerities for which low and high frequency infrasound arrivals are observed and we examine the ability of ray-tracing to predict these arrivals, both in unperturbed atmospheric models and in models where perturbations are added to simulate the effect of gravity waves. Both in the modelling and in the observations, we consider arriving signals not only for the first arrival of each phase, but instead along the full wavetrain. This way we study the full impulse response of the events.

The thermospheric arrivals are predicted using the ray-tracer without the addition of any perturbations to the atmospheric model. However, the perturbations are necessary to be able to predict rays with turning points at stratospheric altitudes. The thermospheric phases are typically of lower frequency and they are not observed at all for the smallest of these events.

Regarding the necessity to include gravity-wave perturbations in the models, we also point out that recent research indicates that small-scale fluctuations are not always necessary to improve the match between predictions and observations (Smets et al. 2015). Smets and co-authors show that applying probabilistic propagation modelling using ensembles of perturbed ECMWF analysis atmospheric models can considerably improve the match.

Moreover, we need to emphasize the ray-tracing method's shortcomings due to its inherent high-frequency assumption, which for example can result in overestimating the width of shadow zones.

By varying the energy of the Gibson spectra and then shooting rays through a large set of corresponding perturbation realizations and finally analyzing the resulting modelled returns with recorded data, we envision the possibility of estimating the strength of the gravity wave activity.

Celerity expectation lookup tables calculated from probability distributions of the gravity-wave perturbed models can be helpful for interpretation of infrasound signals and for improving event location.

S. P. Näsholm
S. J. Gibbons
T. Kværna

References

Brown, D. J., C. N. Katz, R. Le Bras, M. P. Flanagan, J. Wang, and A. K. Gault (2002). Infrasonic Signal Detection and Source Location at the Prototype International Data Centre, *Pure and Applied Geophysics*, 159, 1081-1125, doi:10.1007/s00024-002-8674-2

Drob, D.P.; Picone, J.M.; Garces, M. (2003). Global morphology of infrasound propagation. *J. Geophys. Res*. 108(12), 4680, doi:10.1029/2002jd003307

Drob, D.P.; Garcés, M.; Hedlin, M.A.H.; Brachet, N. (2010). The temporal morphology of infrasound propagation. *Pure Appl. Geophys*. 167, 437–453. doi:10.1007/s00024-010-0080-6

Drob, D. P., Emmert, J. T., Meriwether, J. W., Makela, J. J., Doornbos, E., Conde, M., Hernandez, G., Noto, J., Zawdie, K. A., McDonald, S. E., Huba, J. D. & Klenzing, J. H. (2015). An Update to the Horizontal Wind Model (HWM): The Quiet Time Thermosphere. *Earth and Space Science*. doi:10.1002/2014ea000089

Gainville, O., Blanc-Benon, P., Blanc, E., Roche, R., Millet, C., Le Piver, F., Despres, B., and Piserchia, P. F. (2009), Misty Picture: A Unique Experiment for the Interpretation of the Infrasound Propagation from Large Explosive Sources, in "Infrasound Monitoring for Atmospheric Studies", eds. Le Pichon, A., Blanc, E., and Hauchecorne, A., Springer, pp. 575-598, doi:10.1007/978-1-4020-9508-5_18

Gardner, C. S., Hostetler, C. A. & Franke, S. J. (1993). Gravity wave models for the horizontal wave number spectra of atmospheric velocity and density fluctuations. *Journal of Geophysical Research*, 98 (D1), pp. 1035-1049. doi:10.1029/92jd02051

Gardner, C. S. (1994), Diffusive filtering theory of gravity wave spectra in the atmosphere, *J. Geophys. Res.*, Vol. 99, No. D10. (20 October 1994), pp. 20601-20622, doi:10.1029/94jd00819

Gibbons, S. J.; Ringdal, F.; Kværna, T. (2007). Joint seismic-infrasonic processing of recordings from a repeating source of atmospheric explosions., *J. Acoust. Soc. Am*. 122: EL158-EL164 doi:10.1121/1.2784533

Gibbons, S. J., Asming, V., Eliasson, L., Fedorov, A., Fyen, J., Kero, J., Kozlovskaya, E., Kværna, T., Liszka, L., Näsholm, S. P., Raita, T., Roth, M., Tiira, T. and Vinogradov, Y. (2015). The European Arctic: A Laboratory for Seismoacoustic Studies. *Seismological Research Letters*, Vol. 86, No. 3. (1 May 2015), pp. 917-928, doi:10.1785/0220140230

Gibson, R.G., Norris, D.E., and Drob, D.P. (2008), Investigation of the Effects of Fine-scale Atmospheric Inhomogeneities on Infrasound Propagation. Proceedings of the2008 Monitoring Research Review, Portsmouth, Virginia, September 23-25, 2008, LA-UR-08-05261 Los Alamos National Laboratory, pp. 872-881. http://rdss.info/librarybox/mrr/mrr2008/PAPERS/06-05.PDF

Hedlin, M. A. H. and Walker, K. (2013). A study of infrasonic anisotropy and multipathing in the atmosphere using seismic networks, *Philosophical Transactions of the Royal Society A: Mathematical, Physical and Engineering Sciences* **371**, doi:10.1098/rsta.2011.0542

Israelsson, H. (2013), Recordings from Hukkakero Explosions in 2009 at Infrasound Stations of the IRF Network. Technical Report, *SeismicInfra Research*. https://www.researchgate.net/publication/259267213_Recordings_from_Hukkakero_Explosions_in_2009_at_Infrasound_Stations_of_the_IRF_Network

Kalnay et al. (1996). The NCEP/NCAR 40-year reanalysis project, *Bull. Amer. Meteor. Soc*., 77, 437-470. doi:10.1175/1520-0477(1996)077<0437:tnyrp>2.0.co;2

Liszka, L.; Kvaerna, T (2008) Propagation of infrasound from chemical explosions*, InfraMatics*, March 2008, 1-10

Meriwether, J.; Mesquita, R.; Sanders, S.; Makela, J.; Harding, D.; Fisher, D.; Buriti, R.; Medeiros, A.F.; Drob, D. (2014). Solar cycle and seasonal variations of equatorial thermospheric temperature and winds. 8th Workshop on Long-Term Changes and Trends in the Atmosphere

Mutschlecner, J. P. and R. W. Whitaker (1999). Thermospheric Infrasound Signals, in "Proceedings of the 21st Seismic Research Symposium, Las Vegas, NV, September 21-24, 1999: Technologies for Monitoring The Comprehensive Nuclear-Test-Ban Treaty", Volume II, LA-UR-99-4700 Los Alamos National Laboratory, pp. 151-158. http://rdss.info/librarybox/mrr/srr1999/papers5/mutschle.pdf

Picone, J.M.; Hedin, A.E.; Drob, D.P.; Aikin, A.C. (2002). NRLMSISE-00 empirical model of the atmosphere: Statistical comparisons and scientific issues. *J. Geophys. Res*., 107(A12), 146, doi:10.1029/2002ja009430

Rienecker, M. M. et al. (2011), MERRA: NASA's Modern-Era Retrospective Analysis for Research and Applications. *J. Climate*, 24, 3624–3648. doi:10.1175/jcli-d-11-00015.1

Smets, P.S.M., L.G. Evers, S.P. Näsholm and S.G. Gibbons (2015), Probabilistic infrasound propagation using realistic atmospheric perturbations, *Geophys. Res. Lett. (1 July 2015),* 2015GL064992. doi: 10.1002/2015gl064992

Walker K. (2012) Atmospheric ray tracer 2D (ART2D). The software was obtained from the site http://sail.ucsd.edu/~walker/software/ART2D/art2d.html although this page has since been discontinued.

Whitaker, R. W. and J. P. Mutschlecner (2008). A comparison of infrasound signals refracted from stratospheric and thermospheric altitudes, *Journal of Geophysical Research* **113**, D08117, doi:10.1029/2007jd008852